Microstructure Evolution and Tensile Deformation in Mg Alloy AZ61 Through Thixomolding and Thermomechanical Processing

by

Tracy Dianne Berman

A dissertation submitted in partial fulfillment
of the requirements for the degree of
Doctor of Philosophy
(Applied Physics)
in The University of Michigan
2014

Doctoral Committee:

Professor J. Wayne Jones, Co-Chair
Professor Tresa M. Pollock, University of California Santa Barbara, Co-Chair
Professor John E. Allison
Professor Michael Atzmon
Assistant Professor Samantha H. Daly

“Only those who will risk going too far can possibly find out how far one can go.” - T.S. Eliot

To my cherished son, Cedric and husband, Greg.

ACKNOWLEDGEMENTS

Many people have assisted me on my circuitous journey through graduate education. Without their encouragement, knowledge, feedback, and support this dissertation would have never come to fruition.

I would first like to recognize my co-advisors, Professor Tresa Pollock and Professor Wayne Jones. Professor Pollock was supportive of my situation as a new mother and has served a role model for myself as a female scientist. I appreciate the feedback she continued to provide me, even as she moved on to UCSB. Professor Wayne Jones has been an outstanding source of feedback and suggestions. Words cannot express the respect I have for him.

Dr. Ray Decker and nanoMAG provided financial support, my materials, and interesting discussions. Dr. William Donlon assisted me microscopy and supplied critical feedback on my analysis and interpretation of data. I could also like to acknowledge the contributions of Ford Motor Company in the beginning of my career at Michigan, in particular Dr. Mei Li and Professor John Allison. Professor Allison continued to support me on my journey when he became a full-time faculty member. Professor Daly was also a great help.

Many students and post-docs from the Jones/Pollock group assisted me with training my project, including Dr. Jason Von Sluytman, Dr. Raghav Adharapurapu, and Dr. Jessica Terbush. In addition, I would like to recognize the contributions of

Victoria (Tori) Miller, Eric (Chung-Kai) Hung, Patrick Milligan, and Weston Lawson who aided me as undergraduate research assistants. Since Tori began her own graduate studies, it's been a great privilege to listen to her thoughts on recrystallization in magnesium alloys.

My fellow members in the Allison, Daly, Pollock, and Jones research groups have been a joy to work with. I feel incredibly lucky to have worked amongst all of you. My offices mates, Michael Kimiecik, Sinsar Hsie, and Dr. Jiashi Miao, deserve special recognition for dealing with my occasionally hyperactive nature and incessantly messy desk. Also, extra appreciation to Erin Deda, with whom I could commiserate with about magnesium sample preparation. Our mutual obsession with athletic endeavors helped decrease the guilt (a tiny bit) when I was running out of lab to get in a workout.

I truly appreciate the support and guidance of my first graduate research advisor, Dr. Timothy Ohno at the Colorado School of Mines. Significant aid came from my mentor at Mines, Dr. Joseph Beach. I would not have been able to endure the brutality of those first few years of graduate school without Joe's input, perspective, and support. I would not be the microscopist I am today without the training provided by Dr. John Chandler in the CSM electron microscopy laboratory.

I would also like to recognize the support of my family, in particular my husband, Greg. Becoming an Ironman and a Magnesium Woman within a 1-year period would have been absolutely impossible without his support. The two-body problem is formidable, but at least I have an amazing collaborator. Lastly, I must thank my son, Cedric, for the joy he has brought into my life. And Cedric, yes, mommy is done with her thesis.

TABLE OF CONTENTS

LIST OF FIGURES

Figure

LIST OF TABLES

Table

LIST OF ABBREVIATIONS

α-Mg	primary hexagonal close-packed Mg phase
AA5083	aluminum alloy, Al - 4.5% Mg - 0.7% Mn - 0.15% Cr
Al-5182	aluminum alloy, Al - 4.5% Mg - 0.35% Mn
AM60	magnesium alloy, Mg - 6% Al - $<$ 0.5% Mn
AZ31	magnesium alloy, Mg - 3% Al - 1% Zn
AZ61	magnesium alloy, Mg - 6% Al - 1% Zn
AZ71	magnesium alloy, Mg - 7% Al - 1% Zn
AZ80	magnesium alloy, Mg - 8% Al - $<$ 0.5% Zn
AZ91	magnesium alloy, Mg - 9% Al - 1% Zn
β or β-$Mg_{17}Al_{12}$	secondary phase in Mg-Al alloys
BSE	backscattered electron
CI	confidence index, degree of confidence that TSL software has correctly calculated the orientation
CRSS	critical resolved shear stress
DC	direct chill
DSR	differential speed rolling
EBSD	electron backscatter diffraction
El.	elongation to failure
ϵ_T	true strain

ϵ_t	strain along thickness
ϵ_w	strain along width
FEG	field emission gun
f_β	β-phase volume fraction
GOS	grain orientation spread, average misorientation between all data points within a given grain
H24 temper	strain hardened and partially annealed
hcp	hexagonal close-packed
IPF	inverse pole figure
JCPDS	Joint Committee on Powder Diffraction Standards
JMAK	Johnson-Mehl-Avrami-Kolmogorov
MRD	multiples of a random distribution or density
n-value	strain hardening exponent
ND	normal direction
O temper	fully annealed
ODF	orientation density function
PSN	particle stimulated nucleation
QPF	quick plastic forming
RD	rolling direction
RE	rare earth element
RUB	repeated uniaxial bending
SE or SEI	secondary electron or secondary electron imaging
SEM	scanning electron microscopy
σ_{SS}	solid solution strengthening
σ_T	true stress

STEM	scanning transmission electron microscopy
TD	transverse direction
TEM	transmission electron microscopy
TRC	twin roll cast(ing)
TTMP	Thixomolded and Thermomechanically Processed
UTS or σ_{UTS}	ultimate tensile strength
WE43	magnesium alloy, Mg - 4% Y - 3% RE
XRD	X-ray diffraction
YS or σ_{YS}	yield stress
Z1	magnesium alloy, Mg - 1% Zn
ZE10	magnesium alloy, Mg - 1% Zn - $<$ 0.5% RE
ZEK100	magnesium alloy, Mg - 1% Zn - $<$ 0.5% RE - $<$ 0.5% Zr
ZK10	magnesium alloy, Mg - 1% Zn - $<$ 0.5% Zr
ZK61	magnesium alloy, Mg - 6% Zn - 1% Zr
ZM21	magnesium alloy, Mg - 2% Zn - 1% Mn
ZW41	magnesium alloy, Mg - 4% Zn - 1% Y

ABSTRACT

Mg alloy sheets are of considerable interest in automotive, personal electronic, and medical applications because of their low specific density. However, conventional sheet develops a strong basal texture during rolling that persists through further processing, leading to poor room temperature formability. A reduction in basal texture coupled with grain refinement may significantly improve formability.

Thixomolding and thermomechanical processing (TTMP) has been shown to produce sheet with a good balance of strength and ductility. The objective of this research has been to identify the deformation and microstructural evolution phenomena responsible for these favorable properties.

We have demonstrated that TTMP of AZ61 produces a fine grain size stabilized by β-particles and with a weaker deformation texture than commercial Mg sheet, due in part to the presence of the β phase. Texture is further reduced during annealing, leading to decreased planar anisotropy.

Indicators of formability determined from tensile deformation, such as elongation to failure, work hardening coefficient, and r-value, indicate that TTMP AZ61 has the potential for excellent room temperature formability. Yield strength in the annealed sheets varies according to the Hall-Petch relationship; however, texture must also be taken into account. Yield strength and the work hardening coefficient are orientation dependent, and are directly related to the fraction of grains oriented favorably for

basal slip in the loading direction.

Damage accumulation in the β-particles during tensile deformation does not propagate into the matrix, consistent with the observation that ductility was independent of the β-phase volume fraction. Fractography reveals that failure results from microvoid coalescence in the matrix following the development of shear instability.

This dissertation has identified the microstructural mechanisms responsible for the promising deformation behavior in TTMP AZ61. It also demonstrates the value of considering the addition of secondary phase particles to Mg alloys subjected to rolling. These particles can act to stabilize the grain size and promote a weaker deformation texture, and if kept sufficiently small, will not limit ductility. As the arrangement and distribution of particles evolves little during TTMP, the largest amount of control in the secondary phases will likely be attained during the molding phase of TTMP.

CHAPTER I

Introduction

1.1 Motivation

Magnesium alloys are of considerable interest in automotive, personal electronic, and medical applications because of their low specific density. Magnesium, with a density of 1.7g/cm^3, is the lightest structural metal. It exists in a hexagonal close-packed (hcp) structure, with the c/a ratio close to the ideal packing ratio [1]. Substitution of an Al sheet component with a Mg component of the same shape results in a 37% reduction in weight. Widespread use of Mg alloys requires the production of high strength sheet, however, due to the disproportionate slip activity on the close-packed basal planes, a strong basal texture generated during the sheet production results in poor formability at ambient temperatures. This complication can be overcome by forming at elevated temperatures, but this introduces an increased cost as the energy requirements increase. Higher temperature forming also requires the selection of suitable lubrications and tooling.

The most commonly used Mg alloy sheet is AZ31 [2, 3], which has alloying additions of nominally 3 wt% Al and 1 wt% Zn. The AZ31 alloy was developed in the 1960s, yet for the most part it remains the only widely available Mg alloy for sheet [3]. Today, these sheets are found most commonly in portable electronic devices and

automotive applications [4, 5]. During the second world war, Mg sheet was used in German aircraft [6]. Part of the success of AZ31 is due to its resistance to corrosion and good weldability [7]. However, the limited formability of this alloy has prevented more widespread use of lightweight Mg sheets.

Conventional AZ31 sheet shows considerable tensile-compressive yield anisotropy; typical values for the tensile yield strength and a compressive yield strength in annealed sheet are 150 MPa and 110 MPa, respectively [7]. They also typically exhibit anisotropy in the plane of the sheet. The yield strength is often 15 MPa higher along the transverse direction (TD) than along the rolling direction (RD). These through-plane and in-plane anisotropies often create earing (formation of wavy edges at edges of drawn component), cracking, and unsuitable surfaces during drawing and stamping.

The poor formability of commercial AZ31 sheet, and the necessity for warm forming are a consequence of the lack of symmetry in the hcp crystal structure. The dominant activity of basal slip during rolling of Mg leads to the alignment of a majority of grains in the sheet such that their c-axis is nearly parallel to the sheet normal [8]. This basal texture usually has a maximum intensity of nearly 10 multiples of a random distribution (MRD) [8]. Once a basal texture develops, these grains are oriented unfavorably for basal slip both within the plane of the sheet and through the sheet thickness. An elevation in temperature allows for increased activation of prismatic and pyramidal slip to accommodate through-thickness strain and to compensate for the lack of basal slip activity [8]. Annealed AZ31 sheets require a forming temperature of approximately 160°C for anything but the most basic shapes [7]. Forming at elevated temperatures can lead to grain growth in the sheet, reducing the strength of the component.

Commercially available AZ31 sheet is produced from homogenized, direct chill (DC) cast slabs [3, 9]. The homogenized slabs are then passed through a rolling mill. Generally warm rolling is employed in Mg, where the rolling temperature is above or near the recrystallization temperature allowing for dynamic recrystallization [3]. Multiple rolling passes are normally employed, as many as eighteen, usually with intermediate heating steps [3, 9]. In order to minimize edge cracking, larger rolling reductions employ higher deformation temperatures and the first pass may be limited to only a 10% reduction [9]. The rolling temperature may be reduced after the initial reduction passes, and a final cold rolling pass may be used. The sheets often require flattening and annealing following rolling. AZ31 sheets are commercially available in both cold-worked and annealed conditions.

In order to improve upon the formability of commercially available Mg sheets, it is essential to maintain a fine grain size, which is beneficial for both strength and formability, and as much as possible, to avoid the formation of a basal texture. This may be achieved both through variations in the alloying and in the processing route.

1.2 Improvement of Formability Through Microstructure Modification

1.2.1 Grain Refinement

It is well known that grain refinement improves both strength and ductility in Mg and its alloys [10, 11], and thus grain refinement is an active area of investigation. Several authors have demonstrated that grain refinement results in an increase in ductility [12–15]. As the grain size is refined, the fracture mechanism has been observed to change from less ductile, intragranular failure, to more ductile rupture by microvoid coalescence in AZ31 [16, 17], AZ91[18], and WE43 [19]. In addition, grain sizes below 10 μm makes superplastic forming at elevated temperatures achievable

as grain boundary sliding becomes active [20–24].

Early work on the plastic deformation behavior of Mg focused on single crystals, which showed extensive evidence of basal slip but little evidence of other slip systems [8]. Basal slip provides only two independent slip systems, where the von Mises criterion requires five independent slip systems to accommodate an arbitrary shape change. If basal slip were the only deformation mechanism active at room temperature, Mg alloys would exhibit brittle failure. However, most polycrystalline Mg alloys exhibit some ductility [8]. Grain boundaries are thought to either impose constraints that act to promote non-basal slip or to provide a source for non-basal dislocations [8]. Grain refinement leads to an increase in grain boundary area, and therefore seems to promote an increased number of deformation mechanisms. Refinement also acts to suppress twinning, which may have a negative effect on ductility [11].

1.2.2 Texture

As basal slip is the predominant deformation mechanism, the orientation of the basal planes with respect to the loading direction plays a critical role in the deformation of Mg. Experiments designed to study the influence of starting texture, independent of grain size, by machining samples at different orientations from a textured plate show that the orientation of the basal planes to the loading direction has a strong effect on both the strength and ductility [25, 26]. As texture increases, the level of anisotropy approaches that of a Mg single crystal [27]. Since there have been only a few examples of sheet with significant non-basal texture components [28–30], the emphasis falls on modifying the basal texture intensity rather than on changing the character of the texture. Reduction of the basal texture can lead to dramatic improvements in ductility [31–34]. Figure 1.1 demonstrates how the dome height

at fracture when stretching sheet specimens over a 20 mm hemispherical punch at room temperature (Erichsen test) increases with a decreasing basal texture intensity (measured in terms of multiples of random density (MRD)) [32, 35–39].

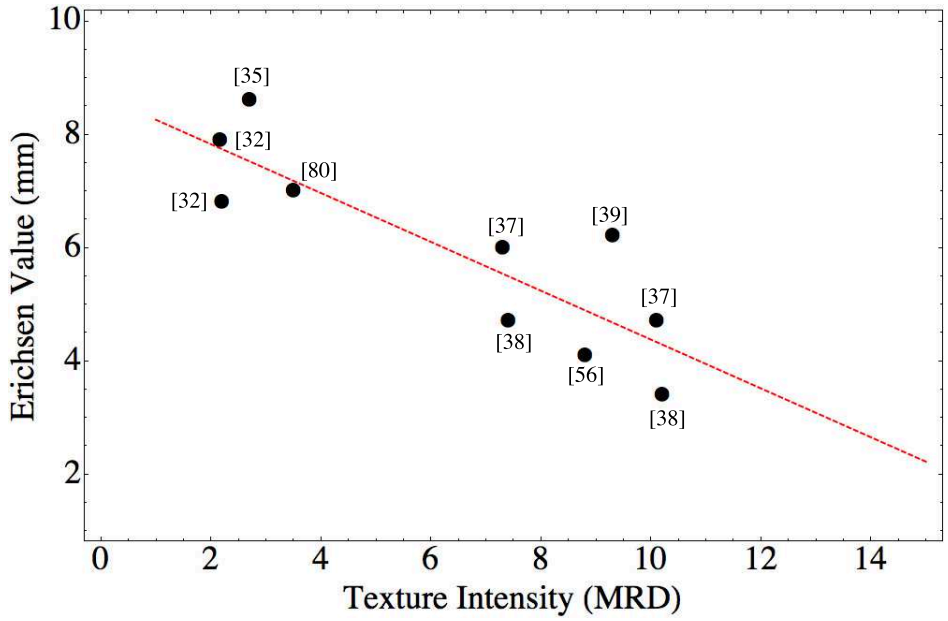

Figure 1.1: Relationship between texture intensity and Erichsen dome height at room temperature for various Mg sheets. Data referenced from

1.2.3 Secondary Phases

The introduction of secondary phases to Mg sheet has been reported to have both positive and negative effects on ductility. An increase in the volume fraction of intermetallic particles is often associated with embrittlement and an decrease in ductility [7, 40]. Yet, secondary phases can serve to decrease texture and stabilize a fine grain size [41]. Since the contribution of particles to these processes is still not understood, the engineering trade off cannot be established.

Brittle secondary phases are usually assumed to decrease ductility. Particle cracking during deformation in Mg alloys has been reported by several authors in AZ91

[18, 42–46], AZ80 [47], AZ31 with Sr additions [48] and in Mg-6.5 Gd-1.3 Nd-0.7 Y-0.3 Zn [28]. Only the work of Lu et al. [44] in a coarse grained, cast AZ91 with a high volume fraction of interconnected β-eutectics definitively shows that failure resulted from cracking in the secondary phase. Other studies reasonably hypothesize that damage in the brittle particles will lead to localized deformation in the α-Mg matrix near the crack tip, leading to propagation of the crack into the matrix or a reduction in load bearing area which nucleates voids in the nearby matrix. It is assumed that linkage of this damage plays a significant role in failure of the material.

The size, morphology, volume fraction, and distribution of the secondary particles are likely important factors determining the effect of the secondary particles on the deformation behavior. While continuous networks of a second phase eutectic allow for rapid crack propagation and brittle failure, shorter cracks in smaller, more evenly distributed precipitates are likely less significant. Several studies show cracks confined within the precipitates, with no evidence of propagation into the matrix [18, 45, 46, 48].

It is difficult to vary the size and volume fraction of secondary particles without also affecting grain size and texture, this complicates our understanding of how the secondary particles affect ductility. Chung et al. [18] observed an increase in ductility after 2 passes of equal channel angular pressing, which they credited in part to the removal of the the large, blocky β-particles, but it is clear that the grain size was refined as well. Sadeghi et al. [48] observed an increase in the ductility of AZ31 with the addition of 0.05 and 0.4 wt% Sr, but a decrease when the Sr addition was increased to 0.8%. They hypothesized the decreased ductility resulted from the increase of secondary phases within which cracks developed during deformation. As both the grain size and texture that resulted from the Sr addition is modified as well

[49, 50], it is difficult to asses the contribution of the particle cracking to the failure process.

The particle shape may also have an influence on ductility. Hou et al. [28] observed a difference in yield strength and ductility along the RD and TD, with the elongation along the RD being 20 to 100% higher than that along the TD depending on the deformation temperature and annealing treatment. The spread of the basal texture along the TD texture in the rolled Mg-6.5 Gd-1.3 Nd-0.7 Y-0.3 Zn sheets in that study favors basal slip along the TD more than along the RD, so some of the difference is certainly a result of the texture itself. Additionally, the elongation of the eutectic phases along the rolling direction results in a larger secondary particle cross section in the plane of the stress when the specimens are loaded along the TD. Hou et al. [28] conjecture that cracking within the secondary phases and interfacial decohesion may have contributed to the lower ductility of the material when loaded along the TD. Scanning electron microscopy (SEM) fractographs in the as-rolled alloy show deeper dimples when loaded along the RD and cracked particles in the bottoms of shallow dimples when loaded along the TD. It is difficult to evaluate the accuracy of this conclusion since the size and distribution of the elongated particles is neither shown nor described. The discrepancy between the RD and TD elongation in the as-rolled sheet increased following an aging treatment, which preserved the deformation texture, but it was not noted whether the elongated particles coarsened during aging.

As secondary particles can provide for grain size stability by Zener pinning, and can affect the deformation texture by altering the recrystallization kinetics and mechanisms, it is important to understand their impact on ductility [41]. The issue has not yet been adequately addressed. Engineering of the optimal microstructure re-

quires knowledge of the suitable size and volume of secondary phases. It is clear that further research on the contribution of the distribution and volume fraction of secondary phase particles to tensile deformation in Mg is needed.

1.3 Texture Modification

In order to improve formability, a significant amount of research has been conducted on texture reduction in Mg sheet alloys. Effective strategies to reduce or eliminate the strong basal texture in Mg alloy sheet include solute additions to increase activity of non-basal slip and/or to alter the kinetics of dynamic recrystallization [34, 51–54] and alternatives or modifications to the conventional process of hot rolling of a DC cast slab, such as asymmetric rolling [55–59], cross rolling [37], repeated unidirectional bending [39, 60], twin-roll casting [61, 62], and changes to the multiple pass rolling temperatures or final annealing treatment [16, 35, 38]. The impact of these approaches is summarized in the following sections.

1.3.1 Alloying

Before discussing Mg alloys, it is helpful to describe the naming convention used in commercial alloys. The names consist of letters designating the alloying additions in order of abundance followed by integers giving their respective rounded weight percentages [7]. The letter designations for common alloying additions in Mg sheets are listed in Table 1.1. Additional letters may be appended to distinguish alloys that have similar concentrations of primary alloying additions, but differ in the amount of lesser additions and impurities and also to demote the temper.

Table 1.1: Letter designation for common Mg sheet alloying additions.

Designation	Element
A	Aluminium
E	Rare Earth
H	Thorium
J	Strontium
K	Zirconium
L	Lithium
M	Manganese
T	Tin
X	Calcium
W	Yttrium
Z	Zinc

In terms of their associated texture, alloys used in Mg sheet can roughly be divided into two groups, those with rare earth elements (RE) and those without, commonly referred to as conventional alloys. Figure 1.2 shows a representative example of each. The conventional Mg sheet texture can be symmetric about the normal direction (ND), but the intensity is more often either split, or elongated along the RD [8, 35, 38, 39, 54, 63–65]. As shown in Figure 1.2, the split usually represents a tilt of 7 to 15° from the ND towards the RD [8]. This splitting is thought to result from the activation of $\langle \mathbf{c}+\mathbf{a} \rangle$ pyramidal slip during warm rolling [51]. The maximum texture intensity in commercial alloys is often around 10 MRD [8, 14, 37, 63, 66, 67].

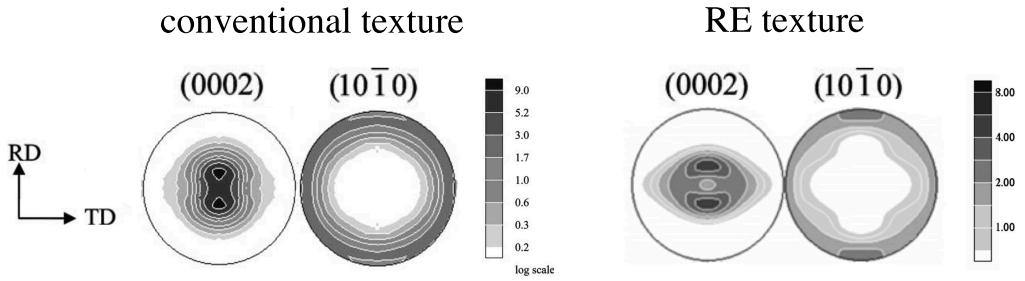

Figure 1.2: Typical (a) conventional texture represented by a commercial AZ31 sheet [8] and (b) RE texture illustrated by a hot-rolled ZEK100 sheet [54].

The most commonly used and readily available Mg sheet alloy is AZ31, and so, logically, research on this alloy comprises a signification portion of the body of Mg sheet literature. Aluminum improves castability, provides solid solution strengthening, and allows for the forming of age hardening β-$Mg_{17}Al_{12}$ precipitates [40]. Zinc acts to increase the solid solution strengthening [68]. In addition to AZ31, within the Mg-Al-Zn alloy system, texture has been studied in sheets of AZ61 [69, 70], AZ80 [71], and AZ91 [58]. The increased Al content in these alloys provides increased age hardening, but in general this comes at the cost of ductility [7, 40]. The sheet texture has also been reported on the non-RE containing alloys AM60 [72], Mg-Zn [73], Z1 [30], ZK10 [54], ZK61 [74], ZM21 [54], and Mg-Mn-Sr [75]. All of these sheets, aside from the ZK10, exhibit conventional texture. For unknown reasons, the ZK10 has an intermediate texture with a higher intensity like the conventional alloys, but a distribution more similar to the texture in the RE materials.

Recent studies have demonstrated that the addition of rare earth (RE) elements such as yttrium, gadolinium, cerium, neodymium, and misch metal ($\sim$ 50% cerium and $\sim$ 25% lanthanum and small amounts of praseodymium and neodymium) to Mg alloys results in a weaker texture and also leads to a more refined recrystallized grain size [2, 76]. The texture of RE sheets also often exhibits the split peak in the RD, but is distinct in two ways, (1) the spread in c-axis orientation is broader along the TD than along the RD, and (2) the maximum texture intensity is usually below 4 MRD [30, 32, 54, 77]. There is also a tendency for preferential alignment of the $\{10\bar{1}0\}$ planes with the RD. The development of the RE texture is not yet understood. It has been hypothesized that the atomic mismatch of RE additions results in an increase in non-basal slip during deformation brought about by a modification of the c/a ratio in the hcp crystal or segregation of the large atoms to grain boundaries

leads to solute drag which can alter the grain boundary mobilities and alter the dynamic recrystallization kinetics [30, 78]. While RE additions have been shown to be effective in generating a weaker deformation texture, they are costly and in limited supply [79]. Therefore, RE alloys are not the best choice for texture reduction if the goal is large-scale production of more formable Mg alloy sheets.

1.3.2 Processing

Modifying the rolling and intermediate reheating temperatures, the application of shear, the magnitude of strain per pass, and the total strain can affect the deformation and recrystallization mechanisms, and thus the as-rolled texture. This section will describe some of the modifications and variations of the hot rolling process that have been shown to influence the sheet texture.

Multiple Pass Hot Rolling

Hot rolling is generally used to describe rolling above the recrystallization temperature. There are numerous variables to consider in multiple pass hot rolling, including the number of passes, the reduction per pass, the rolling speed, the roll temperature, and the intermediate reheat time and temperature. The problem is complicated, and it is challenging to make broad conclusions from the literature as multiple variables are changed between each report. Huang and co-workers varied the final pass rolling temperature in seven-pass rolling and found that the deformation texture increased slightly from 5.4 to 6.3 MRD when the final pass temperature increased from 450°C to 555°C. However, following annealing at 350°C for 1 hour, the higher final pass rolling temperatures resulted in the weakest textures [35]. Miao

et al. [16] also observed an increase in deformation texture with increasing roll temperature. Another study shows an increase in texture (from 7.4 MRD to 10.2 MRD) with an increase in the temperature of the intermediate reheat from 390°C to 450°C. Unfortunately only the texture of annealed material is given [38].

Asymmetric Rolling

Asymmetrical rolling produces shear deformation by running the top and bottom rolls at different speeds (also known as differential speed rolling (DSR)) or using top and bottom rolls with different diameters. This process has also been shown to lead to a more refined grain size and weaker texture than symmetric rolling [3]. The texture of AZ31 sheet produced by asymmetric rolling can be reduced by as much as 50%, but may still have an intensity of $\sim$ 9 MRD in [56, 59]. Huang et al. [80] reported a maximum basal texture intensity of 3.7 MRD in an AZ61 sheet, but does not include a symmetrically rolled sheet for comparison. Chino et al. [57] observed a decrease in texture intensity from 7 to 5 MRD by moving from normal rolling to asymmetric rolling.

Cross Rolling

Cross rolling may entail altering the feed direction of the sheet between rolling passes as well as the use of a mill in which the top and bottom rollers are not parallel. Chino et al. [37] demonstrated a basal texture intensity reduction from 10.1 to 7.3 MRD in AZ31 sheet when a 7.5° tilt was introduced between the rollers in the RD-TD plane. Alternating the rolling direction by 90° between passes was shown to reduce texture from 11.2 to 9.6 MRD in Mg-0.6 wt%Zr [81]. Zhang et al. [82]

explored the difference in texture of an AZ31 sheet after 9 rolling passes in sheet in which (a) each pass was conducted along the same direction, (b) the rolling direction alternated between two perpendicular orientations, and (c) alternated between 3 orientations, the second and third being 90° and 135° from the first. All three samples were annealed following rolling. The resulting basal texture was lowest in the material rolled at three orientations (7.3 MRD) and highest in the unidirectional sheet (11.9 MRD).

Repeated Uniaxial Bending

Commercial hot rolled AZ31 sheets, processed by repeated uniaxial bending (RUB) have exhibited a decrease in the basal texture intensity [39, 60]. This procedure introduces shear by using a motor to pull the sheets through a 90° bend. In the first report, they perform six-passes and alternating the bending direction between the RD and TD while also flipping the sheet over between passes. This processing resulted in a basal texture reduction from 8.5 to 7.3 MRD and an increased spread along the RD in the basal pole figure [60]. In the second report, all six passes were performed with the bend parallel to the RD [39]. The results of this study are unusual, as they reported a maximum texture intensity of 30.6 in the as-received sheet, which is significantly higher than the texture commonly reported for hot rolled AZ31. After RUB processing, the texture had decreased to 9.3 MRD and spread dramatically along the RD. While this reduction is substantial, the texture remains higher than what was measured on the as-received sheet in the first study. The starting sheet for thickness between the two studies varied slightly, with 0.8 mm in the first publication and 0.6 mm in the second.

Twin Roll Casting

Twin roll casting (TRC) is a process that integrates the casting and rolling processes, and has been successfully applied to large-scale aluminum sheet production [83]. The rolls can be oriented either horizontally or vertically. One of the benefits of this processing route is savings in the time and cost needed to homogenize and preheat extruded and cast plates prior to reheating. The primary issue, which can be improved by modification of the liquid metal temperature and the casting speed, is inhomogeneity of the microstructure in terms of grain size and chemical segregation. Masoumi and co-workers observed a significantly weaker, and more RE-like texture in a TRC alloy ($\sim$ 3 MRD) which changed dramatically with annealing [61], while Bayandorian et al. [62] observed a conventional basal texture of 5 MRD, so it is clear there is a lot of room for texture control. Another benefit of TRC is that the rapid solidification rate can lead to a fine microstructure [3].

Thixomolding and Thermomechanical Processing

Decker and co-workers at Thixomat, LLC developed a new process designated as Thixomolded Thermomechanical Processing (TTMP), which produces Mg alloy sheet by utilizing Thixomolded plates as the warm-rolling feedstock [84, 85]. Thixomolding is an injection molding process, where the shearing of the liquid metal in the barrel decreases the viscosity, allowing casting to be done at lower temperature. The rapid solidification rate produces finer grain sizes, an isotropic texture, refined secondary phases, low porosity, and a relatively homogeneous microstructure [86, 87]. It was demonstrated that Mg- 6 wt%Al and Mg- 6 wt%Al-1 wt% Zn alloys produced by TTMP had a fine grain size, assumed to be stabilized by the refined

β-$Mg_{17}Al_{12}$ phase [84]. The TTMP sheets exhibit very limited edge cracking, and both the strength and ductility was improved from the as-Thixomolded condition. Our studies of TTMP AZ61 sheet have demonstrated a basal texture intensity less than 5 MRD, which can be reduced following a recrystallization annealing treatment [88–92].

Summary

While several processing techniques reduce the basal texture, in most studies the texture remained above 5 MRD. Those studies achieving lower textures were in asymmetrically rolled or TTMP AZ61 [80, 92] and in TRC AZ31 with numerous coarse intermetallics [61]. It is unclear whether secondary particles or the the processing route itself is responsible for the lower texture. However, this work establishes the feasibility of the production of weakly textured Mg alloy sheet without the use of RE additions.

Table 1.2 lists the grain size, basal texture intensity, and room-temperature tensile properties in AZ31 and AZ61 sheet produced by different processing routes. The initial strain rate used during deformation is noted, though AZ31 has weak strain rate sensitivity at room temperature [8].

Table 1.2: Comparison of room temperature properties of Mg alloys processed using different techniques. The average value is given if properties were measured in more than one orientation.

Alloy	**Processing Method**	**Grain size** μ**m**	**Strain Rate** s^{-1}	**YS MPa**	**UTS MPa**	**Elong. %**	**r-value**	**n - value**	**Max Texture Intensity MRD**	**Ref.**
AZ31B	commercial			225	285	19.5	2		12.1	[93]
AZ31	multiple pass hot roll + anneal	11		149	258	27.5	1.1	0.283	2.7	[35]
AZ31	multiple pass hot roll + anneal	3	$1x10^{-3}$	236	278	35			9.4	[16]
AZ31B	multiple pass hot roll + anneal	15	$1.7x10^{-3}$	170	260	22.5	2.1		7.4	[38]
AZ61	hot roll + anneal	14	$3x10^{-3}$	202	312	20				[69]
AZ61	multiple pass DSR + anneal	11.5	$3x10^{-3}$	147	300	23	1.3	0.31	3.7	[80]
AZ31	DSR	1.4		275	330	24			11.6	[59]
AZ31	DSR + anneal	2.5		225	295	35			8.2	[59]
AZ31	DSR	16	$3x10^{-3}$	160	259	24.5	2.5	0.28	8.8	[56]
AZ31	DSR	17.3	$1x10^{-3}$	99	252	11	1.2		6	[57]
AZ31	DSR +anneal	17.8	$1x10^{-3}$	125	245	30	2.5			[57]
AZ31	cross roll + anneal	40	$1.7x10^{-3}$	100		25	1.6		7.3	[37]
AZ31	cross roll + anneal	15.6	$1x10^{-3}$	170	350	28			7.3	[82]
AZ31B	RUB	6	$1x10^{-2}$	104	335	26			7.3	[60]
AZ31	TRC +anneal	10 and 100	$5x10^{-3}$	119	259	11.5		0.16	1.9	[61]
AZ31	Vertical TRC	8	$6.7x10^{-4}$	126	248	22.7			5	[62]
AZ61	Extruded + multiple pass hot roll	21	$3x10^{-3}$	220	311	18.5				[70]
AZ61	**TTMP**	**3**	$\mathbf{4x10^{-4}}$	**215**	**310**	**22.7**	**1.1**	**0.24**	**3.5**	**[92]**

1.4 Static Recrystallization Behavior

Texture generally does not change appreciably during static annealing of Mg alloy sheets [26, 30, 41, 94–97]. The maximum basal texture intensity may decrease slightly (usually no more than 30%), but new texture components are rarely observed. Discontinuous static recrystallization is the mechanism most commonly reported in Mg [98–104]. However, continuous static recrystallization in Mg alloys has also been reported [97, 105]. The term "discontinuous" is used to refer to recrystallization processes with distinct nucleation and growth phases. Discontinuous recrystallization is generally observed in the form of preferential nucleation of grains at grain boundaries and secondary particles. Continuous refers to a process where the nucleation is more homogenous throughout the microstructure, and nucleation and growth are less distinct processes. Huang et al. [103] made the observation that continuous recrystallization is often observed in materials that have undergone significant dynamic recrystallization while discontinuous static recrystallization is observed in materials with little or no dynamic recrystallization. In continuous recrystallization, as the recrystallized grains tend to adopt an orientation close to that of their parent grain, no new texture components develop. It is reported that discontinuous recrystallization can alter the deformation texture [41]. Substantial changes during annealing have been observed in Mg sheets with a significant amount of intermetallics and those with RE additions.

An increase in the volume fraction of intermetallic particles can lead to a sizable reduction in texture intensity upon annealing [106, 107]. Large particles, usually greater than 1 μm in diameter, can lead to a texture reduction via the mechanism of particle stimulated nucleation (PSN) [41]. PSN is the mechanism by which recrys-

tallization nuclei develop within dislocation gradients near particles. As the number of randomly oriented grains increases, the intensity of the deformation texture will decrease; a computer generated model for PSN showed a texture decrease from 5.4 to 3.1 times random [108]. Masoumi et al. [107] have demonstrated RE-like texture upon annealing of twin-roll cast AZ31, which they attributed to PSN arising from a higher volume fraction of secondary phases.

Small, closely spaced particles have also been shown to influence recrystallization behavior, though the effects are still not well understood [41]. The primary effect seems to be grain boundary pinning, which can slow the recrystallization kinetics and lead to an extended recovery period. In RE alloys, texture reduction and the increase of new texture components can occur, even in dilute alloys without secondary phases [53, 109]. Similar to the effect of small precipitates, this is thought to be a consequence of retardation of the recrystallization dynamics as grain boundaries are pinned by the relatively large RE elements by solute drag effects [34, 52, 110, 111]. A few studies have shown a dramatic change in texture upon static annealing [29, 30]. As the size and distribution of secondary particles can be controlled by alloying and processing, it is important to understand their effect their influence on recrystallization for design of weakly textured, high formability Mg alloy sheets.

1.5 Tensile Deformation Behavior

Uniaxial tensile deformation yields information about the strength and ductility, and enables the calculation of parameters that provide insights into the formability of the material. This section will discuss the typical tensile deformation behavior of Mg alloy sheets, which factors control strength, and how the work hardening coefficient

and Lankford r-value predict formability. It will also explore the relative activity of different deformation mechanisms during formability. Finally, we will discuss the damage and failure mechanisms reported in Mg alloy sheets.

1.5.1 Deformation Mechanisms

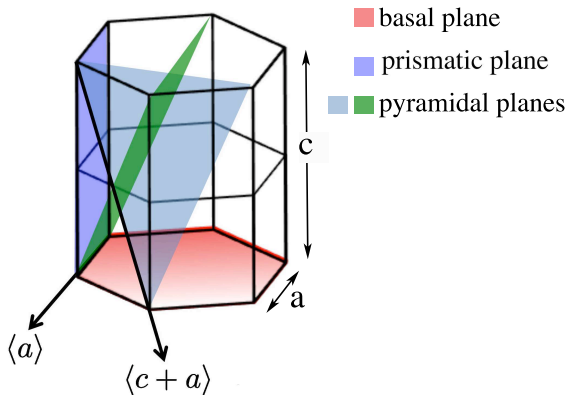

Figure 1.3: Illustration of the most common slip planes and slip directions in Mg.

The hcp magnesium crystal can deform through basal ⟨**a**⟩, prismatic and pyramidal ⟨**a**⟩, and pyramidal ⟨**c**+**a**⟩ slip as well as mechanical twinning. The common slip planes and directions are illustrated in Figure 1.3. Basal and prismatic ⟨**a**⟩ each provide two independent slip systems, while pyramidal ⟨**a**⟩ provides four. Deformation parallel to the c-axis requires activation of ⟨**c**+**a**⟩, which requires higher stress or a higher deformation temperature [112].

Early studies on the plastic properties of Mg focused on single crystals, which showed extensive evidence of basal slip, but little evidence of other slip systems. Thus it was assumed that the stress needed to activate non-basal slip was much higher than that needed to activate basal slip [8]. Since the von Mises criterion requires five independent slip systems to accommodate an arbitrary shape change, if

basal slip were the only deformation mechanism active at room temperature, then Mg alloys would exhibit brittle failure. In reality, most polycrystalline Mg alloys exhibit some ductility [8]. Grain boundaries are thought to either impose constraints that act to promote non-basal slip or to provide a source for non-basal dislocations [8, 113]. The critical resolved shear stress (CRSS) of basal slip at room temperature has been measured to be two to three times less than the next easiest deformation mode [51]. Regions of grains more favorably oriented for basal slip are considerably "softer" than those not favorably oriented, which leads to considerable grain to grain variability [114]. Different slip mechanisms may exhibit different grain size dependencies [115]. The CRSS for $\langle \mathbf{c}+\mathbf{a} \rangle$ slip is high at room temperature, but decreases rapidly as temperature increases [116].

Twinning is common in magnesium, especially during compression along the c-axis, and is thought to make a contribution to the five slip systems needed to meet the von Mises criterion [8, 117]. The CRSS for twinning has been found to be insensitive to temperature [118]. It has been observed that the twinning density is higher in the neck area than in the region of uniform elongation [69], and has been reported to only occur near failure [8]. The amount of deformation that can be accommodated by twinning is directly related to the volume fraction twinned [8]. Schmid and Boas [119] calculated that the maximum strain that can be accommodated by twinning alone is 0.065; perhaps the main contribution of twinning is to reorient grains such that $\langle \mathbf{a} \rangle$ slip become favorable [51, 69]. Samples mounted such that the stress axis is perpendicular to the c-axis is unfavorable for basal slip but facilitates $\{10\bar{1}2\}\langle 10\bar{1}1 \rangle$ twinning. However, $\{10\bar{1}2\}$ twins do occur in samples loaded along the RD, and are thought to result from compressive strain along the c-axis imposed by neighboring grains [8, 120]. Twinning is reported more frequently in grains larger than 10 μm,

and is suppressed by grain refinement [113, 118].

The activity of slip systems can be determined by transmission electron microscopy dislocation analysis, though little work has been done to explore non-basal slip in polycrystalline Mg alloys and analysis is limited to first few percent of plastic deformation [8, 113, 121]. Another method to track the activity of deformation mechanisms is through the evolution of texture during deformation. During tension, deformation by slip leads to a rotation of the lattice such that the active slip direction tends to become aligned along the tensile axis and the active slip plane parallel to the tensile stress axis [122]. During tensile deformation, dislocation slip leads to the slip plane rotating perpendicular to the tensile axis. As a result, samples tested along the RD showed an increased spread in the TD, and the samples tested along the TD showed an increased spread of the basal poles along the RD [8]. Therefore, texture evolution during deformation provides insights regarding the relative slip system activities. If basal slip is the dominant deformation mechanism, the basal texture intensity tends to increase [123, 124]. The exhaustion of basal slip may be evident if there is a decrease in intensity of peaks representing grains oriented favorably for basal slip [122]. Prismatic $\langle \mathbf{a} \rangle$ slip activity can be recognized by the development of six-fold symmetry in the $\{10\bar{1}1\}$ and $\{10\bar{1}0\}$ pole figures [8].

1.5.2 Yield Strength

The yield strength of Mg alloys is controlled by the grain size, solid solution strengthening additions, texture, and precipitation strengthening. The orientation of the tensile sample with respect to the initial texture plays a significant role in determining the yield stress [26, 125]. Basal textured sheet materials have a strong tension-compression asymmetry that is associated with the anisotropic nature of

twinning in the hcp crystals. This asymmetry results in non-uniform bending characteristics and forming failures [126]. Materials with the conventional texture exhibit a higher strength along the TD than along the RD, which is directly related to the broader spread of the c-axis along the RD than along the TD [8]. As the c-axes of the grains are tilted more towards the RD than the TD, the Schmid factor for basal slip of $\langle \mathbf{a} \rangle$ dislocations in a "typical" grain is larger for the RD samples than for the TD samples. Therefore soft basal slip can accommodate more of the deformation in the RD than in the TD orientation, leading to a higher strength along the TD orientation. If grains are not favorably oriented for basal slip, then they must deform by other, harder deformation modes. With tilted basal textures, in the early stages of deformation basal slip occurs in the soft grains, however, as the sample elongates and the c-axis rotates towards a direction perpendicular to the tensile axis, basal slip activity decreases. Non-basal slip accommodates more of the strain in the TD samples. Through transmission electron microscopy (TEM) analysis, Agnew observed that up to 80% of the strain in the TD orientation under tension is accommodated by non-basal slip [121]. For the same reason, sheets with the RE texture exhibit a yield anisotropy with the highest yield strength along the RD and the lowest along the TD [54]. Sheets with a RE texture, exhibit a broader spread in the TD and thus are more favorably oriented for soft basal slip along this direction.

In Mg-Al alloys, Al provides for solid solution strengthening (σ_{SS}) following Eqn. 1.1, where n=1/2, m=5.6, B_n=21.2 (at.)$^{1/2}$, and c is the at.% Al [127]. The aluminum in the AZ31 alloy contributes a maximum of 20 MPa to the yield strength at room temperature.

$$\sigma_{SS} \approx m B_n c^n \tag{1.1}$$

The contribution of grain size to the yield strength of the material is given by the

Hall-Petch relationship (Eqn. 1.2), where σ_o is the lattice resistance of the matrix to slip, k is the Hall-Petch coefficient, and d is the average grain size of the material. Hall-Petch coefficients between 4 and 10 MPa$\times$mm$^{1/2}$ have been reported in AZ series alloys [128].

$$\sigma_{gs} = \sigma_o + kd^{-1/2} \tag{1.2}$$

Assuming a uniform distribution of precipitates with identical strength, the contribution of precipitates to yield strength can be modeled by Orowan strengthening [129]:

$$\sigma_{Orowan} = \frac{MG\mathbf{b}}{2\pi\sqrt{1-\nu}}\frac{1}{\lambda}\ln\left(\frac{d_A}{r_o}\right) \tag{1.3}$$

where M is the Taylor factor (5), G is the shear modulus of the matrix (17.2 GPa), **b** is the Burgers vector for basal slip in Mg (0.32 nm), ν is the Poisson's ratio (0.35), λ is the mean particle spacing in the slip plane, d_A is the mean particle diameter, and r_o is the inner cut-off radius of the dislocation. AZ31, with only 3 wt% Al, is not an age hardenable alloy. Generally, alloys with the potential for a significant formation of precipitates are avoided, as they are believed to have more brittle behavior.

1.5.3 Work Hardening

Hollomon's equation (Eqn. 1.4) models work hardening as a power law relationship between the true stress and true strain, where n is referred to as the strain hardening exponent. Higher strain hardening coefficients indicate more resistance to shear localization, and thus predict better formability during stretching [130]. Strain hardening exponents between 0.12 and 0.31 have been reported in Mg sheet [8, 32, 35, 39, 56, 61, 80, 82]. Conventional AZ31 sheet has the lowest coefficient[8]

and the highest value was measured in AZ31 sheets with a maximum basal texture intensity less than 4 MRD [80].

$$\sigma_T = K\sigma^n \tag{1.4}$$

1.5.4 Lankford r-value

The r-value, also referred to as the Lankford value or the anisotropy factor (Eqn. 1.5), is a comparison of the strain in width direction, ϵ_w=Ln(w_f/ w_o), to the strain in the thickness direction, ϵ_t=Ln(t_f/ t_o) after a specified amount of tensile straining, where w_f and w_o are the final and initial width and t_f and t_o are the final and initial thickness [131].

$$r = \epsilon_w/\epsilon_t \tag{1.5}$$

$$\bar{r} = |r_0 + 2 * r_{45} + r_{90}|/4 \tag{1.6}$$

$$\Delta r = |r_0 - 2 * r_{45} + r_{90}|/2 \tag{1.7}$$

In steel, a high r-value indicates a material with good drawing properties [130]. However, in hcp materials a high r-value is associated with strong anisotropy and poor formability [63, 132]. Instead, reduced r-values in Mg-sheet indicate improved sheet thinning and improved formability for stretching operations [35, 54, 63]. In magnesium the r-value is generally measured at a fixed strain between 8 and 11% [8]. From the r-value determined by loading at 0°, 45°, and 90° from the RD, two additional forming parameters can be calculated, the average r-value, $\bar{r}$ (Eqn. 1.6), and Δr (Eqn. 1.7). In hcp Mg sheet, a low $\bar{r}$ and low Δr indicate optimal formability with more isotropic behavior. Large variations in $\bar{r}$ can cause forming problems such

as earing [32]. The r-value is highly dependent on texture [133]. Values from 0.8 to 3 have been reported for $\bar{r}$ [8, 32, 35, 37–39, 54, 56, 57, 63, 80, 93, 134, 135], with conventional AZ31 sheets having the highest values [8, 38]. Materials with $\bar{r}$ between 0.8 and 1.2 tend to be those with the weakest basal texture intensities [32, 35, 54, 63]. Polycrystal plasticity models suggest that a reduction in r-value can result from the activation of $\langle \mathbf{c}+\mathbf{a} \rangle$ slip [136].

1.5.5 Fracture

Despite the perception that only basal slip operates extensively at room temperature, commercial AZ31 and other Mg alloy sheets typically have an elongation to failure of 15% [7]. Mg sheets usually exhibit a shear angle of near 45° [137]. Ductile microvoid coalescence has been observed by several authors in Mg alloy sheets [42, 48, 69, 138–140]. As grain size increases to above 10 μm, the fracture surface shows more brittle fracture modes [16, 18, 19]. Particles are often observed in the bottom of dimples [42, 44, 48, 140], and as discussed in Section 1.2.3, the cracks that develop in the brittle intermetallics are often associated with failure of the material, though the evidence in most cases is inconclusive.

1.6 Forming of Mg Alloy Sheet

Formability of Mg alloy sheet at room temperature is limited. Investigations of formability in Mg alloy sheet have established that due to the prevalence of basal slip at ambient temperatures, formability can be improved through a decrease in the basal texture intensity or an increase in forming temperature [32, 35, 37, 39, 56, 141–144]. As temperature is elevated, and non-basal slip systems are more easily activated, the

advantages of a weak basal texture are reduced [39, 142].

Stretch formability is accessed by the measurement of the maximum dome height achieved at failure as sheet is loaded by the bulge media (a ridged punch or pressurized liquid or gas). Limiting dome height and Erichsen tests, utilize a ridged punch to deform the sheet. Liquid and gas bulge tests utilize pressurized liquid or gas. Boba et al. [142] observed a limiting dome height of 29.7 mm vs. 12.7 mm at room temperature in the more weakly textured ZEK100 compared to commercial AZ31 sheet. In both alloys the limiting dome height increased with forming temperature, however the improvement was more substantial in AZ31. Randman et al. [145] also observed that ZEK100 exhibited an dome height nearly twice that measured in AZ31B formed at the same temperature. Interestingly, in Randman's work increasing the forming temperature to 425°C did not increase the limiting dome height in either alloy. Zhang et al. [39] found that commercial AZ31B sheet required a temperature of at least 100°C for successful deep drawing, but that weakly textured AZ31 sheet produced by repeated uniaxial bending could perform deep drawing at room temperature. Zhang and coworkers [82] were able to increase the room temperature Erichsen value of a commercial AZ31 sheet by 50% by pre-stretching it for a 5% elongation at 250°C, which provided for a $\sim$ 80% reduction in basal texture.

Bulge tests on 1.56 mm thickness TTMP AZ61 sheets (the material studied in this dissertation) demonstrate that the maximum dome height achieved at a strain rate of $1.3 \times 10^{-3} s^{-1}$ can be increased from 7 mm to 30 mm by increasing the forming temperature from 25°C to 300°C [141]. A similar increase in dome height with increase temperature was observed at strain rates of $1.3 \times 10^{-2} s^{-1}$ and $1.3 \times 10^{-1} s^{-1}$. Liquid bulge tests preformed on TTMP AZ61 at 255°C achieved a bulge height of 18 mm [86]. Gas bulge tests performed by the Interlaken Technology Corporation

between 200°C and 300°C on Al-5182 and TTMP AZ61 demonstrate that warm forming in TTMP AZ61 can be performed at faster rates and lower stresses, likely decreasing the cost of components [86].

Failure during forming usually results from a catastrophic shear instability [143]. Dreyer et al. [143] observed that failure in warm forming of ZW41 resulted from transgranular ductile tearing, and not cleavage or intergranular cracking. Formation of compression twin shear bands in biaxially deformed AZ31 sheet at room temperature contributed to a lower forming limit in both biaxial and plane strain tensile specimens [146]. Another potential source for instabilities are secondary phase particles, however little work has been done in order to explore the effect of second phase particles on the formability of Mg alloy sheet. Carter et al. [147] observed that dome height achieved in continuous cast Mg alloy sheet was lower than expected based on grain size due to failure caused by long stringers of inter metallic particles. Verma et al. [148] also observed random location failures during pneumatic testing of AZ31B sheets due to stringers of intermetallics along the RD.

Mg alloy sheet components have been successfully formed at elevated temperatures. Successful stamping of simple components using AZ31 sheet, such as 125 mm deep rectangular pans, have been achieved at temperatures between 150°C and 350°C [5]. Carter et al. [147] tested numerous commercial grade Mg alloy sheets via pneumatic biaxial bulge testing at 450°C and found that several of them exhibited formability similar to a fine-grain AA5083 Al sheet that has already been established for quick plastic forming (QPF) of automotive components. The temper of the sheet was found to determine if the sheet would successfully meet the forming requirements, with fully recrystallized O-temper sheets exhibiting lower biaxial formability than sheets in the strain hardened and partially recrystallized H24 tem-

per. In the same work the authors also demonstrated that commercial AZ31B sheet could be used successfully to produce inner door panels using the existing QPF process and dies at 450°C. Randman and coworkers [145] demonstrated that wide sheets of asymmetrically rolled AZ31B and ZEK100 sheet could be successfully formed into automotive parts, though the weak texture of ZEK100 allowed for more rapid forming.

1.7 Objectives and Approach

The use of Mg alloy sheet, which could provide significant weight savings in many applications, is limited due to its poor formability. It has been demonstrated that the formability can be improved through refinement of the grain size and a decrease in the basal texture developed during sheet rolling. RE additions are quite effective in producing weakly textured sheets, but these additions are limited in availability and are costly. Alterations to the conventional multiple pass hot rolling route can also produce more weakly textured sheets. This dissertation explores the use of TTMP to produce high strength, weakly textured sheets with good formability.

AZ31 is the most commonly used wrought Mg alloy sheet, however AZ61 was chosen as it can be successfully Thixomolded with low porosity [86] and allows for the possibility of increased precipitation and solid solution strengthening as it has a higher Al content. Thixomolded AZ61 has a significant volume fraction of β-$Mg_{17}Al_{12}$ particles, so study of this alloy allows for evaluation of the influence of secondary particles on texture and grain refinement. It had been established that TTMP can produce favorable tensile properties, yet the mechanisms responsible were not well understood. The objectives of this research are to (1) develop an understanding of

the microstructure and texture evolution during TTMP, (2) determine the effect of TTMP on the tensile deformation behavior and use the tensile behavior to predict the room-temperature formability of TTMP AZ61, and (3) evaluate the contribution of the β-phase to grain size stability, texture evolution, and failure of the TTMP AZ61 sheets.

Chapter II describes the experimental procedures used in this investigation. Chapter III discusses the evolution of microstructure and texture during TTMP and explores the stability of the recrystallized grain size. Chapter IV explains how the microstructure and texture evolution determine the room-temperature tensile deformation behavior. The active deformation modes are explored by studying the evolution of texture during deformation. Finally, we describe the failure mechanisms observed in the as-Thixmolded plate and TTMP sheet. Chapter V summarizes the major conclusions of this work and provides suggestions for further studies on TTMP and Mg sheet production.

Bibliography

1. Y. Wang and J. Huang, *Materials Chemistry and Physics*, 81 (1) (2003), 11–26.
2. M. Pekguleryuz, *Advances in Wrought Magnesium Alloys*, eds. C. Bettles and M. Barnett (Woodhead Publishing, Cambridge, UK, 2012), chap. 1, 3–62.
3. J. Bohlen, G. Kurz, S. Yi, and D. Letzig, *Advances in Wrought Magnesium Alloys*, eds. C. Bettles and M. Barnett (Woodhead Publishing, Cambridge, UK, 2012), chap. 10, 346–375.
4. Magnesium Elektron,"Wrought Magnesium Alloys," http://www.magnesium-elektron.com/products-services.asp?ID=10 (2014).
5. A. A. Luo and A. K. Sachdev, *Advances in Wrought Magnesium Alloys*, eds. C. Bettles and M. Barnett (Woodhead Publishing, Cambridge, UK, 2012), chap. 10, 393–426.
6. R. E. Brown and E. Lee, *Proceedings of the 9th International Conference Magnesium Alloys and Their Applications*, eds. W. Poole and K. Kainer (ICMAA2012, Vancouver, Canada, 2012), 453–460.
7. *ASM Handbook: Volume 2 (Properties and Selection : Nonferrous Alloys and Special-Purpose Materials)* (ASM, 1990).
8. S. Agnew and O. Duygulu, *International Journal of Plasticity*, 21 (6) (2005), 1161–1193.
9. F. Zarandi and S. Yue, *Magnesium Alloys - Design, Processing and Properties*, ed. F. Czerwinski (InTech, 2011), chap. 14, 297–320.
10. J. Chapman and D. Wilson, *Journal of the Institute of Metals*, 91 (1962), 39–40.
11. M. Barnett, D. L. Atwell, and A. Beer, *Materials Science Forum*, 558-559 (2007), 433–440.
12. A. Yamashita, Z. Horita, and T. Langdon, *Materials Science and Engineering A*, 300 (1-2) (2001), 142–147.
13. C. Lee, *Materials Science and Engineering: A*, 459 (1-2) (2007), 355–360.
14. A. Jain, O. Duygulu, D. Brown, C. Tomé, and S. Agnew, *Materials Science and Engineering: A*, 486 (1-2) (2008), 545–555.
15. B. Shi, R. Chen, and W. Ke, *Journal of Magnesium and Alloys*, 1 (3) (2013), 210–216.
16. Q. Miao, L. Hu, G. Wang, and E. Wang, *Materials Science and Engineering: A*, 528 (22-23) (2011), 6694–6701.
17. A. Sadeghi, S. Shook, and M. Pekguleryuz, *Materials Science and Engineering: A*, 528 (25-26) (2011), 7529–7536.

18. C. W. Chung, R. G. Ding, Y. Chino, M. A. Hodgson, and W. Gao, *IOP Conference Series: Materials Science and Engineering*, 4 (2009), 012012.

19. T. Mukai, T. Mohri, M. Mabuchi, M. Nakamura, K. Ishikawa, and K. Higashi, *Scripta Materialia*, 39 (9) (1998), 1249–1253.

20. A. Bussiba, A. Benartzy, A. Shtechman, S. Ifergan, and M. Kupiec, *Materials Science and Engineering A*, 302 (1) (2001), 56–62.

21. Y. Miyahara, K. Matsubara, Z. Horita, and T. G. Langdon, *Metallurgical and Materials Transactions A*, 36 (July) (2005), 1705–1711.

22. T. Mohri, M. Mabuchi, M. Nakamura, T. Asahina, H. Iwasaki, T. Aizawa, and K. Higashi, *Materials Science and Engineering A*, 290 (1-2) (2000), 139–144.

23. K. Matsubara, Y. Miyahara, Z. Horita, and T. G. Langdon, *Acta Materialia*, 51 (11) (2003), 3073–3084.

24. R. Lapovok, P. Thomson, R. Cottam, and Y. Estrin, *Materials Science and Engineering: A*, 410-411 (2005), 390–393.

25. R. Gehrmann, M. Frommert, and G. Gottstein, *Materials Science and Engineering A*, 395 (1-2) (2005), 338–349.

26. S. Agnew, J. Horton, T. Lillo, and D. Brown, *Scripta Materialia*, 50 (3) (2004), 377–381.

27. E. W. Kelley and W. F. Hosford, *Transactions of the Metallurgical Society of AIME*, 242 (April) (1968), 654–661.

28. X. Hou, Z. Cao, L. Zhao, L. Wang, Y. Wu, and L. Wang, *Materials and Design*, 34 (2012), 776–781.

29. I. Basu and T. Al-Samman, *Magnesium Technology*, eds. M. L. Alderman, M. V. Manuel, N. Hort, and N. Neelameggham (2014), 133–138.

30. L. W. F. Mackenzie and M. Pekguleryuz, *Scripta Materialia*, 59 (6) (2008), 665–668.

31. T. Mukai, H. Watanabe, K. Ishikawa, and K. Higashi, *Materials Science Forum*, 419-422 (2003), 171–176.

32. D. Wu, R. Chen, and E. Han, *Journal of Alloys and Compounds*, 509 (6) (2011), 2856–2863.

33. N. Stanford and M. Barnett, *Journal of Alloys and Compounds*, 466 (1-2) (2008), 182–188.

34. N. Stanford, D. Atwell, and M. Barnett, *Acta Materialia*, 58 (20) (2010), 6773–6783.

35. X. Huang, K. Suzuki, Y. Chino, and M. Mabuchi, *Journal of Alloys and Compounds*, 509 (28) (2011), 7579–7584.

36. X. Huang, K. Suzuki, and N. Saito, *Scripta Materialia*, 61 (4) (2009), 445–448.

37. Y. Chino, K. Sassa, and M. Mabuchi, *Journal of Materials Science*, 44 (7) (2009), 1821–1827.

38. Y. Chino and M. Mabuchi, *Scripta Materialia*, 60 (6) (2009), 447–450.

39. H. Zhang, G. Huang, D. Kong, G. Sang, and B. Song, *Journal of Materials Processing Technology*, 211 (10) (2011), 1575–1580.

40. I. Polmear, *Light Alloys: From Traditional Alloys to Nanocrystals* (Elselvier, Oxford, 2006), 4 ed.

41. F. Humphreys and M. Hatherly, *Recrystallization and Related Annealing Phenomena* (Elsevier, Netherlands, 2004), 2 ed.

42. A. Luo, *Metallurgical and Materials Transactions A*, 26 (September) (1995), 2445–2455.

43. C. D. Lee, *Metals and Materials International*, 16 (4) (2010), 543–551.

44. Y. Lu, Q. D. Wang, W. J. Ding, X. Q. Zeng, and Y. P. Zhu, *Material Letters*, 44 (July) (2000), 265–268.

45. C. D. Lee and K. S. Shin, *Metals and Materials International*, 9 (1) (2003), 21–27.

46. B. Chen, D.-L. Lin, L. Jin, X.-Q. Zeng, and C. Lu, *Materials Science and Engineering: A*, 483-484 (2008), 113–116.

47. Q. Guo, H.-G. Yan, Z.-H. Chen, and H. Zhang, *Transactions of Nonferrous Metals Society of China*, 16 (4) (2006), 922–926.

48. A. Sadeghi, S. Shook, and M. Pekguleryuz, *Materials Science and Engineering: A*, 528 (25-26) (2011), 7529–7536.

49. A. Sadeghi and M. Pekguleryuz, *Materials Science & Engineering A*, 528 (3) (2011), 1678–1685.

50. A. Sadeghi, M. Hoseini, and M. Pekguleryuz, *Materials Science and Engineering: A*, 528 (7-8) (2011), 3096–3104.

51. S. Agnew, M. Yoo, and C. Tomé, *Acta Materialia*, 49 (20) (2001), 4277–4289.

52. K. Hantzsche, J. Bohlen, J. Wendt, K. Kainer, S. Yi, and D. Letzig, *Scripta Materialia*, 63 (7) (2010), 725–730.

53. J. P. Hadorn, K. Hantzsche, S. Yi, J. Bohlen, D. Letzig, J. A. Wollmershauser, and S. Agnew, *Metallurgical and Materials Transactions A*, 43 (April) (2012), 1347–1362.

54. J. Bohlen, M. R. Nurnberg, J. W. Senn, D. Letzig, and S. Agnew, *Acta Materialia*, 55 (2007), 2101–2112.

55. B. Radhakrishnan, S. B. Gorti, G. M. Stoica, and G. Muralidharan, *Metallurgical and Materials Transactions A*, 43 (May) (2012), 1509–1516.

56. X. Huang, K. Suzuki, A. Watazu, I. Shigematsu, and N. Saito, *Journal of Alloys and Compounds*, 470 (1-2) (2009), 263–268.

57. Y. Chino, M. Mabuchi, R. Kishihara, H. Hosokawa, Y. Yamada, C. Wen, K. Shimojima, and H. Iwasaki, *Materials Transactions*, 43 (10) (2002), 2554–2560.

58. W. Kim, J. Park, and W. Kim, *Journal of Alloys and Compounds*, 460 (1-2) (2008), 289–293.

59. W. Kim, J. Lee, W. Kim, H. Jeong, and H. Jeong, *Scripta Materialia*, 56 (4) (2007), 309–312.

60. G.-S. Huang, H.-C. Li, B. Song, and L. Zhang, *Transactions of Nonferrous Metals Society of China*, 20 (1) (2010), 28–33.

61. M. Masoumi, F. Zarandi, and M. Pekguleryuz, *Materials Science and Engineering: A*, 528 (3) (2011), 1268–1279.

62. I. Bayandorian, I. Stone, Y. Huang, and Z. Fan, *Magnesium Technology*, eds. S. Mathaudhu, W. Sillekens, N. Hort, and N. Neelameggham (Wiley, 2012), 135–140.

63. S. Yi, J. Bohlen, F. Heinemann, and D. Letzig, *Acta Materialia*, 58 (2) (2010), 592–605.

64. L. Jin, J. Dong, R. Wang, and L. Peng, *Materials Science and Engineering: A*, 527 (7-8) (2010), 1970–1974.

65. J. Koike, *Metallurgical and Materials Transactions A*, 36 (7) (2005), 1689–1696.

66. M. Eddahbi, J. del Valle, M. Pérez-Prado, and O. Ruano, *Materials Science and Engineering: A*, 410-411 (2005), 308–311.

67. H. Wang, B. Raeisinia, P. Wu, S. Agnew, and C. Tomé, *International Journal of Solids and Structures*, 47 (21) (2010), 2905–2917.

68. S. Spigarelli, M. Mehtedi, M. Cabibbo, E. Evangelista, J. Kaneko, A. Jager, and V. Gartnerova, *Materials Science and Engineering: A*, 462 (1-2) (2007), 197–201.

69. A. N. Chamos, S. G. Pantelakis, G. N. Haidemenopoulos, and E. Kamoutsi, *Fatigue & Fracture of Engineering Materials & Structures*, 31 (9) (2008), 812–821.

70. J. Koike and R. Ohyama, *Acta Materialia*, 53 (2005), 1963–1972.

71. T. Sakai, Y. Watanabe, and H. Utsunomiya, *Materials Science Forum*, 618-619 (2009), 483–486.

72. M. Pérez-Prado, J. del Valle, J. Contreras, and O. Ruano, *Scripta Materialia*, 50 (5) (2004), 661–665.

73. N. Stanford and M. Barnett, *International Journal of Plasticity*, 47 (2013), 165–181.

74. W. Chen, Y. Yu, X. Wang, E. Wang, and Z. Liu, *Materials Science and Engineering: A*, 575 (2013), 136–143.

75. M. Masoumi and M. Pekguleryuz, *Materials Letters*, 71 (2012), 104–107.

76. E. Ball and P. Prangnell, *Scripta Metallurgica et Materialia*, 31 (2) (1994), 111–116.

77. Y. Chino, K. Kimura, and M. Mabuchi, *Materials Science and Engineering: A*, 486 (1-2) (2008), 481–488.

78. S. Agnew and J. Nie, *Scripta Materialia*, 63 (7) (2010), 671–673.

79. "Critical Materials Strategy," Tech. rep., U.S. Department of Energy (2011).

80. X. Huang, K. Suzuki, and N. Saito, *Scripta Materialia*, 60 (8) (2009), 651–654.

81. J. Xiong, Z. Chen, L. Yi, S. Hu, T. Chen, and C. Liu, *Materials Science and Engineering: A*, 590 (2014), 60–65.

82. H. Zhang, G. Huang, J. Li, L. Wang, and H. J. Roven, *Journal of Alloys and Compounds*, 563 (2013), 150–154.

83. E. Essadiqi, I.-H. Jung, and M. Wells, *Advances in Wrought Magnesium Alloys*, eds. C. Bettles and M. Barnett (Woodhead Publishing, Cambridge, UK, 2012), chap. 7, 272–303.

84. R. F. Decker, S. Kulkarni, J. Huang, and S. LeBeau, *Magnesium Technology*, eds. E. Nyberg, S. Agnew, N. Neeglameggham, and M. Pekguleryuz (Wiley, 2009), 357–361.

85. J. Huang, T. Arbel, L. Ligeski, J. McCaffrey, S. Kulkarni, J. Jones, T. M. Pollock, R. F. Decker, and S. Lebeau, *Magnesium Technology*, eds. S. Agnew, N. Neeglameggham, E. Nyberg, and W. Sillekens (Wiley, 2010).

86. R. F. Decker, *Solid State Phenomena*, 192-193 (2012), 47–57.

87. F. Czerwinski, a. Zielinska-Lipiec, P. Pinet, and J. Overbeeke, *Acta Materialia*, 49 (7) (2001), 1225–1235.

88. T. D. Berman, W. Donlon, R. F. Decker, J. Huang, T. M. Pollock, and J. Jones, *Magnesium Technology*, eds. W. Sillekens, S. Agnew, N. Neelameggham, and S. Mathaudhu (Wiley, 2011), 599 – 603.

89. T. D. Berman, W. Donlon, R. F. Decker, J. Huang, T. M. Pollock, and J. Jones, *Proceedings of the 9th International Conference Magnesium Alloys and Their Applications*, eds. W. J. Poole and K. Kainer (ICMAA2012, Vancouver, Canada, 2012), 571–578.

90. T. D. Berman, W. Donlon, V. M. Miller, R. F. Decker, J. Huang, T. M. Pollock, and J. Jones, *Magnesium Technology*, eds. S. Mathaudhu, W. Sillekens, N. Hort, and N. Neelameggham (Wiley, 2012), 339–344.

91. T. D. Berman, W. Donlon, C. K. Hung, P. Milligan, R. F. Decker, T. M. Pollock, and J. W. Jones, *Magnesium Technology* (2013), 113–118.

92. T. D. Berman, W. Donlon, R. Decker, T. M. Pollock, and J. W. Jones, *Magnesium Technology* (2014), 161–166.

93. F. Kaiser, D. Letzig, J. Bohlen, A. Styczynski, C. Hartig, and K. Kainer, *Materials Science Forum*, 419-422 (2003), 315–320.

94. A. Jager, P. Lukáč, V. Gartnerova, J. Haloda, and M. Dopita, *Materials Science and Engineering: A*, 432 (1-2) (2006), 20–25.

95. R. K. Nadella, I. Samajdar, and G. Gottstein, *Magnesium: Proceedings of the 6th International Conference Magnesium Alloys and Their Applications*, ed. K. Kainer (Wiley, 2005), 1052–1057.

96. G. Gottstein and T. Al-Samman, *Material Science Forum*, 495-497 (2005), 623–632.

97. X. Yang, H. Miura, and T. Sakai, *Transactions of Nonferrous Metals Society of China*, 31 (2007), 1139–1142.

98. S. Wang, S. B. Kang, and J. Cho, *Journal of Materials Science*, 44 (20) (2009), 5475–5484.

99. H. Chao, H. Sun, W. Chen, and E. Wang, *Materials Characterization*, 62 (3) (2011), 312–320.

100. X. Huang, K. Suzuki, and Y. Chino, *Journal of Alloys and Compounds*, 509 (14) (2011), 4854–4860.

101. X. Huang, K. Suzuki, and Y. Chino, *Materials Science & Engineering A*, 538 (2012), 281–287.

102. L. W. F. Mackenzie, G. W. Lorimer, F. Humphreys, and T. Wilks, *Materials Science Forum*, 469-470 (2004), 477–482.

103. X. Huang, K. Suzuki, Y. Chino, and M. Mabuchi, *Journal of Materials Science* (2012), 4561–4567.

104. C. Su, L. Lu, and M. Lai, *Philosophical Magazine*, 88 (2) (2008), 181–200.

105. A. Galiyev, R. Kaibyshev, and G. Gottstein, *Acta Materialia*, 49 (2001), 1199–1207.

106. H.-W. Huang, H.-T. Lee, K.-S. Chan, B.-L. Ou, and C.-J. Chang, *Proceedings of the 9th International Conference Magnesium Alloys and Their Applications*, eds. W. J. Poole and K. Kainer (ICMAA2012, Vancouver, Canada, 2012), 1109–1114.

107. M. Masoumi, F. Zarandi, and M. Pekguleryuz, *Scripta Materialia*, 62 (11) (2010), 823–826.

108. F. Habiby and F. Humphreys, *Textures and Microstructures*, 20 (1977) (1993), 125–140.

109. J. W. Senn and S. Agnew, *Magnesium Technology*, eds. M. Pekguleryuz, N. Neeglameggham, R. Beals, and E. Nyberg (Wiley, 2008), 153–158.

110. J. P. Hadorn, K. Hantzsche, S. Yi, J. Bohlen, D. Letzig, and S. Agnew, *Metallurgical and Materials Transactions A*, 43 (April) (2012), 1363–1375.

111. A. Farzadfar, M. Sanjari, I. Jung, E. Essadiqi, and S. Yue (2012), 469–473.

112. M. Yoo, *Metallurgical and Materials Transactions A*, 12A (1981), 409–418.

113. J. Koike, T. Kobayahi, T. Mukai, H. Watanabe, M. Suzuki, K. Maruyama, and K. Higashi, *Acta Materialia*, 51 (2003), 2055–2065.

114. M. Barnett, *Materials Science Forum*, 618-619 (2009), 227–232.

115. M. Barnett, *Science And Technology*, 44 (4) (2003), 571–577.

116. T. Obara, H. Yoshinga, and S. Morozumi, *Acta Metallurgica*, 21 (July) (1973), 845–853.

117. M. Barnett, *Materials Science and Engineering: A*, 464 (1-2) (2007), 1–7.

118. V. Meyers, M.A., Vohringer, O., Lubarda, *Acta Materialia*, 49 (19) (2001), 4025–4039.

119. E. Schmid and W. Boas, *PLASTICITY OF CRYSTALS* (F.A. Hughes & CO, London, 1950), 2 ed.

120. J. Koike, Y. Sato, and D. Ando, *Materials Transactions*, 49 (12) (2008), 2792–2800.

121. S. Agnew, J. A. Horton, and M. H. Yoo, *Metallurgical and Materials Transactions A*, 33 (March) (2002), 851–858.

122. D. Wu, R.-S. Chen, and E.-H. Han, *Proceedings of the 9th International Conference Magnesium Alloys and Their Applications*, eds. W. J. Poole and K. Kainer (ICMAA2012, Vancouver, Canada, 2012), 531–538.

123. U. Kocks, C. Tóme, and H.-R. Wenk, *Texture and Anisotropy: Preferred Orientations in Polycrystals and Their Effect on Materials Properties* (Cambridge University Press, Cambridge, UK, 1998).

124. X. Huang, K. Suzuki, A. Watazu, I. Shigematsu, and N. Saito, *Materials Science and Engineering: A*, 488 (1-2) (2008), 214–220.

125. Q. Wang, Y. Chen, M. Liu, J. Lin, and H. J. Roven, *Materials Science and Engineering: A*, 527 (9) (2010), 2265–2273.

126. S. R. Agnew, J. W. Senn, and J. A. Horton, *JOM*, 58 (5) (2006), 62–69.

127. C. Cáceres and D. M. Rovera, *Journal of Light Metals*, 1 (2001), 151–156.

128. M. Barnett, Z. Keshavarz, A. Beer, and D. Atwell, *Acta Materialia*, 52 (17) (2004), 5093–5103.

129. C. R. Hutchinson, J. F. Nie, and S. Gorsse, *Metallurgical and Materials Transactions A*, 36 (8) (2005), 2093–2105.

130. *ASM Handbook: Volume 14 (Forming and Forging)* (ASM, 1990).

131. W. Lankford, S. Snyder, and J. Bausher, *Transactions of ASM*, 42 (1950), 1197–1205.

132. Y. Chino, K. Sassa, A. Kamiya, and M. Mabuchi, *Materials Science and Engineering: A*, 473 (1-2) (2006), 195–200.

133. W. F. Hosford, *Materials Science and Engineering: A*, 257 (1998), 1–8.

134. S. Gall, R. Coelho, S. Müller, and W. Reimers, *Materials Science and Engineering: A*, 579 (2013), 180–187.

135. T. Wu, L. Jin, W. Wu, L. Gao, J. Wang, Z. Zhang, and J. Dong, *Materials Science and Engineering: A*, 584 (2013), 97–102.

136. S. Agnew, C. Tomé, D. Brown, T. Holden, and S. Vogel, *Scripta Materialia*, 48 (8) (2003), 1003–1008.

137. M. Barnett, *Materials Science and Engineering: A*, 464 (1-2) (2007), 8–16.

138. M. Marya, L. G. Hector, R. Verma, and W. Tong, *Materials Science and Engineering: A*, 418 (1-2) (2006), 341–356.

139. Z. Chen, J. Huang, R. F. Decker, S. E. Lebeau, L. R. Walker, O. B. Cavin, T. R. Watkins, and C. J. Boehlert, *Metallurgical and Materials Transactions A*, 42 (5) (2010), 1386–1399.

140. Z. Li, J. Dong, X. Q. Zeng, C. Lu, and W. J. Ding, *Materials Science and Engineering: A*, 466 (1-2) (2007), 134–139.

141. M. Koç, O. N. Cora, R. Snell, R. F. Decker, and J. Huang, *Magnesium Technology*, eds. S. Mathaudhu, W. Sillekens, N. Hort, and N. Neelameggham (Wiley, 2012), 413–418.

142. M. Boba, M. Worswick, R. Mishra, and J. T. Carter, *Proceedings of the 9th International Conference Magnesium Alloys and Their Applications*, eds. W. J. Poole and K. Kainer (ICMAA2012, Vancouver, Canada, 2012), 397–402.

143. C. Dreyer, W. Chiu, R. Wagoner, and S. Agnew, *Journal of Materials Processing Technology*, 210 (1) (2010), 37–47.

144. E. Yukutake, J. Kaneko, and M. Sugamata, *Materials Transactions*, 44 (4) (2003), 452–457.

145. D. Randman, B. Davis, M. L. Alderman, G. Muralidharan, T. R. Muth, W. H. Peter, and T. R. Watkins, *Proceedings of the 9th International Conference Magnesium Alloys and Their Applications*, eds. W. J. Poole and K. Kainer (ICMAA2012, Vancouver, Canada, 2012), 23–28.

146. J. Scott, M. Miles, D. Fullwood, B. Adams, A. Khosravani, and R. K. Mishra, *Metallurgical and Materials Transactions A*, 44 (1) (2012), 512–516.

147. J. T. Carter, P. E. Krajewski, and R. Verma, *JOM*, 60 (11) (2008), 77–81.

148. R. Verma and L. Hector, *Magnesium Technology*, eds. S. Mathaudhu, W. Sillekens, N. Hort, and N. Neelameggham (Wiley, 2012), 289–294.

CHAPTER II

Experimental Procedures

This chapter describes the experimental methods used in this thesis. The Thixomolding, rolling, and annealing processes used to produce TTMP AZ61L sheet are presented. The preparation, procedures, and analysis used to characterize microstructure and mechanical properties are also described.

2.1 Material Production

Thixomolded and Thermomechanically Processed (TTMP) sheet is produced by warm-rolling of a Thixomolded plate followed by subsequent annealing. This section describes the process of each of the three primary steps; Thixomolding, rolling, and annealing.

2.1.1 Thixomolding

Thixomolding is an injection molding process, where the shearing of the liquid metal in the barrel decreases the viscosity (thixotropy), allowing casting to be done at lower temperature. Thixomolding is generally a semi-solid processing route; the injected slurry usually contains a solid fraction of 5 to 60% [1]. The rapid solidifica-

tion rate achieved as a result of the reduced casting temperature leads to finer grain sizes, an isotropic texture, refined secondary phases, low porosity, and a relatively homogeneous microstructure [2, 3].

For this research, thirty plates with dimensions of 20.3 cm x 20.3 cm x 3 mm were produced with a 280 ton commercial Thixomolder. The Thixomolder was run with a maximum barrel temperature of 638°C and a screw injection speed of 305 cm/s. The Thixomolding parameters were selected by Thixomat, LLC to achieve low porosity and low ($< 5\%$) solid fraction. Argon was used as the cover gas in the barrel. The nominal composition of the Thixomolded plates, as determined by spectrographic chemical analysis by Dead Sea Magnesium, is given in Table 2.1.

Table 2.1: Composition of received AZ61L in wt %

Al	Zn	Mn	Si	Fe	Mg
6.5	0.46	0.14	0.01	0.003	bal.

2.1.2 Rolling

Twenty five of the thirty Thixomolded plates were rolled to produce sheet using a mill with 150 mm diameter x 150 mm wide rolls. During the rolling process, the bottom plate and rollers were held at 245°C and 195°C, respectively. A proprietary lubrication was used. The plates were preheated for 5 minutes at 315°C and then warm-rolled in a single-pass with a feed rate of 50.8 mm/s to produce a final sheet thickness of 1.8 mm, a thickness reduction of 42%. The rolled sheets were allowed to cool to room temperature in ambient air. Fourteen of the TTMP sheets were used for this dissertation.

The strain rate during rolling is approximately 1.4 s^{-1} as estimated by:

$$\dot{\epsilon} \simeq 0.9V\sqrt{\frac{r}{Dt}} \tag{2.1}$$

where V is the velocity, expressed in mm/s, r is the reduction in thickness as a decimal, D is the roll diameter in mm, and t is the initial thickness in mm [4].

2.1.3 Thermal Treatment

Thermal exposures below 300°C were conducted in a Techne SBL-2D fluidised bath with an alumina media. A thermocouple placed in contact with the sample monitored the temperature, which was stable to ± 2°C. Higher temperature annealing treatments were performed in a Lindberg tube furnace. Temperature was again monitored with a thermocouple in contact with the sample. Annealed samples were water quenched.

2.2 Microstructural Characterization

Optical, scanning electron and transmission electron microscopies were used to characterize the microstructure. This section details the sample preparation procedures and analysis techniques utilized.

2.2.1 Sample Preparation

As magnesium and its alloys are quite difficult to prepare reproducibly for metallographic study, considerable detail is presented. Sample preparation for all microstructure characterization (excluding fractography) differs only in the final step. Metallographic specimens were prepared by using a Buehler EcoMet 250 automatic

grinder-polisher with samples embedded in 31.8 mm diameter cold mount epoxy resin. Settings on the polishing system were 150 rpm base speed, 60 rpm head speed, complementary rotation, and 25 N of pressure. The specimens were ground until planar using 200 grit SiC with water lubricant, and then ground for 30 s each with 400, 600, 800, and 1200 grit SiC with water. If at any of these grinding steps the surface was not uniform, the SiC paper was replaced and the sample was ground for another 30 s. The samples and sample holder were rinsed thoroughly with water between each step. To prevent oxidation, water was avoided after grinding.

All polishing was performed using either Lapmaster (6 μm) or Buehler (3 μm and 1 μm) diamond pastes on Buehler Chemomet pads with the Buehler MetaDi Fluid lubricant. The sample was polished at 6 μm for 10 minutes, and for 5 minutes at the 3 μm and 1 μm steps. Between steps the sample was rinsed well with ethanol, blown dry with an air gun, and then set in front of a low speed air dryer for a few minutes. The pads were cleaned by rinsing with ethanol while gently scraping with the edge of a scoopula before being returned to a ventilated storage box. Between polishing steps the sample holder was rinsed thoroughly with water, and dried with paper towel. Clean gloves were applied at every polishing step. In order to clean and dry the samples as quickly as possible, only two specimens were polished at one time.

To reveal grain boundaries, wrought material was etched for 3 s at room temperature in a picral solution composed of 10 mL water, 10 mL acetic acid, 4.3 grams of picric acid, and 70 mL of ethanol. For the as-Thixmolded material, etching for 3-5 s in a ~ 5°C solution of 60 mL ethanol, 20 mL water, 15 mL glacial acetic acid, and 3 mL of nitric acid produced the best results. The acetic-nitric solution was also used to best reveal the β-particle morphology and as the final preparation step for

electron backscatter diffraction (EBSD). No etchant was used on samples intended for microprobe analysis or backscattered electron (BSE) imaging.

To avoid oxidation, samples were usually prepared immediately before examination. For general optical and SEM analysis, the sample surface was of sufficient quality for approximately 2 weeks following preparation. For EBSD analysis, surface oxidation caused the pattern quality to decrease in as little as two hours following etching when stored in a sample box with desiccant. A $\sim$ 33% reduction in the average confidence index (confidence of the software that the chosen orientation correctly represents the real orientation) in samples that were re-examined 1-7 days after preparation was common. In order to obtain the highest quality EBSD data, an effort was made to have the sample in the SEM vacuum chamber within 0.25 h of etching.

2.2.2 Optical Microscopy

Optical microscopy was performed on an Nikon Epiphot inverted microscope equipped with a digital camera.

2.2.3 Scanning Electron Microscopy (SEM)

SEM examination was conducted with a Philips XL30 field emission gun (FEG) SEM and a Tescan Mira FEG microscope. Both microscopes are equipped with a backscattered electron detector, an EDAX energy dispersive spectroscopy (EDS) detector, and an EDAX electron backscatter diffraction camera. EDAX TSL OIM data collection and EDAX TSL OIM analysis software were used on both systems. Each of these detectors was utilized to characterize different aspects of the microstructure.

Wavelength Energy Dispersive Spectroscopy

A Cameca SX100 electron microprobe was used to quantify the Al concentration in a few of the samples. An accelerating voltage of 15 keV and a probe current of 10 nA was used, resulting in an estimated spot size of 2 μm. The samples and calibration standards were carbon coated prior to analysis. The chemical composition is calculated as the average of 10 point counts (1 minute in duration) at the grain interiors.

Particle Size and Volume Fraction

Secondary electron imaging (SEI) was used to characterize the size and volume fraction of the β-phase particles. Typical microscope operating conditions were an accelerating voltage of 15 keV and a working distance of 5 to 15 mm. At least 20 secondary electron images with an area of 2500 μm^2 were used per condition. A representative microstructure is shown in Figure 2.1.

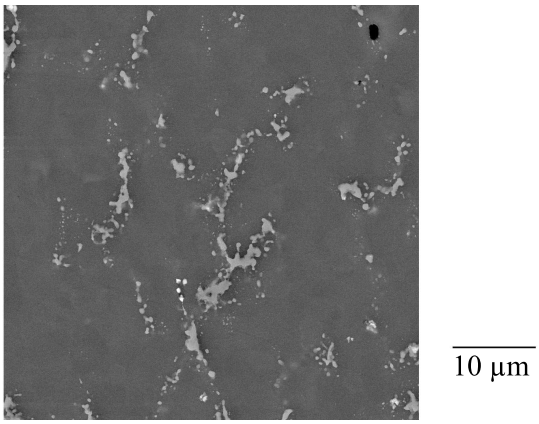

Figure 2.1: SE image used for determination of β-particle size and area fraction. This particular micrograph represents sheet annealed for 285°C for 10 min. The rolling direction is vertical.

ImageJ software [5] developed by the National Institutes of Health was utilized for segmentation and quantitative analysis of microstructure. After the pixels per micron ratio was calibrated, the greyscale threshold was adjusted so that, as much as possible, only the particles appear black (Figure 2.2). Inclusion of a few bright pixels in the matrix was usually unavoidable. The "Analyze Particles" function was used to determine the size, aspect ratio, major axis inclination, length along the horizontal and vertical directions for each particle, as well as the area fraction of particles. A lower limit was set on the possible particle size to exclude single pixels, removing most of the erroneously created particles resulting from the threshold setting. For particle size and morphology measurements, particles on the perimeter of the image were excluded. For volume fraction determination, particles on the edges were retained. The "show outlines" option was used so that the particles selected by the software could be compared to the microstructure to confirm the validity of the measurement. Each particle in the outlined image is automatically numbered for reference. Figure 2.3 shows the generally good agreement between a subset of Figure 2.1 and the generated particle outlines. The results from each image were compiled into a single file in order to calculate mean particle size and particle size distributions. The resolution of micrographs used for this technique neglects all secondary particles less than 0.1 μm in diameter.

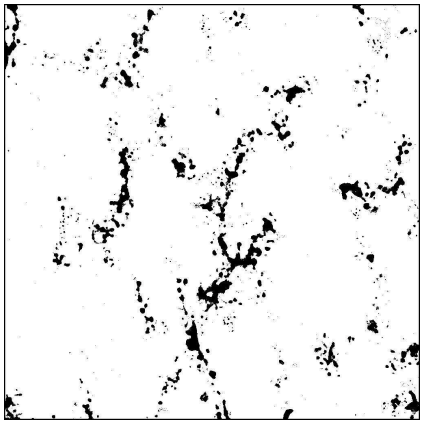

Figure 2.2: Image resulting from adjusting the threshold such that the β-particles are the only remaining feature. This image is 25 μm in width.

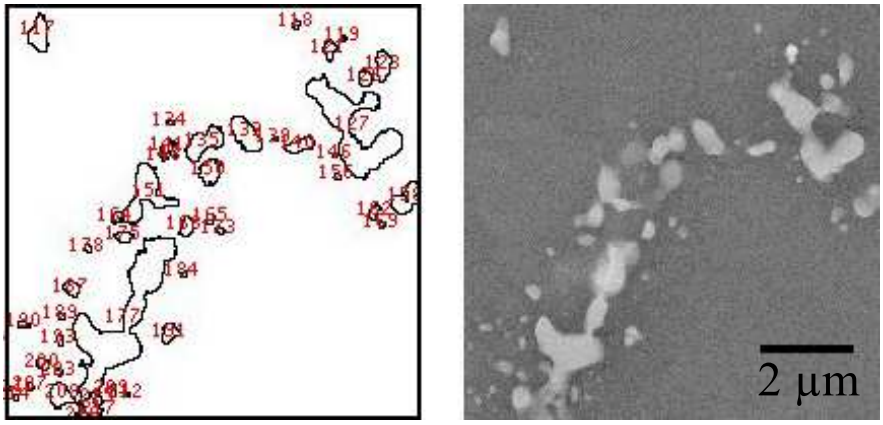

Figure 2.3: Comparison between particles as determined by ImageJ (left) and and the original SE image (right).

Electron Backscatter Diffraction

General operating conditions for EBSD were a working distance between 18 and 20 mm, an accelerating voltage of 30 keV, and a beam intensity of 18. The large accelerating voltage and beam intensity give a predicted spot size of $\sim$ 50 nm and were chosen in order to give the best quality of patterns with a collection rate of 30 to 40 patterns per second. A step size of approximately $^1/_{15}$ of the average grain

diameter and a scan area providing for 500 to 1000 grains was used for most scans. A finer step size of 0.08 μm was used for some of the data sets in which the intention was to study the evolution of grain misorientation during recrystallization.

The general cleaning procedure for EBSD maps was (1) neighbor orientation correlation, (2) one iteration of grain dilation, and (3) grain Confidence Index (CI) standardization. After the cleaning routine, a partition was generated to only retain points with a CI > 0.1. In the TSL OIM analysis program, a CI of 0.1 indicates the software is 90% certain of the grain orientation. Manual examination of the selected pattern for points with a CI < 0.1 usually demonstrates an incorrect match, while points above a CI of 0.1 are a correct match.

A second set of scans was used to determine texture. Here the scan parameters were selected such that the step size would result in an average of 2-5 measurements per grain and that the scan area would sample approximately 10,000 grains. For the highly deformed, as-rolled material and the larger grained solution treated material, a large scan area was needed in order to obtain the desired 10,000 orientations. To avoid the collection of poor patterns due to defocusing as the beam is rastered over the surface in large scans, the orientation information of several smaller scans was merged. It was observed that increasing the scan area from 200 x 200 μm to 400 x 400 μm resulted in a 50% decrease of quality data points in the highly deformed as-rolled material. For larger grained, recrystallized materials, high quality data was obtained on scans as large as 850 x 850 μm. For the large step size EBSD scans intended to only provide texture information, the definition of grain loses validity, and thus the only "cleaning" process was creating a partition to drop all of the low (< 0.1) CI points. The appendix provides a more detailed description of how the texture generated by EBSD compares to that determined by X-ray Diffraction.

Grain Size Determination

The grain size distribution for each condition was determined from the EBSD data. After the routine cleaning procedure, the grain properties in the OIM software were modified to require grains to contain at least 10 points and occupy multiple rows of the scan. A misorientation of $> 5^\circ$ was used to define a grain boundary. Extension twin boundaries of $\{10\bar{1}2\}\langle 10\bar{1}1\rangle$ at $86^\circ \pm 3^\circ$ were included in the parent grain size. The resulting EBSD data and grain properties were used to construct an inverse pole figure map. Black grain boundaries were superimposed on the map. The ImageJ software was used to threshold these images such that only the grain interiors remained black and the "Analyze Particles" function could be used. At least 1000 grain area measurements were collected. Circular grains were assumed in order to convert grain area to grain diameter.

2.2.4 Transmission Electron Microscopy (TEM)

Sample preparation for TEM consisted of first thinning a $\sim$ 10 mm by 30 mm coupon of material to less than 300 μm in thickness. 3 mm diameter disks were then punched from the sheet using a Gatan foil punch. These disks were ground with 1200 grit SiC with ethanol as lubrication, and polished with diamond pastes to 1 μm on both sides; the foil thickness after polishing was between 70 and 100 μm. A Gatan Precicion Ion Polishing system was used to thin the sample to electron transparency. The thinning was done in two steps, one at a gun tilt of 5° at 4.5 keV until a hole formed (this usually required about 10 hours) and a lower energy step at 3° and 3.0 keV for 20 minutes to remove some of the damage from the first step. A liquid

nitrogen cold finger was used to cool the foil during the entire process.

TEM was conducted on either a Phillips CM12 AEM or a JEOL 2010F TEM. Both microscopes were equipped with a double-tilt holder.

2.3 Mechanical Testing

Both hardness and tensile tests were used to evaluate mechanical properties. This section describes the specimen geometry, preparation, and testing procedures used.

2.3.1 Tensile Tests

Dogbone tensile specimens with a gauge length of 25.45 mm and a width 6.35 mm were machined from a total of twelve sheets and one plate. In the sheets, specimens were machined with the tensile axis oriented at either 0°, 45°, and 90° from the rolling direction. The specimen thickness was equal to the material thickness, 3 mm for the Thioxmolded plates and $\sim$ 1.8 mm for the sheets. Annealing treatments were always conducted after machining. An oxide layer that formed during annealing on some of the solution treated samples was removed with 1200 grit SiC before testing. A few samples were polished before deformation to allow for evaluation of shear band activity.

Room temperature tensile tests were performed with an Instron 5505B load frame equipped with a 100 kN load cell. A constant displacement rate of 0.01 mm per second resulted in an initial strain rate of $4x10^{-4}s^{-1}$. The samples were preloaded to 20 MPa to remove the rolling curvature. An extensonometer with a 25.4 mm gage was used to measure tensile elongation. At least 4 specimens for each condition were loaded monotonically to failure. The yield strength was calculated using a 0.2%

offset.

Three additional samples, strained to 10% were used to calculate the r-value (r), the mean r-value ($\bar{r}$) and the planar anisotropy of r-value (Δr) which are given by:

$$r = \epsilon_w/\epsilon_t \tag{2.2}$$

$$\bar{r} = |r_0 + 2 * r_{45} + r_{90}|/4 \tag{2.3}$$

$$\Delta r = |r_0 - 2 * r_{45} + r_{90}|/2 \tag{2.4}$$

where ϵ_w and ϵ_t are the strains in the width and thickness directions, respectively and the subscripts indicate the orientation of the tensile axis with respect to the rolling direction [6].

In order to observe damage accumulation during deformation, interrupted tensile tests were also conducted. The tensile tests were stopped at the desired strain and ~ 50 μm was removed from the surface by grinding and polishing to 1 μm to remove topology before examination via SEM. The first set of interrupted tests examined deformation at 1%,2%, 4%, 8%, and 16% plastic strain. No damage was observed at 1% or 2%, so these steps were dropped in further studies.

Crack length and crack density information was collected on nominally twenty BSE micrographs at each strain increment. The micrographs were taken along the polished surface beginning at one of the gauge ends and then at 1 mm intervals towards the opposite end of the specimen. Each image had a field of view of approximately 1000 μm^2, resulting in a resolution of 33.2 pixels per μm. Crack length was measured using ImageJ.

The fracture surfaces were inspected both optically and in the SEM. In several cases, one piece of the specimen was polished to either mid-width or mid-thickness

to characterize the damage at failure by BSE imaging. Twinning was studied as a function of strain in several mid-thickness samples following etching in the picral solution described in 2.2.1.

2.3.2 Hardness

Vickers microhardness measurements were made with a Clark Microhardness tester with a dwell time of 15 s and a 200 g load. At least 10 measurements were taken per condition.

Bibliography

1. F. Czerwinski, *Materials Science and Engineering: A*, 392 (1-2) (2005), 51–61.
2. R. F. Decker, *Solid State Phenomena*, 192-193 (2012), 47–57.
3. F. Czerwinski, a. Zielinska-Lipiec, P. Pinet, and J. Overbeeke, *Acta Materialia*, 49 (7) (2001), 1225–1235.
4. W. Roberts, *Cold Rolling of Steel* (MARCEL DEKKER, INC., New York, 1978).
5. C. A. Schneider, W. S. Rasband, and K. W. Eliceiri, *Nature Methods*, 9 (7) (2012), 671–675.
6. W. Lankford, S. Snyder, and J. Bausher, *Transactions of ASM*, 42 (1950), 1197–1205.

CHAPTER III

Microstructure and Texture Evolution Through Thixomolding and Thermomechanical Processing

This chapter describes the evolution of the microstructure through the TTMP process, starting from the as-Thixomolded plate pre-cursor to annealed TTMP sheets. The α-Mg grain size and β-particle size, volume fraction, and distribution are discussed. Recrystallization in the rolled sheet is characterized, and the kinetics of recrystallization are determined. Grain size stability during annealing is also be examined.

3.1 Microstructure of Thixomolded Plate

Thixomolded plate was chosen as the precursor for rolling because produces a microstructure composed of fine α-Mg grains (darker grey) surrounded by blocky β-particles and some divorced β-eutectic (brighter grey) (Fig. 3.1). The average grain diameter of the as-Thixomolded material is 4.3 μm, but as shown in Figure 3.2, the grain size distribution is broad. There are some grains as large as 20 μm in diameter. The cast plate is essentially untextured, which was desirable to aid in producing rolled sheet with low texture (Figure 3.3).

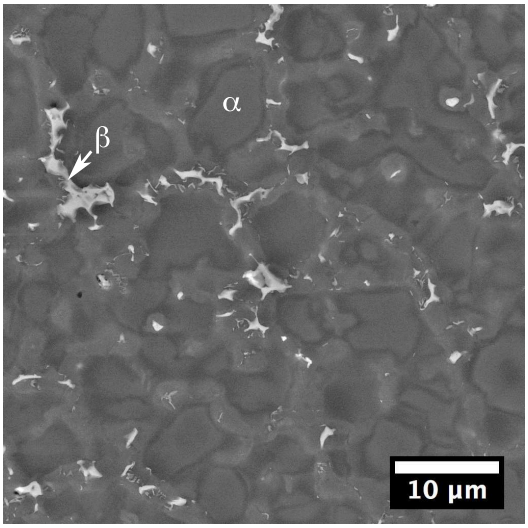

Figure 3.1: Representative microstructure of the as-molded plate.

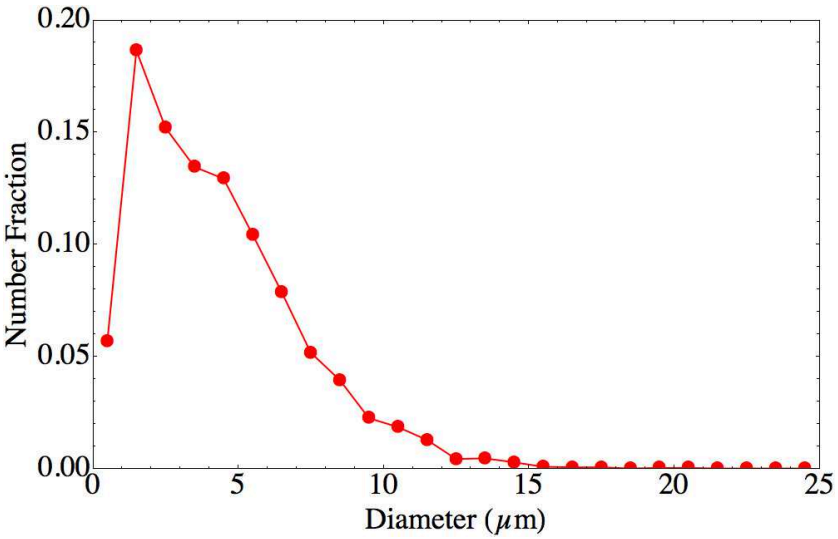

Figure 3.2: Grain size distribution of > 4000 grains in the as-molded plate.

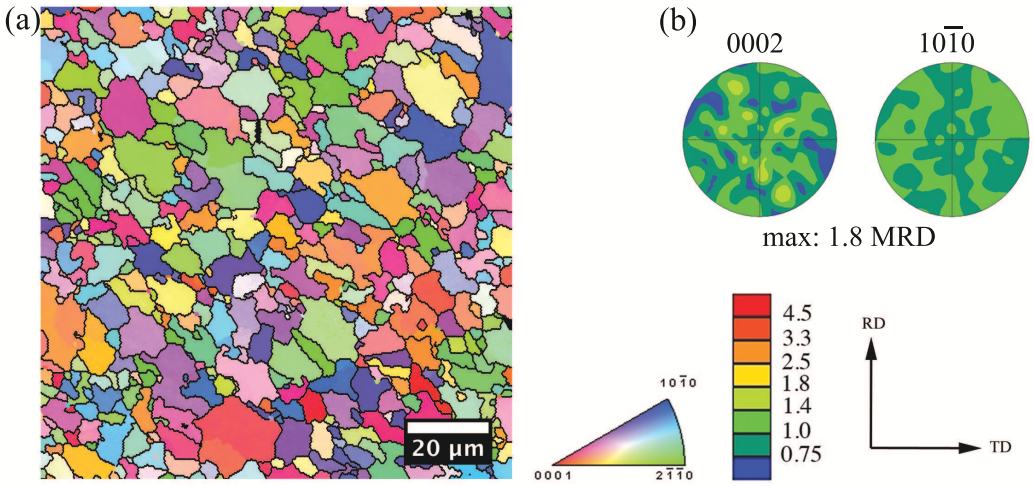

Figure 3.3: (a) Inverse pole figure map and (b) basal and prismatic pole figures representing the as-molded plate. EBSD data courtesy of Victoria Miller of UCSB.

The rapid cooling rate during Thixomolding leads to a supersaturation of aluminum and results in an average volume fraction of β-phase of only 4.2%, compared to 10% at equilibrium, as determined by area fraction measurements. It should be noted that determination of the β-phase volume fraction by area fraction neglects β-particles finer that 200 nm in diameter, however the analysis of the phase fractions by XRD yielded a similar β-phase volume fraction of 3%. Aluminum is likely segregated to regions in the vicinity of the grain boundary, an average Al concentration of 3.6 wt.% was measured in the grain interiors by wavelength dispersive spectroscopy. The β-particles are distributed primarily along grain boundaries, and have an average diameter of 1 μm. Figure 3.34 illustrates a typical β-particle morphology in the as-molded condition.

There are also some large grains 50 to 100 μm in diameter, as shown in Figure 3.5, which likely solidified in the nozzle of the Thixomolding machine at a higher temperature and thus contain less Al [1]. These externally solidified grains tend to

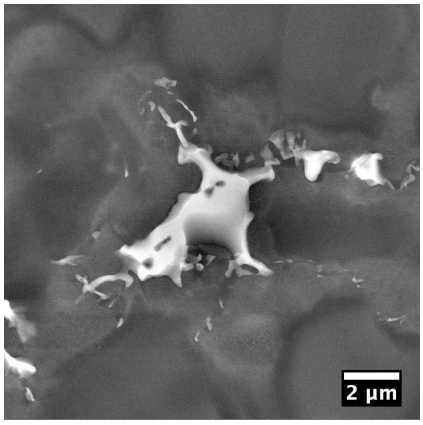

Figure 3.4: Typical β-particle morphology of one of the larger particles in the as-molded condition.

be segregated in bands in the plate thickness. The average volume fraction of these grains is $\sim 4\%$.

Thixomolding is generally a semisolid processing, with a solid fraction of 5 to 60%, though components have been made successfully with a solid fraction of 85% [2]. The solid particles promote more laminar flow, reducing porosity, though lower solid fractions (5 to 10%) are generally employed for thinner components [2].

Both elongation to failure and tensile strength have been shown to increase with decreasing solid fraction, and therefore the Thixomolded plates for TTMP were processed to have a solid fraction less than 5% [3, 4]. Although they persist through processing in TTMP AZ61, no correlation between these externally solidified grains and damage and failure of the as-molded or TTMP sheets was observed. This is consistent with work by Nandy et al.. [3], in which particle-matrix decohesion was infrequent, even in alloys with solid fractions of 30%. Based on the work of Nandy et al.., and the low solid fraction in TTMP AZ61, it is assumed that these particles play a limited role in the deformation behavior of TTMP AZ61 and their evolution through processing is not addressed.

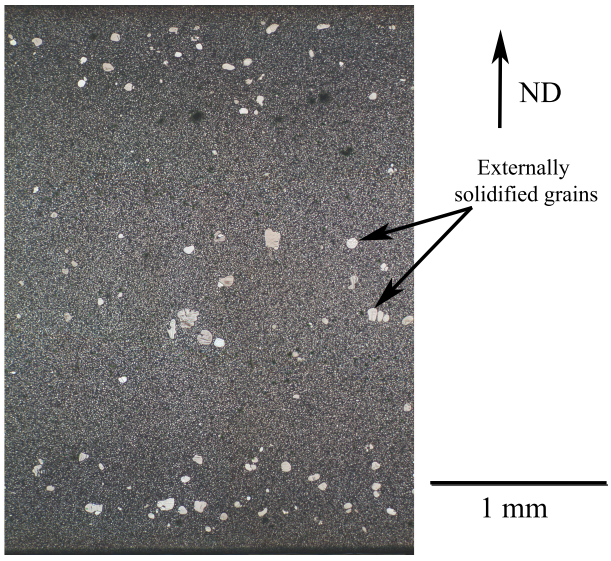

Figure 3.5: Optical micrograph revealing the distribution of bright, externally solidified grains through the thickness of the as-molded plate.

A small amount of porosity, highlighted in Figure 3.6, exists in the as-molded plate. A few of these casting pores are highlighted by white arrows in Figure 3.6. Thixomat, LLC measured a porosity of 1.5% in the Thixomolded AZ61 plates by the Archimedies method. Though a detailed characterization of the porosity was not conducted, visual inspection of the area fraction of pores seems to be consistent with the measured porosity level.

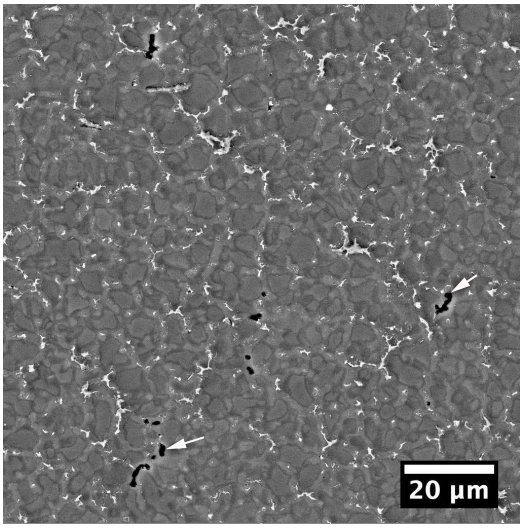

Figure 3.6: SE micrograph showing porosity in the as-molded microstructure.

3.2 Microstructure of as-Rolled Sheet

The rolling process produces highly deformed grains elongated in the rolling direction. No grain boundaries or equiaxed grains are observable in the microstructure by SEM (Figure 3.7). The deformed state of the as-rolled sheet yields generally poor EBSD pattern quality. Figure 3.8 illustrates an inverse pole figure (IPF) map, generated by EBSD, for the as-rolled sheet. Black pixels indicate that an orientation could not be determined at that location. Possible causes for a lack of indexing are the presence of a β-particle, shadowing by topography, overlapping diffraction patterns at grain boundaries, and poor pattern quality due to a high dislocation content in the material. An indexing rate of less than 40% of the points is common in the as-rolled material.

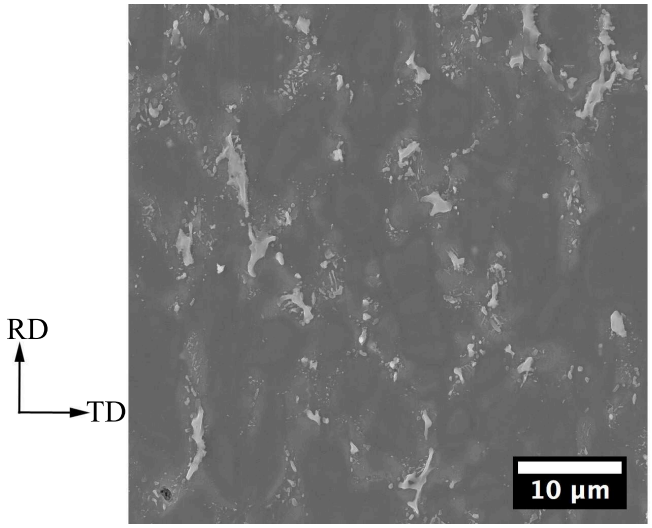

Figure 3.7: Representative scanning electron micrograph of the as-rolled microstructure.

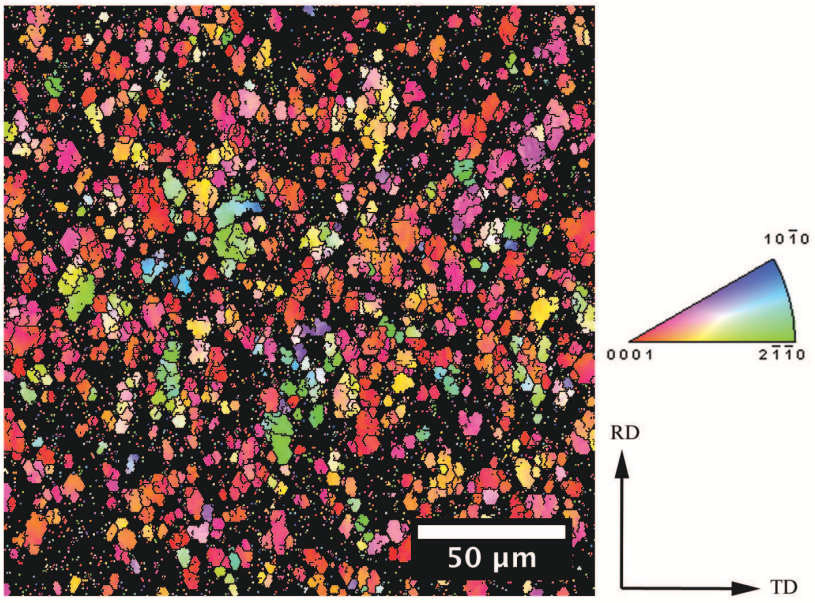

Figure 3.8: IPF map representing the as-rolled sheet. The black pixels are points that could not be indexed. The black lines indicate boundaries with a 5 ° misorientation.

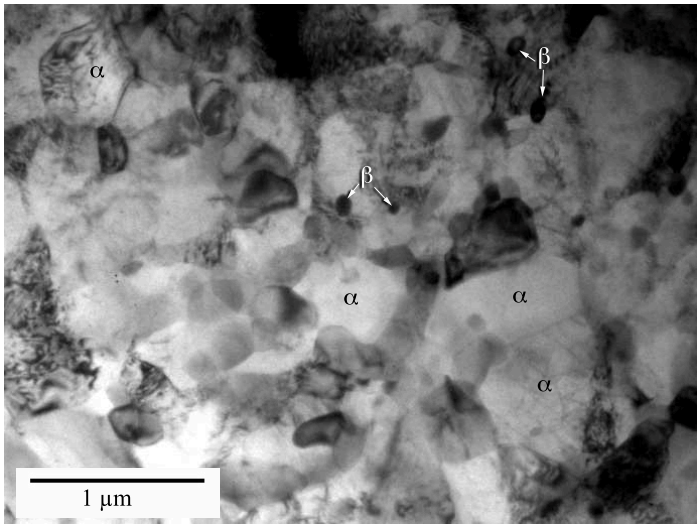

Figure 3.9: Transmission electron micrograph of a region containing several dynamically recrystallized grains indicated by α.

Transmission electron microscopy of as-rolled microstructure reveals regions of dynamically recrystallized grains (Figure 3.9). The dynamically recrystallized regions appear to be associated with regions with a numerous β-precipitates, though a rigorous analysis of the relationship between dynamically recrystallized grains and β-precipitates was not established. The majority of the microstructure contains a high density of dislocation networks (Figure 3.10(a)). Figure 3.10(b) illustrates one region in which a highly deformed grain (labeled A) neighbors a region of fine dynamically recrystallized α-Mg grains and β-particles (labeled B). Due to the complexity of the microstructure, and the inherently small area that can be examined via TEM, a dynamically recrystallized grain size was not rigorously determined, but an average dynamically recrystallized grain diameter of 0.5 μm appears reasonable.

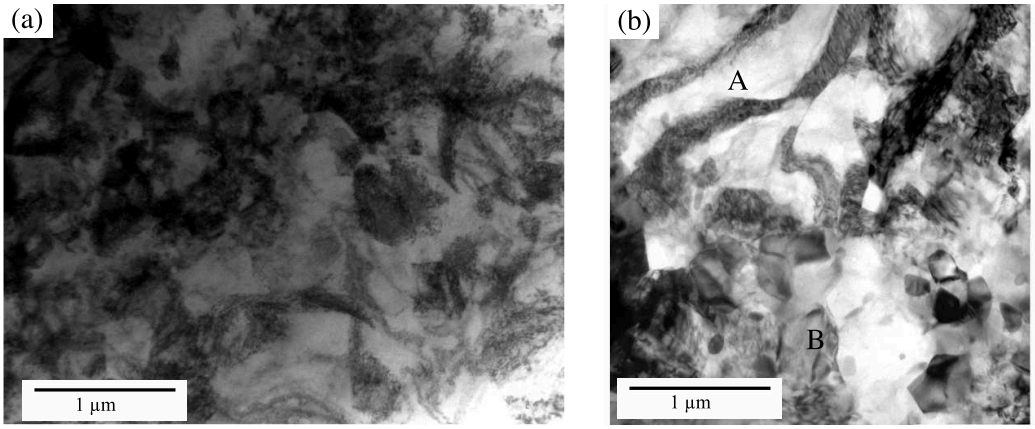

Figure 3.10: Transmission electron micrographs showing the complexity of the as-rolled sheet microstructure. (a) The typical microstructure via TEM in the as-rolled condition and (b) a deformed grain neighboring a region of sub-micron dynamically recrystallized grains and β-precipitates.

In the as-rolled sheet, the volume fraction of the β-phase increased to 7.6% from 4.2% in the as-molded plate. This results from the additional time at temperature during the preheat (315°C) and rolling process. Rolling results in the tendency for the β-particles to be arranged in chains aligned roughly parallel to the rolling direction. Finer β-precipitates observed via TEM (Figure 3.9) have a platelet shaped geometry consistent with that observed by TEM in AZ91 [5]. These finer β-precipitates are heterogeneously distributed throughout the microstructure. The evolution of the β-phase during TTMP is discussed in more detail in Section 3.6.

3.3 Recrystallization in TTMP AZ61 Sheet

Recrystallization treatments were performed in order to recover ductility loss due to the high dislocation density in the as-rolled sheet. In order to quantify the recrystallization kinetics, both isochronal and isothermal annealing treatments were conducted. A modified Johnson-Mehl-Avrami-Kolmogorov (JMAK) recrystallization model gives a reasonable description of recrystallization in the as-rolled TTMP sheet [6–8].

3.3.1 Isochronal Recrystallization Treatments

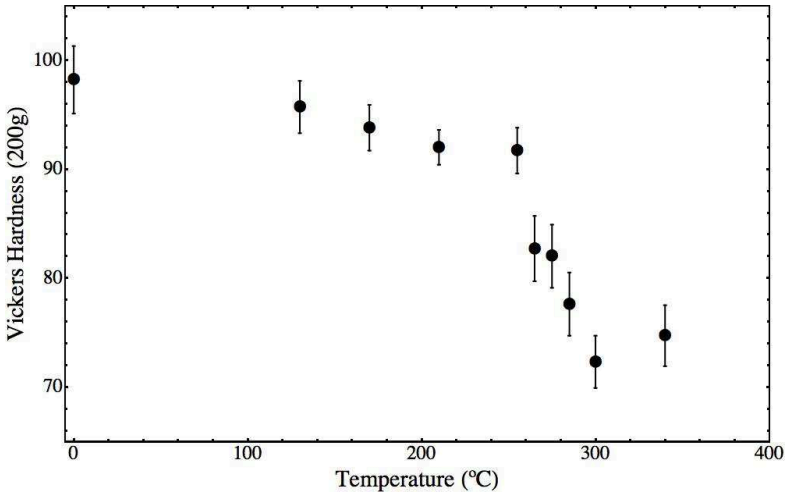

Figure 3.11: Evolution of hardness after 10 minute annealing treatments at temperatures between 130°C and 340°C.

Ten minute annealing treatments at temperatures between 130°C and 340°C were performed on the as-rolled sheet. The resulting hardness evolution is summarized in Figure 3.11. The hardness begins to significantly decrease above 250°C. Based on the premise that the fraction recrystallized (X) is proportional to the amount of softening, we can approximate recrystallization as a function of temperature by Eqn.

3.1 [6, 8–10].

$$X = \frac{H_{max} - H}{H_{max} - H_{min}} \tag{3.1}$$

H, H_{max}, and H_{min} are the hardness, the maximum hardness (cold worked state), and the minimum hardness (recrystallized state), respectively. A value of 95.7 HV, the hardness of sheet that has been annealed at 130°C for 12 hours, is used for H_{max}. Following this low temperature heat treatment, the sheet softens slightly from the as-rolled hardness of 99 HV. Observations of the microstructure after 12 hours at 130°C show no signs of recrystallization, so it is assumed that the reduction in hardness is a result of recovery. H_{min} is approximated as 75.9 HV, the average hardness of the four highest temperature annealing treatments. Figure 3.12 shows the resulting recrystallization curve. From this 285°C was chosen as the recrystallization annealing treatment temperature as it provides a nearly fully recrystallized microstructure ($\sim$ 80% based on hardness) after only 10 minutes and it is lower than the β-solvus for AZ61 ($\sim$ 300°C).

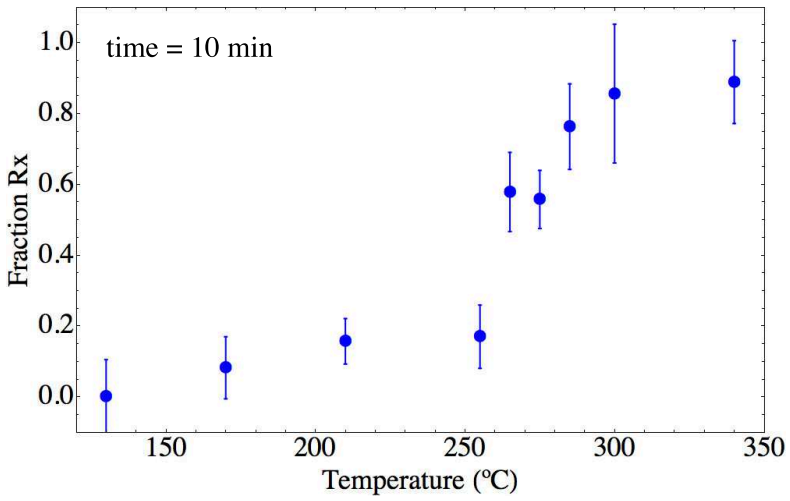

Figure 3.12: Fraction recrystallized in material annealed for ten minutes at temperatures between 130°C and 340°C, as calculated from hardness measurements.

3.3.2 Isothermal Recrystallization Treatments

In order to better understand the recrystallization kinetics at the selected recrystallization temperature of 285°C, an isothermal recrystallization curve was determined for times between 30 and 900 seconds following the same procedure used for the isochronal curve. Figure 3.13 presents the results of this analysis, and Figure 3.14 demonstrates the microstructure evolution during recrystallization. Aside from the value at 480 seconds, which is low compared to its neighboring points, the hardness seems to be relatively stable at times above 360 seconds.

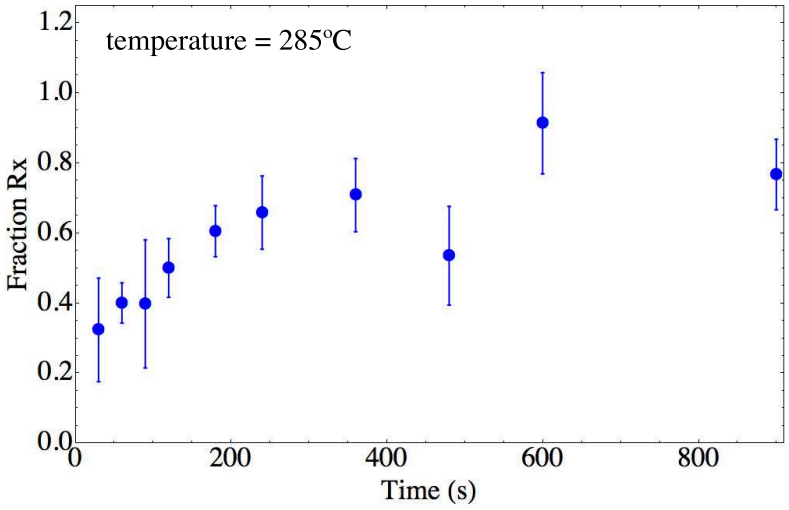

Figure 3.13: Fraction recrystallized in material annealed at 285°C for between 30 and 900 seconds, as calculated from hardness measurements.

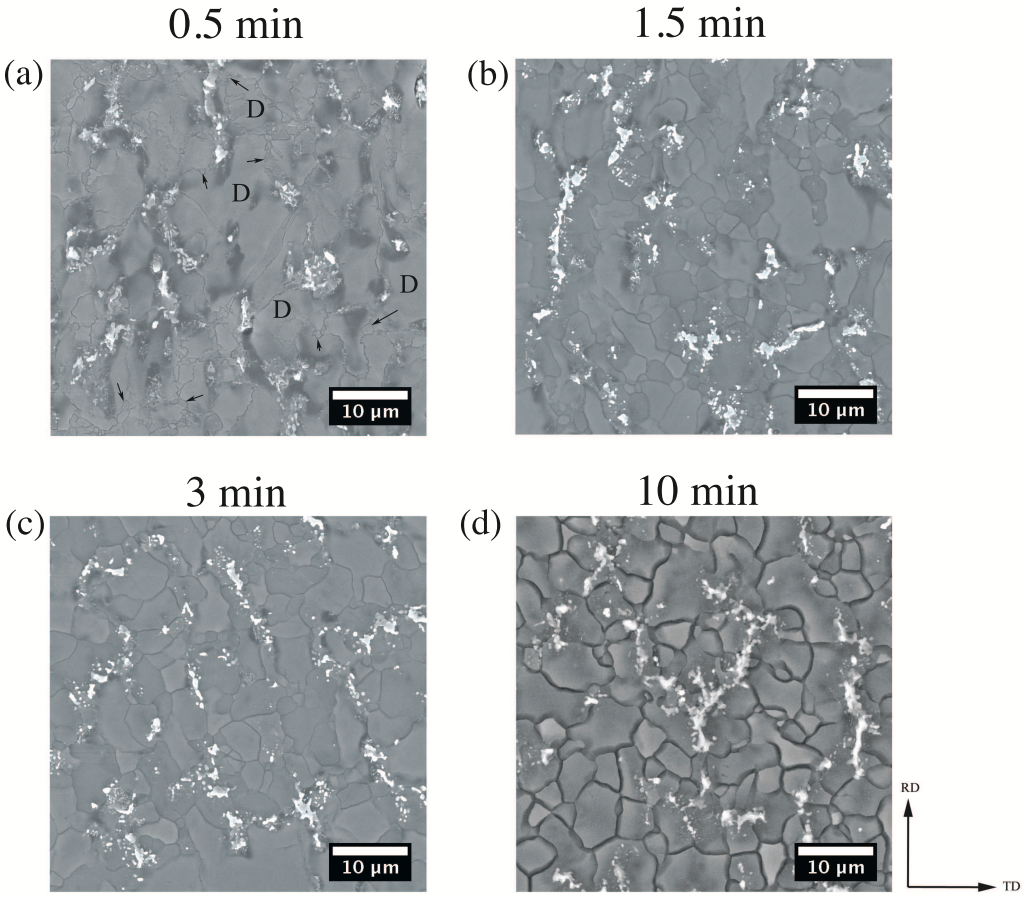

Figure 3.14: Evolution of microstructure during recrystallization at 285°C observed by SEM. Arrows highlight some of the recrystallized grains which surround the deformed grains, some of which are indicated by "D."

3.3.3 Recrystallization Kinetics

Researchers have described recrystallization in Mg reasonably well using JMAK kinetics [6, 11–15]. The JMAK model assumes homogeneous nucleation of recrystallized grains at a constant rate, isotropic growth, and a linear growth rate [8]. If these criteria are satisfied, then the Avrami exponent would be 4 [8, 16]. In reality, nucleation is neither spatially or temporally homogeneous; reported Avrami exponents in AZ31 range between 1.18 and 1.38 [6, 11, 14].

The results from both recrystallization studies in TTMP AZ61 were used to fit a modified Johnson-Mehl-Avrami-Kolmogorov (JMAK) recrystallization model expressed below [6, 7].

$$X = 1 - exp\left(-0.693\left(t/t_{0.5}\right)^{n}\right) \tag{3.2}$$

$$t_{0.5} = BZ^{r}exp\left(Q_{rex}/RT\right) \tag{3.3}$$

Here $t_{0.5}$ is the time to 50% recrystallization, which is calculated using Equation 3.3. Z is the Zener-Hollomon parameter, $Z = \dot{\epsilon} \times exp(Q_{def}/RT_d)$, and R is the ideal gas constant (8.314 $JK^{-1}mol^{-1}$). The activation energy for Mg self-diffusion, 135 $kJmol^{-1}$, is used to approximate, Q_{def}, the activation energy for deformation [6]. T_d, the temperature of deformation, was approximately 300°C. The expressions for $t_{0.5}$ and Z were substituted into Equation 3.2 and fit to the experimental data for the fraction recrystallized (Figure 3.12 and Figure 3.13). A nonlinear regression algorithm was used to solve for n (the Avrami exponent), Q_{rex} (the activation energy for recrystallization), and the fitting constants r and B. The best fit parameters, are presented in Table 3.1. A decrease in the B parameter (to which the isochronal curve is less sensitive) is the only difference from previously reported parameters obtained by considering the isochronal recrystallization curve exclusively [17]. Figure 3.15 displays the resulting JMAK model with the isochronal and isothermal recrystallization curves in as-rolled TTMP AZ61 sheet.

Table 3.1: Parameters used for JMAK model

Parameter	**Value**
n	0.94
Q_{rex}	137 $kJmol^{-1}$
r	-0.87
B	1.63 $s^{0.13}$

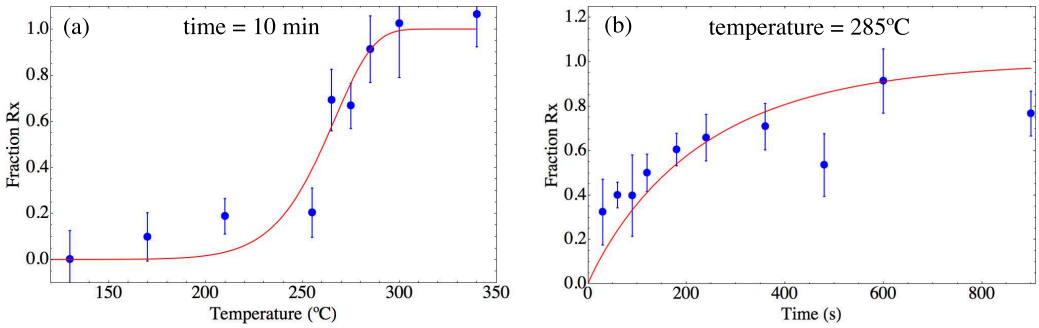

Figure 3.15: JMAK model fit to the isochronal and isothermal recrystallization curves in as-rolled TTMP AZ61 sheet.

The Avrami exponent, n, of 0.94 in the TTMP AZ61 sheet is slightly lower than reported Avrami exponents in AZ31 [6, 11, 14]. This low exponent may be due to non-random nucleation in the deformed material, for instance an exponent of 1 has been found when modeling nucleation of random sites on grain boundaries [18]. Clusters of β particles along grain boundaries may be preferential nucleation sites. Another factor is that the driving force for recrystallization increases with increasing strain and n decreases as dislocation density increases [8, 11].

3.3.4 Low Temperature Annealing Treatments

In order to evaluate the potential for age hardening in the as-rolled sheet, annealing treatments between 5 and 720 minutes were conducted at 130°C, 170°C, and 210°C. The hardnesses resulting from these low temperature annealing treatments are shown in Figure 3.16. Unsurprisingly, no age hardening response is seen in the material with a non-uniform distribution of Al, but the results do provide some insights into the recovery and recrystallization processes in the as-rolled sheet. Unlike at temperatures above 250°C, no substantial decrease in hardness is seen at the low temperatures, even after 12 h. Thus, 210°C is below the recrystallization tempera-

ture in the as-rolled sheet. The 4 HV decrease between the as-rolled material and sheets annealed at the low temperatures can be attributed to recovery.

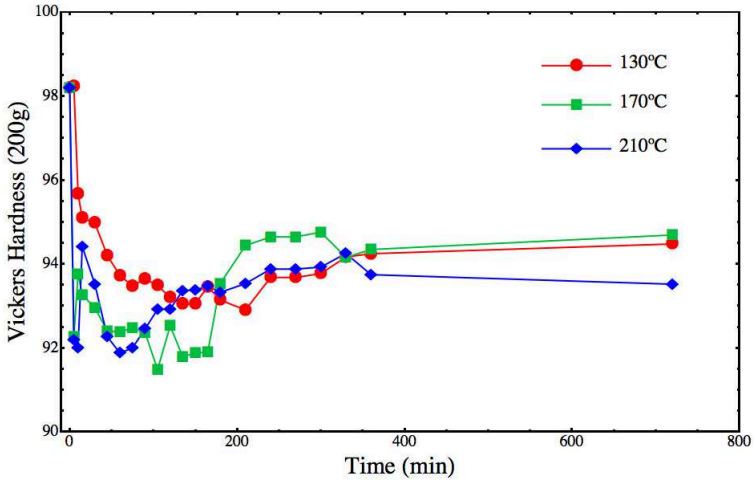

Figure 3.16: Hardness following low temperature annealing treatments.

The recrystallization temperature, T_{RX}, is often defined as the temperature at which the material is 50% recrystallized after 1 hour [8]. Based on this criterion the recrystallization temperature for as-rolled TTMP AZ61 sheet lies between 210°C and 260°C. Our JMAK model would predict T_{RX} to be 230°C. However, since our model is largely based on the kinetics at higher temperatures (with an emphasis at 285°C), it loses validity as the temperature, and therefore energy available for recrystallization, is decreased. Indeed, it would predict that after 12 hours at 210°C the sheet is more than 80% recrystallized, when no evidence of recrystallization after this treatment was detected by hardness measurements or observation of the microstructure (Figure 3.17). The recrystallization temperature is often approximated as either $^1/_3$ or $^1/_2$ the melting temperature, which is 620°C in AZ61 [19]. This predicts a recrystallization temperature between 205°C and 310°C, in agreement with our observations. Recrystallization temperatures between 200°C and 300°C have been reported in Mg and a

wide variety of Mg alloys [11–13, 15, 20–22].

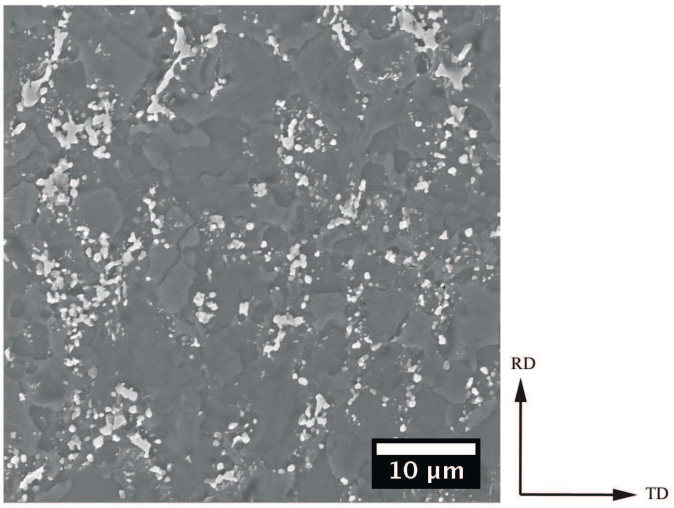

Figure 3.17: SE micrograph presenting the representative microstructure of sheet annealed for 210°C for 12 h demonstrating a lack of grain boundaries which would indicate recrystallization.

3.3.5 Grain Orientation Spread

Another method used to characterize the fraction recrystallized is by calculating the internal misorientation of a subset of grains via EBSD orientation measurements. The grain orientation spread (GOS) is a measure of the mean misorientation of all pixels within a grain from the average grain orientation. Grains with a GOS less than 1.5° or 1° are usually considered recrystallized [22–24]. Figure 3.18 compares GOS maps for sheet annealed for (a) 0.5 min and (b) 10 min at 285°C. As there are no grains in either map with a GOS greater than 10°, this appears to be near the limit for the maximum deformation above which TTMP AZ61 does not produce sufficient image quality for reliable indexing. Using 1° as the cutoff between recrystallized and un-recrystallized grains, a dramatic increase in the fraction of recrystallized grains (blue) from 5% at 0.5 minutes to 63% after 10 minutes is apparent.

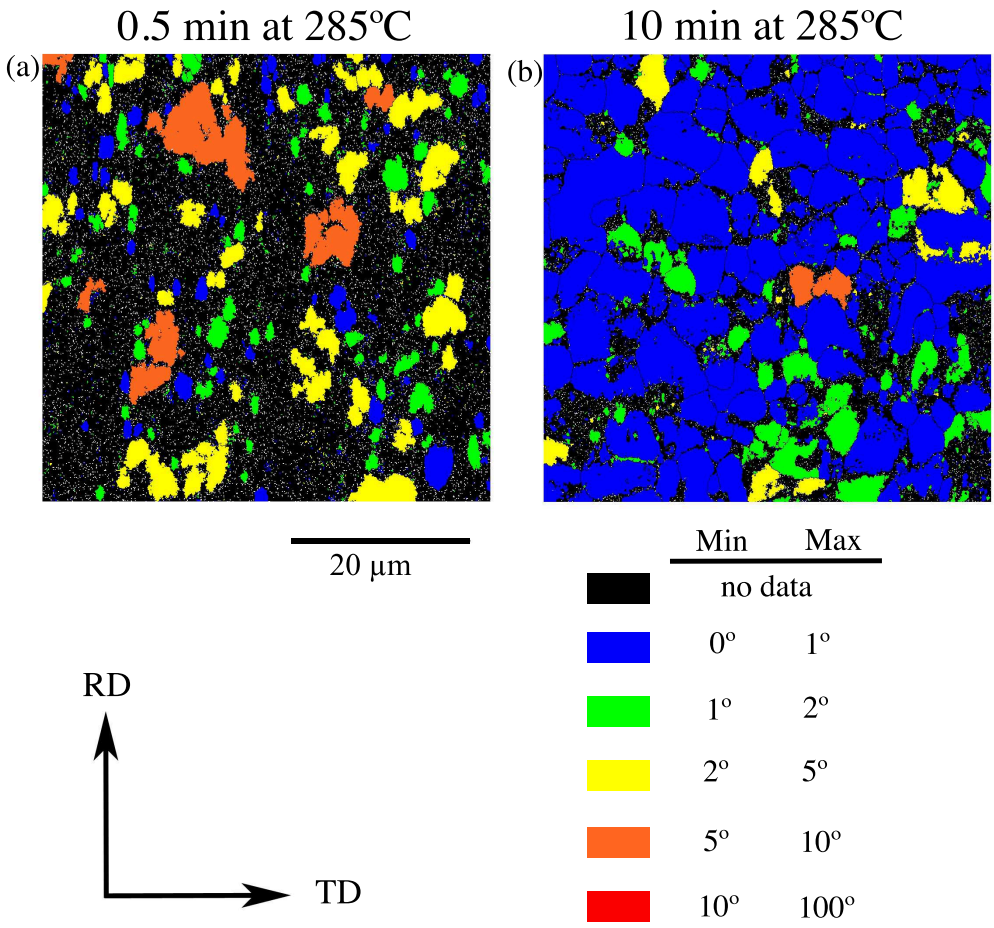

Figure 3.18: Grain orientation spread maps for sheet annealed for (a) 0.5 min and (b) 10 min at 285°C. Grain color indicates the GOS.

It should be noted that these are relatively small maps (50 μm square), collected with the intentions of exploring potential interactions between β-particles and recrystallized grains (to be discussed in Section 3.3.6), and so the fraction of recrystallized grains in Figure 3.18 is not necessarily representative of the material condition. Yet, a larger scan (115 μm square) of the 10 minute anneal at 285°C demonstrates a nearly identical recrystallized fraction of 64% (Figure 3.19). It is common for hardness to predict a higher fraction recrystallized than the GOS method [23]. In the

case of of the 0.5 min and 10 min annealing treatments at 285°C, the hardness based predictions are 20% higher than the fraction determined from the GOS maps.

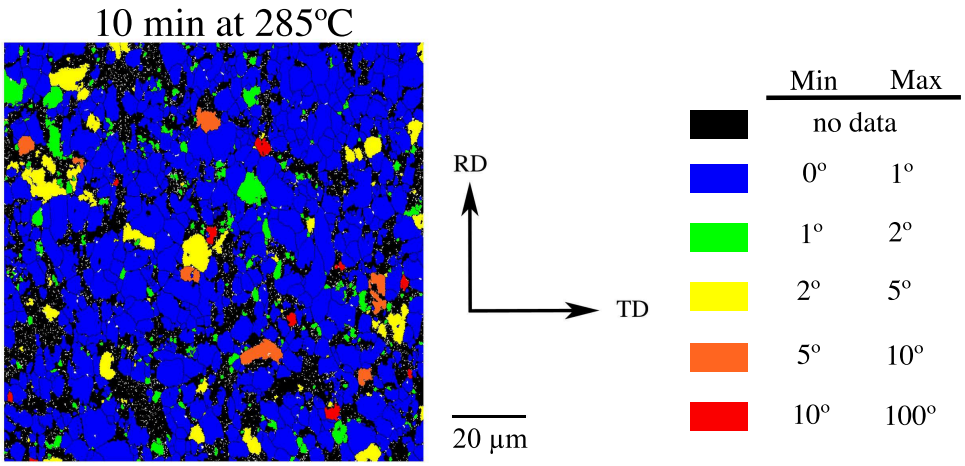

Figure 3.19: Larger grain orientation spread maps for sheet annealed for 10 min at 285°C. Grain color indicates the GOS.

3.3.6 Mechanisms of Recrystallization

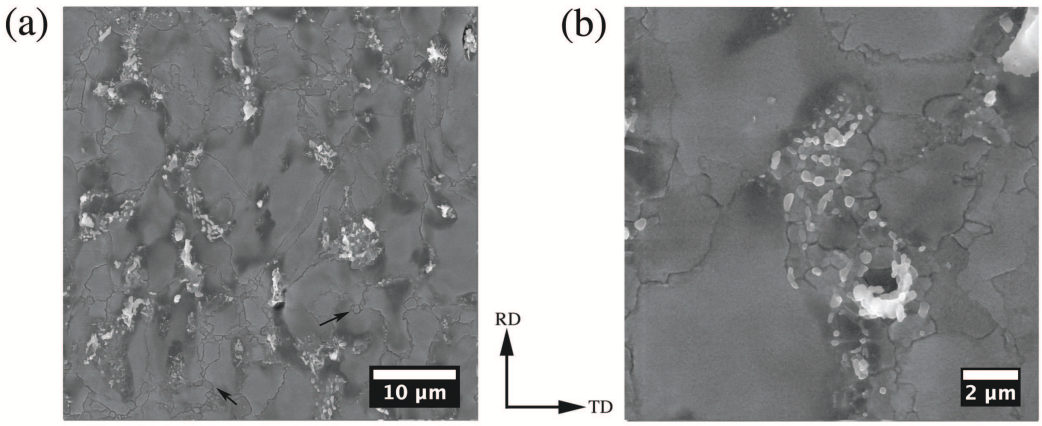

Figure 3.20: SE micrograph of sheet annealed for 0.5 minutes at 285°C featuring (a) the general recrystallization behavior and (b) recrystallization behavior in a cluster of β-particles.

The microstructure of partially recrystallized materials indicates that the recrystallized grains nucleate primarily at grain boundaries. The black arrows in Figure 3.20(a) illustrate some of the recrystallized grains in a necklace structure surrounding the deformed grains. Recrystallized grains also nucleate in regions of dense β-particles (Figure 3.20(b)), but as these particles also tend to lie near grain boundaries, it is difficult to isolate nucleation on grain boundaries versus nucleation on the β-particles themselves. However, the grain boundary serration and obvious pinning of grain boundaries in Figure 3.21 clearly illustrate that the β-particles reduce grain boundary mobility. It is feasible that fine grains in Figure 3.20(b) did not nucleate on the β-particles, but their growth was arrested once their grain boundaries became pinned by the comparatively large β-particles. The microstructure in this region seems to be equivalent to that observed by TEM in Figure 3.9, in that both exhibit the coincidence of a large number of fine ($\sim$ 1 μm) recrystallized grains in a field of β-particles. Our model of recrystallization kinetics indicates that sheets annealed for 285°C for 0.5 minutes and 225°C for 10 minutes are 25% and 8% recrystallized, respectively.

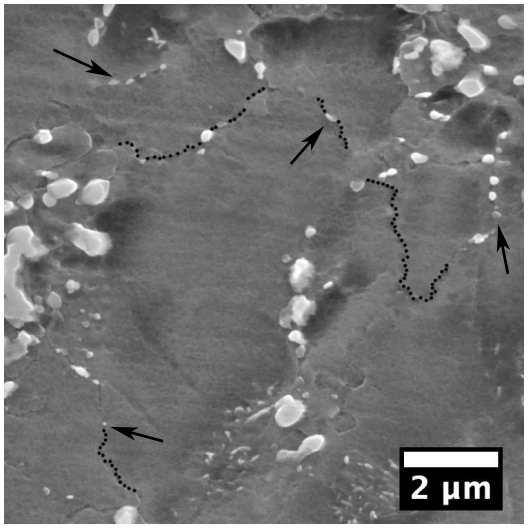

Figure 3.21: SE micrograph of regions of obvious grain boundary pinning by β-particles in sheet annealed for 10 minutes at 225°C. Some of the pinned and serrated grain boundaries are highlighted by dotted lines.

An effort was made to relate the location (and crystallographic orientation) of recrystallized grains to the β-particle distribution. The β-phase does not produce EBSD diffraction patterns, and so in order to relate the two phases, GOS maps (collected at 70°, the calibrated EBSD geometry) were superimposed on the SE image collected at 0°. Unfortunately, the best EBSD preparation method leads to a significant amount of relief between the β-phase and the matrix, which allows for easy identification of the β-phase in SE imaging, but also interferes with the EBSD analysis. At a 70° tilt angle, the β-particles shadow the region below them from the electron beam. Therefore, it is not possible to index the matrix adjacent to a large portion of the β-phase and it would be difficult to capture sub-micron grains that nucleated on β-particles. With a step size of 0.08 μm and a requirement that a grain contain at least ten points, only grains with a diameter larger than 0.25 μm can be detected. With these limitations in mind, Figure 3.22 represents the GOS

with relation to the bright β-phase particles. Recrystallized grains are found both adjacent to, and removed from the observable β-particles. Grains with a higher misorientation also show no specific spatial relationship to the β-phase. Based on this analysis it is not reasonable to conclude that recrystallized grains are nucleating on β-particles.

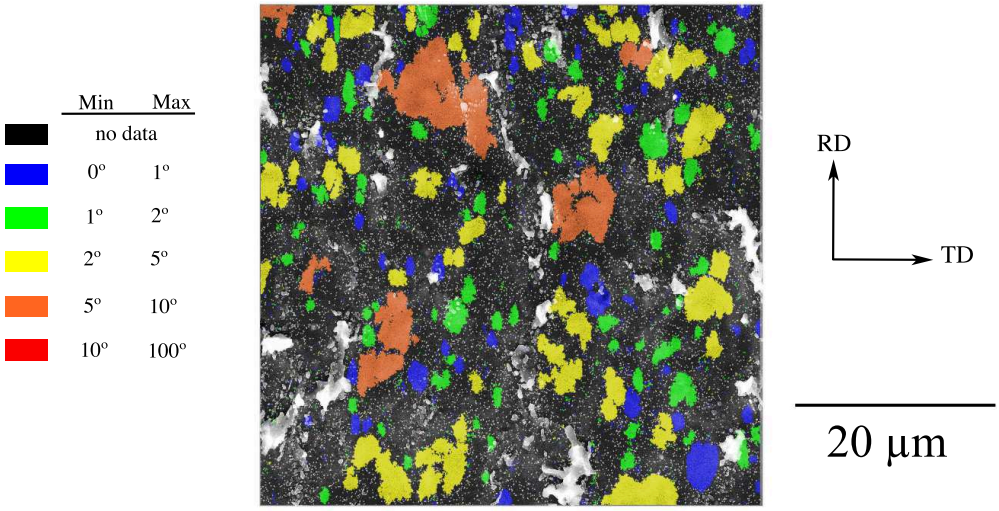

Figure 3.22: GOS map superimposed on the associated SE image in sheet annealed at 285°C for 0.5 min. The bright grey and white particles are the β-phase.

Discontinuous static recrystallization (recrystallization with distinct nucleation and growth phases) such as that observed in the TTMP AZ61 sheets, has been observed by other researchers in Mg alloys [11, 12, 25–28]. In discontinuous recrystallization, nucleation of new grains tends to occur at grain boundaries and secondary phase particles [11, 15, 25]. Continuous static recrystallization in Mg alloys has also been reported. Huang et al.. [28] made the observation that continuous recrystallization is often observed in materials that have undergone significant dynamic recrystallization while discontinuous static recrystallization is observed in materials

with little, or no dynamic recrystallization. This is consistent with our observations, as the as-rolled TTMP AZ61 sheet exhibited limited dynamic recrystallization.

3.4 Microstructure of Annealed Sheets

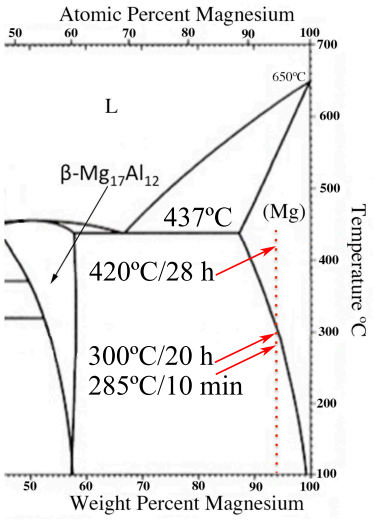

Figure 3.23: The three annealing temperatures used are indicated with red arrows on the Mg-Al phase diagram [29].

To be able to explore the effect of grain size and β-particle size and distribution on the mechanical properties, three annealing treatments were selected for the as-rolled sheet. The first is the 285°C for 10 minute annealing treatment intended to produce a nearly fully recrystallized microstructure in a relatively short time while remaining below the β-solvus. The second and third annealing treatments of 300°C for 20 hours and 420°C for 28 hours were selected to provide a materials with a reduced volume of β-phase and no β-phase respectively. The three annealing temperatures are indicated with respect to the Mg-Al phase diagram in Figure 3.23. This illustration is intended as a reference, not to imply that any of these annealing treatments result

in the equilibrium microstructure.

3.4.1 Microstructure of Sheet Annealed at 285°C for 10 minutes

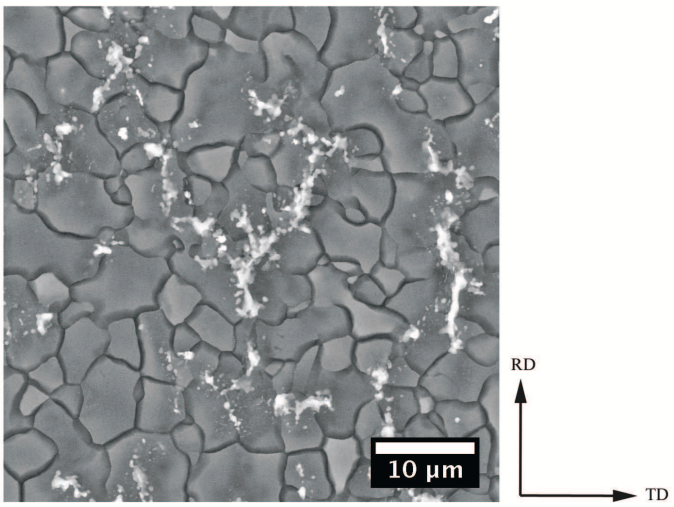

Figure 3.24: SE micrograph presenting the representative microstructure of sheet annealed for 285°C for 10 minutes.

SE images of the sheet annealed for 285°C for 10 minutes reveal equiaxed grains with an average diameter of 3.1 μm in the RD-TD plane of the sheet (Figure 3.24). IPF maps were collected from all three sheet faces (RD-TD, ND-RD, and ND-TD) to evaluate if the grains are truly equiaxed after the recrystallization anneal, or if due to the 50% reduction in thickness during sheet processing, were flattened in the normal direction. A composite of those maps is shown in Figure 3.25. Visual inspection shows that any difference between the grain size on each face is insignificant. Analysis of the grain size reveals a similar average and distribution in all three planes (Figure 3.26). The inverse pole figure maps demonstrate the basal texture of the sheet; the grains have a tendency for their c-axis to be almost parallel to the ND. As a result the IPF map in the RD-TD plane has a higher number of red, and warm tone grains.

The near alignment of the c-axis with the ND, means that the orthogonal directions $\{10\bar{1}0\}$ and $\{2\bar{1}\bar{1}0\}$ lie near the RD-TD plane and so correspondingly the IPF maps in the ND-TD and ND-RD planes are more blue-green. The texture of the annealed sheet is discussed in depth in Section 3.5.

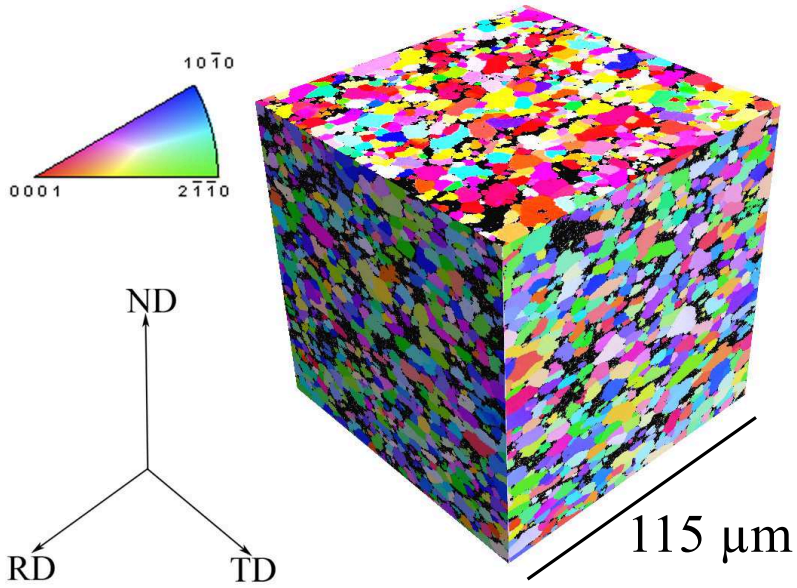

Figure 3.25: IPF maps of all three sheet faces in the sheet annealed for 285°C for 10 minutes. The Black pixels represent locations with poor EBSD pattern quality, which in this material usually indicates the location of the β-phase.

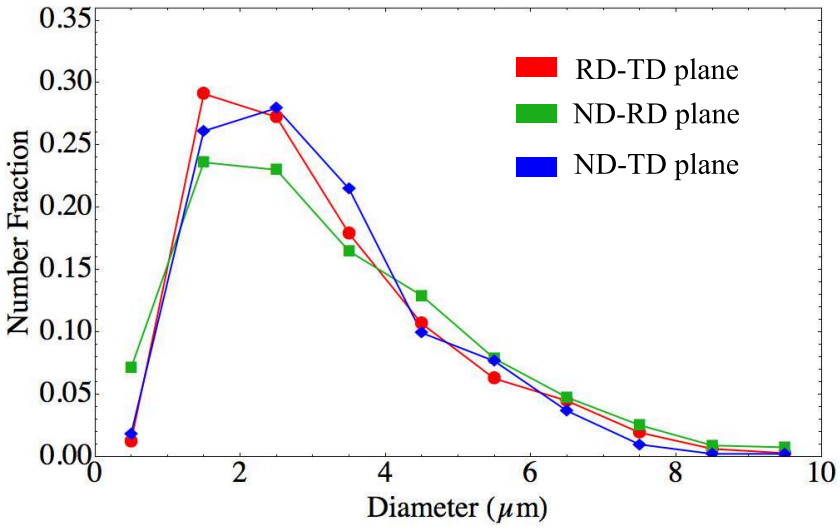

Figure 3.26: Grain size distribution of sheet annealed for 285°C for 10 minutes in all three sheet planes.

Scanning transmission electron microscopy (STEM) on the annealed sheet reveals that the fine β-precipitates are non-uniformly distributed, and tend to be clustered near the α-Mg grain boundaries (Figures 3.27 and 3.28). Phase identification in these figures is based on the similarity in particle morphology to particle composition confirmed by diffraction patterns and energy dispersive spectroscopy during TEM analysis of an earlier batch of TTMP AZ61 material. Rigorous TEM analysis of the fine β-precipitates was not conducted for this dissertation. The size and morphology of the coarser β-particles is discussed in Section 3.6.

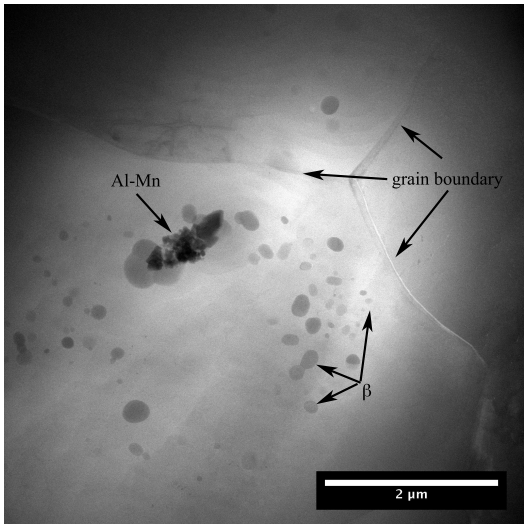

Figure 3.27: STEM of the annealed sheet showing a non-uniform distribution of β-precipitates, which tend to be clustered near grain boundaries.

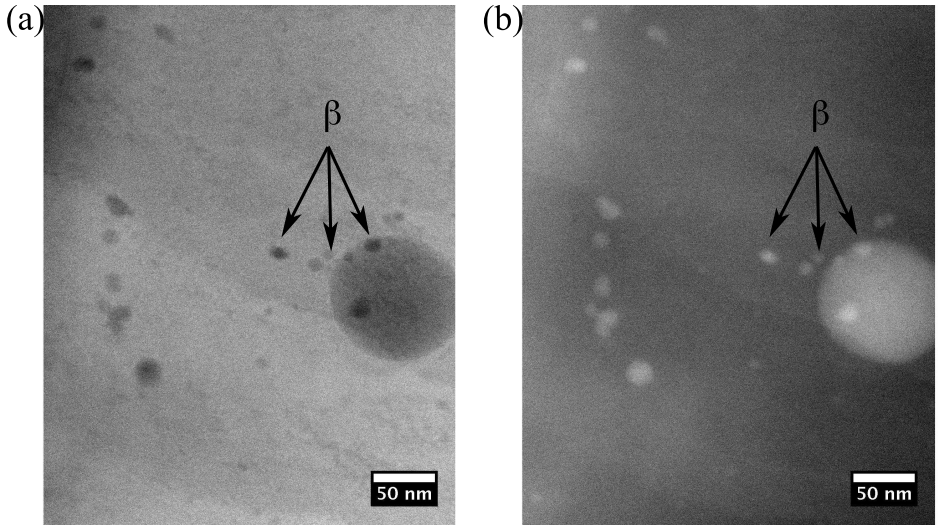

Figure 3.28: (a) Bright and (b) dark-field TEM image demonstrating a non-uniform distribution of the fine β-precipitates.

3.4.2 Microstructure of Sheet Annealed at 300°C for 20 hours

Figure 3.29 illustrates the typical microstructure after the 300°C for 20 hour annealing treatment. This treatment results in sheets with a slightly larger grain size,

and lower β-phase volume fraction than those annealed for 10 minutes at 285°C. A β-phase volume fraction of 3% indicates that equilibrium fraction of nearly 0% was not achieved. The average grain diameter is 5.6 μm.

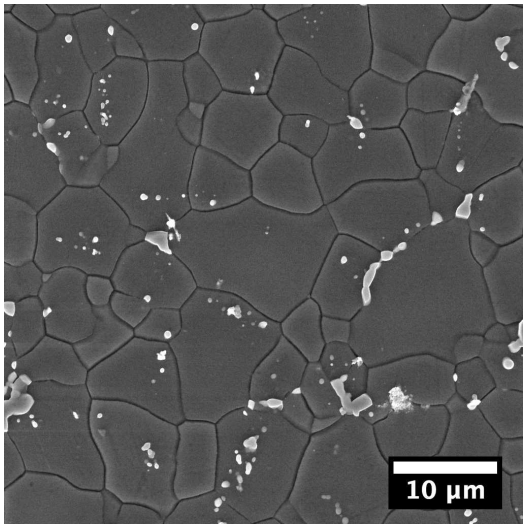

Figure 3.29: SE micrograph presenting the representative microstructure of sheet annealed for 300°C for 20 hours.

3.4.3 Microstructure of Sheet Annealed at 420°C for 28 hours

Figure 3.30(a) illustrates the typical microstructure after the 420°C for 28 hour annealing treatment. This treatment results in complete dissolution of the β-phase, as observed by SEM and also by XRD. The bright precipitates that remain are Al-Mn intermetallics based on energy dispersive spectroscopy, which dissolve at 610°C in AZ31 [30]. This annealing treatment results in the largest grain size studied in this work, 11.7 μm. Some annealing twins were observed in these sheets (Figure 3.30(b)).

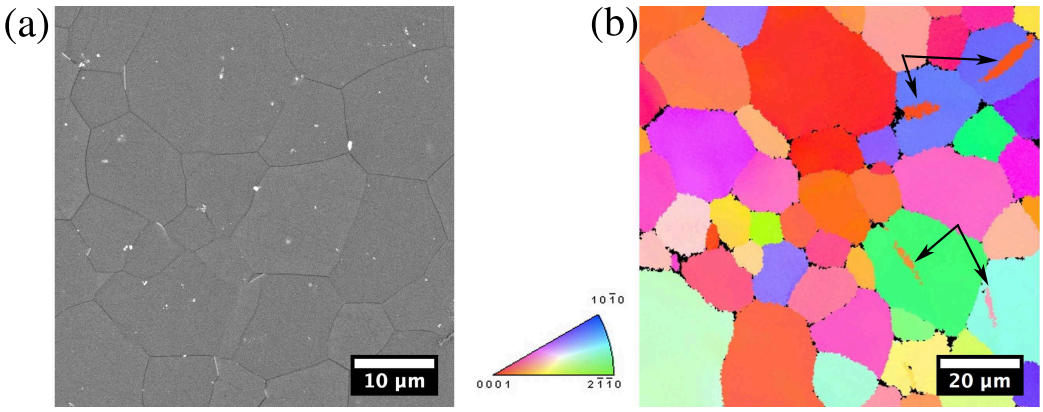

Figure 3.30: (a) SE micrograph presenting the representative microstructure of sheet annealed for 420°C for 28 hours and (b) IPF map demonstrating the presence of annealing twins.

3.4.4 Summary of Microstructure in Annealed Sheets

Table 3.2 summarizes the microstructure in the annealed sheet materials. In addition, the grain size distributions are summarized in Figure 3.31. The difference in grain size and β-phase volume fraction allows us to study the effect of these parameters on the mechanical properties, as described in Chapter IV. Unfortunately, grain size and volume fraction could not be varied independently. In addition, the basal texture intensity after each of these thermal treatments is slightly different as well, as described in the next section.

Table 3.2: Grain size and β-phase volume fraction, f_β, following the three annealing treatments.

Annealing Treatment	**Grain Diameter (μm)**	f_β(%)
285°C/10 min	3.1	5
300°C/20 h	5.6	3
420°C/28 h	11.7	0

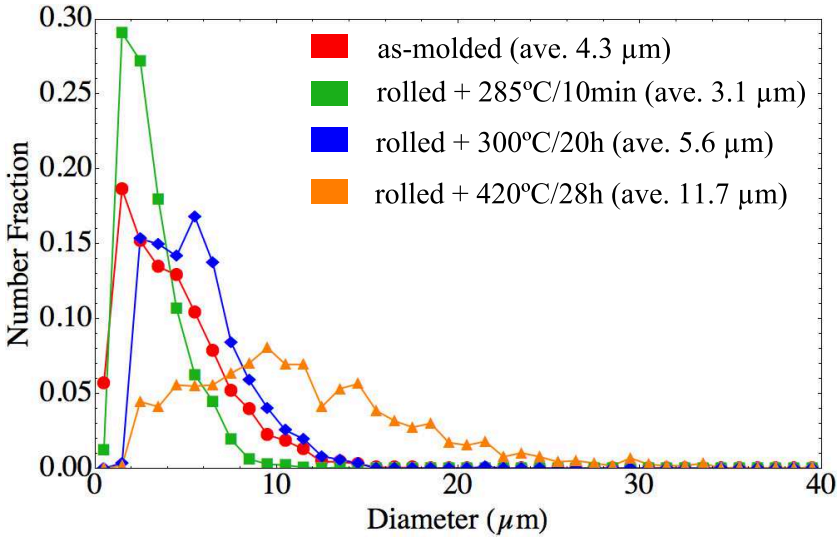

Figure 3.31: Grain size distributions for the as-molded plate and annealed sheets.

3.5 Texture Evolution During TTMP

One of the motivations for starting with Thixomolded plate as the precursor for rolled sheet, is its lack of crystallographic texture (Figure 3.3). Formability decreases as the basal texture intensity increases, so in order to produce high-formability Mg alloy sheet, a weak texture is preferred. Here we discuss the texture resulting from the single-pass warm-rolling, and then investigate how subsequent annealing treatments affect crystallographic texture.

Figure 3.32 summarizes the texture evolution in AZ61 after molding, rolling, and subsequent annealing. Rolling introduces a near basal texture with a maximum texture intensity of 4.8 MRD. The peak is split, and tilted slighting along the RD. There is a broader spread in the c-axis tilt along the TD than along the RD. In the prismatic pole figure, there is a tendency for the prismatic planes to align with the RD. The texture weakens following all three annealing treatments. After 285°C/10 min the basal texture intensity is reduced to 3.7 MRD and the orientation of $\langle \mathbf{a} \rangle$

becomes uniform around the basal fiber. The texture intensity is even lower following 300°C/20 h, at 2.4 MRD, but increases slightly, to 3.0 MRD, following 420°C/28 h.

The basal texture is typical in Mg sheet. The splitting, or elongation of the basal peak in the rolling direction is also commonly observed [31–38]. Peak splitting along the rolling direction likely results from increased activity of the $\langle \mathbf{c}+\mathbf{a} \rangle$ slip mode [39]. However, the texture of the as-rolled TTMP AZ61 sheet is distinct among AZ series alloys. Firstly, the texture intensity is relatively weak; 10 times random is typical for a basal pole figure intensity in commercial AZ31 [31, 35, 40–43]. The second notable feature is the $\langle 10\bar{1}0 \rangle$ fiber texture. Other reports on AZ series alloys that provide the $10\bar{1}0$ pole figure show a random orientation of $\langle \mathbf{a} \rangle$ and exhibit a tighter spread along the TD than along the RD in the basal pole figure [31, 35, 38, 40]. Though not usually observed in AZ series alloys, textures similar to that in as-rolled TTMP AZ61 sheet have been reported in RE containing wrought Mg sheets [32, 44]. The mechanisms behind the development of the so-called RE textures are still not understood [45].

It is not clear why the as-rolled TTMP AZ61 sheet does not develop a strong texture, though it is likely that the β-particles play some role, as the formation of the normal deformation texture can be interrupted by secondary particles [8]. Li el al conducted a study on AZ31, AZ61, and AZ91 in hot plane-strain compression, and observed that the higher levels of β-particles resulted in weaker deformation textures [46]. They proposed enhanced dynamic recrystallization via particle stimulated nucleation (PSN) as the mechanism. Miller et al.. [47], produced a weaker deformation texture by increasing the Zn concentration from 4.5 wt% to 9% to allow for the formation of Mg-Zn intermetallics in a binary Mg-Zn sheet. Along the same vein, Masoumi et al.. [48] observed a weaker texture in AZ31 sheet with a higher

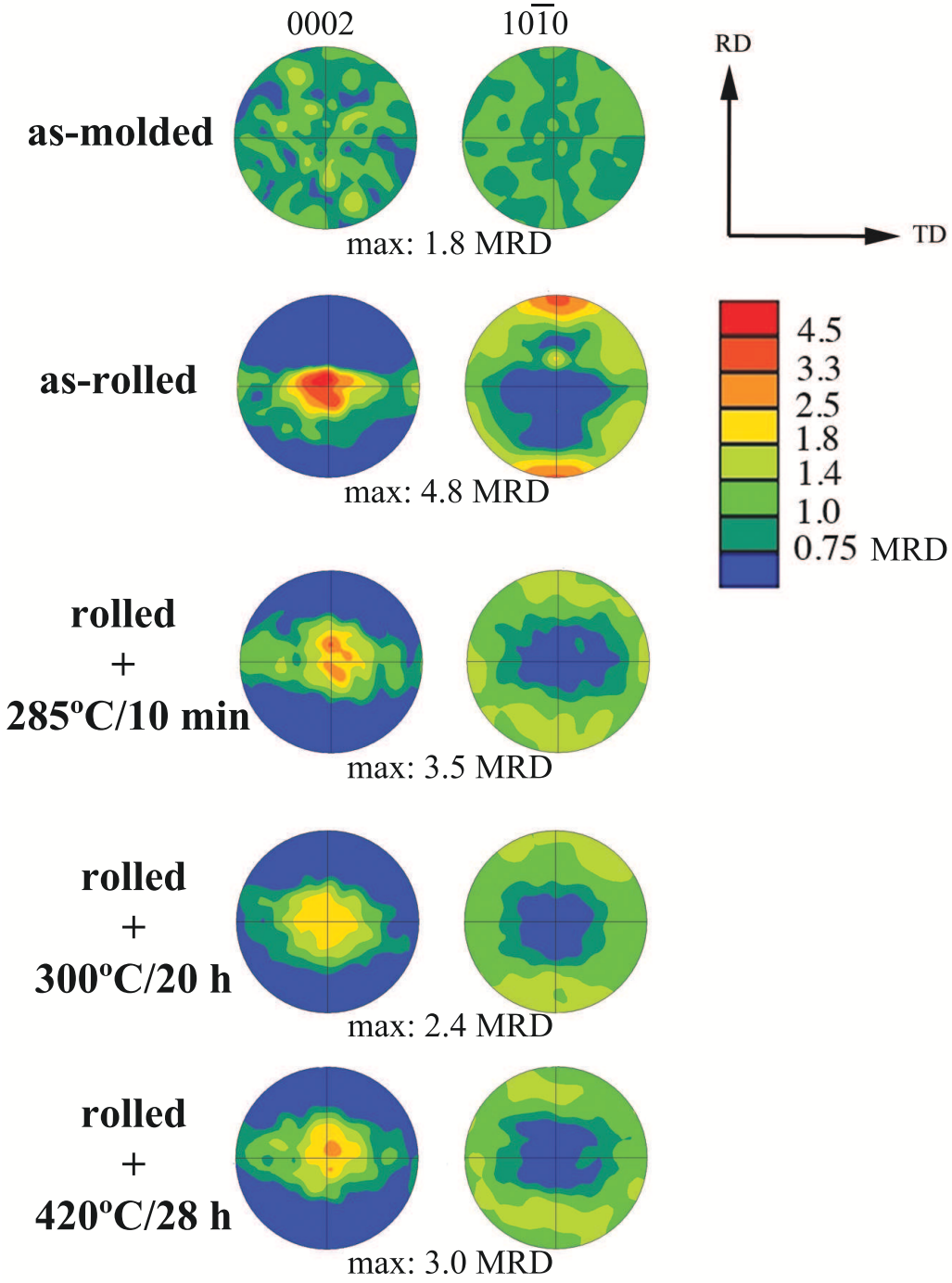

Figure 3.32: Basal and prismatic pole figures after molding, rolling, and subsequent annealing.

volume fraction (12%) of 1 μm β-particles than in sheet with a lower volume (6%) of 3 μm particles. It is interesting, that in both Miller and Masoumi's work, the particle containing materials exhibit textures with spread along the TD, similar to the RE-texture. However, a higher β-phase content does not guarantee a weak deformation texture or TD spreading; Kim et al.. [49] produced AZ91 sheet by differential speed hot rolling with a 65% reduction in thickness after a single pass, this sheet exhibited a strong basal texture with a maximum intensity of 16.3 MRD.

PSN is not necessary for the development of the RE texture; dilute alloys with RE elements in solution can exhibit weak textures as well [50–52]. It has been proposed that solute drag alters the recrystallization mechanisms responsible for the conventional basal texture by suppressing the mobility of the high angle grain boundaries [50–52]. We observed precipitates pinning grain boundaries during recrystallization in as-rolled TTMP AZ61, so perhaps Zener pinning, rather than PSN, is the mechanism from which the weak RE-like texture arises. Hadorn et al.. [52] reached a similar conclusion while investigating weak textures in a Nd containing Mg alloys with second-phase particles. In their study, alloys with secondary-phase particles large enough to enable Zener pinning developed weaker deformation textures, even if the particles were smaller than required for PSN. Zener pinning in TTMP AZ61 will be addressed in Section 3.7.

An interesting observation in the as-rolled sheet is that the few externally solidified grains studied by EBSD exhibited a basal texture. One such grain, and its associated IPF map is shown in Figure 3.33. These grains do not contain precipitates, and so they provide anecdotal evidence that in the absence of β-particles, a strong, basal texture would result from rolling. However, even if the orientation of a significant number of these grains had been studied, differences in the deformation mechanisms

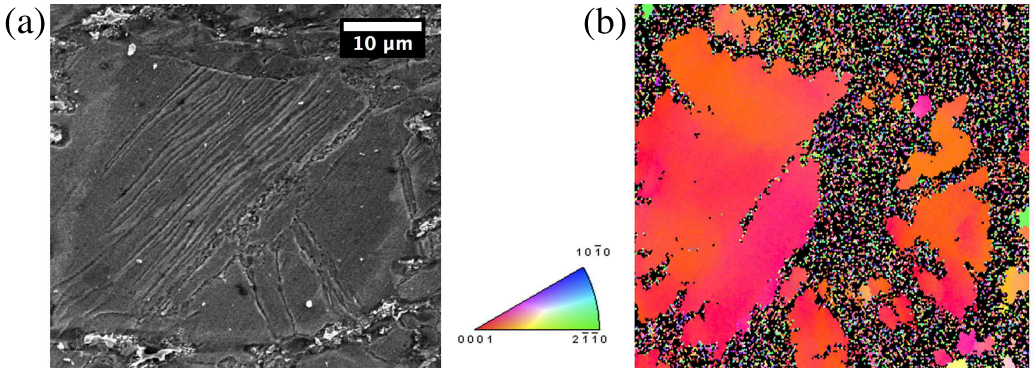

Figure 3.33: (a) SE micrograph of an externally solidified grain in the as-rolled sheet and (b) the associated IPF map.

due to significantly larger grain size must be considered.

The already weak basal texture is further reduced during static annealing with the texture intensity reduced 20% following the 285°C/10 min anneal and 50% following the 300°C/20 h anneal. However, texture generally does not change during static annealing [8, 53–57]. Masoumi et al.. [48] have shown texture reduction during the annealing of twin-roll cast AZ31, which they attributed to PSN arising from a higher volume fraction of secondary phases. This mechanism may be active in the TTMP AZ61L sheet as well. The reduction in texture observed after annealing of the TTMP sheet is consistent with a reduction from 5.4 to 3.1 MRD produced by a computer model of PSN [58]. Another postulate is that discontinuous static recrystallization allows for texture randomization [28]. Recrystallization occurring via lattice rotations at grain boundaries can lead to a change in recrystallization texture [8]. Discontinuous static recrystallization is the dominant recrystallization mechanism in the TTMP AZ61L as pinning of grain boundaries and dislocations by β-particles (as observed in Figure 3.20) likely hinders dynamic recrystallization as well. Similar observations have been made during recrystallization of RE alloys [51, 59]. As will be shown in Chapter IV, the texture of the TTMP AZ61 sheet has

important effects on mechanical behavior.

3.6 Evolution of β-phase through TTMP

TTMP involves both thermal exposures and mechanical deformation that may affect the size, morphology, and distribution of the secondary phase particles. Here we focus on characterizing the β-phase after four processing stages; molding, preheating, rolling, and the 10 minute at 285°C annealing treatment.

Figure 3.34 illustrates (a) the volume fraction and distribution of the β-particles and (b) the particle size and morphology. The rapid cooling rate during Thixomolding leads to a supersaturation of aluminum; an average volume fraction of β-phase of only 4.2% is determined by area fraction measurements. AZ61 has a maximum equilibrium β-phase volume fraction of 10.3%. Segregation of Al to the grain boundary regions due to the solidification path leads to the variation in shading in the α-phase highlighted in Figure 3.34(b). The β-particles are distributed primarily along grain boundaries, and have an average diameter of 0.5 μm.

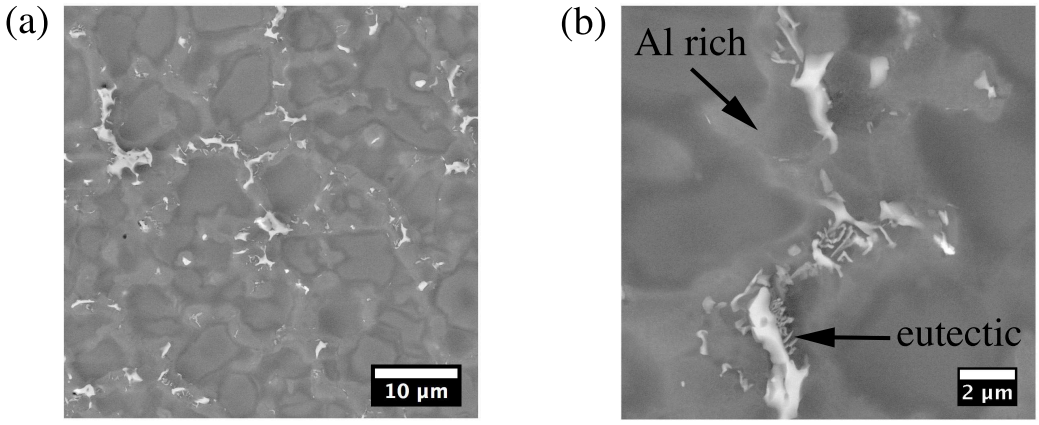

Figure 3.34: The volume fraction and distribution of the β-particles (a) and the particle size and morphology (b) in the as-molded plate.

Before rolling, the plates are preheated to 315°C for 5 minutes. Preheating does not affect the spatial arrangement of the β-phase particles (Figure 3.35(a)) but leads to an increase in the number of fine particles and thus an increase in the β-phase volume fraction to 5.5% (Figure 3.35(b)). As illustrated in Figure 3.36, the new particles have a platelet or lath shape, and a thickness of less than 50 nm. These platelets, appear rod-like when viewed on edge. Based on the decreased variation of shading in the α-phase, the Al concentration is likely more uniform after the preheat.

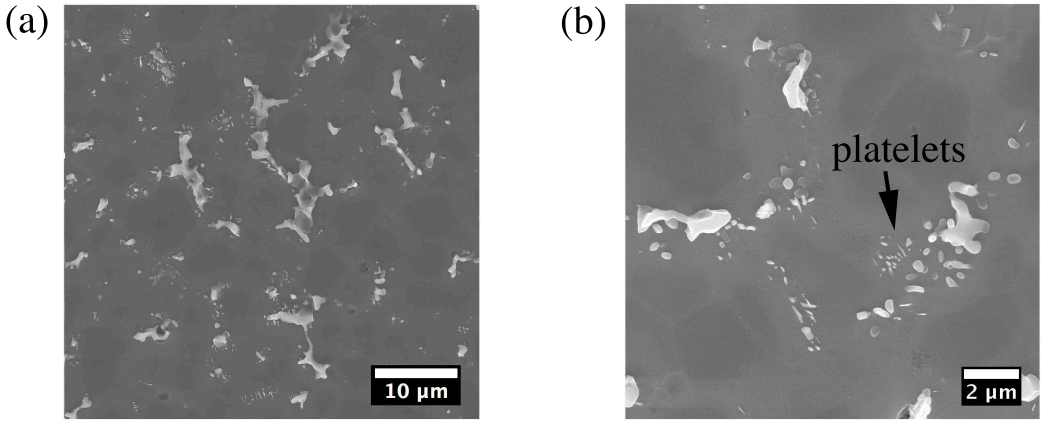

Figure 3.35: The volume fraction and distribution of the β-particles (a) and the particle size and morphology (b) in the plate following a 315°C for 5 minutes thermal exposure.

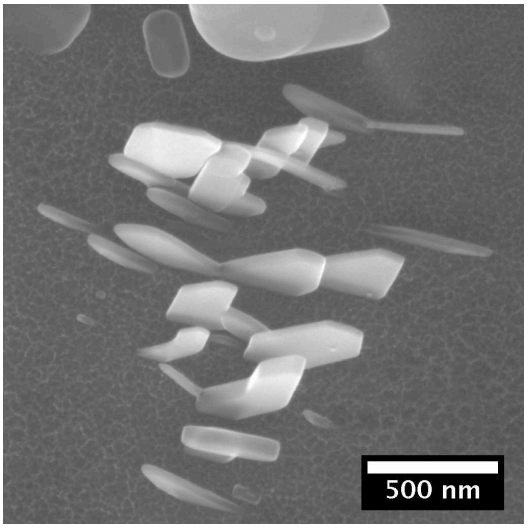

Figure 3.36: β-phase platelets in the molded plate following a 315°C for 5 minutes thermal exposure.

Rolling leads to a slight elongation of the β-particle network along the RD (Figure 3.37(a)). The β-phase volume fraction further increases to 7.6%. Once again, this increase results from an increase in fine β-particles (Figure 3.37(b)). No evidence of brittle fracture of the β-particles as a result of rolling was observed. A close examination of the largest β-particles in the as-rolled material reveal that at least superficially, they are conglomerates of small spherical particles (Figure 3.38).

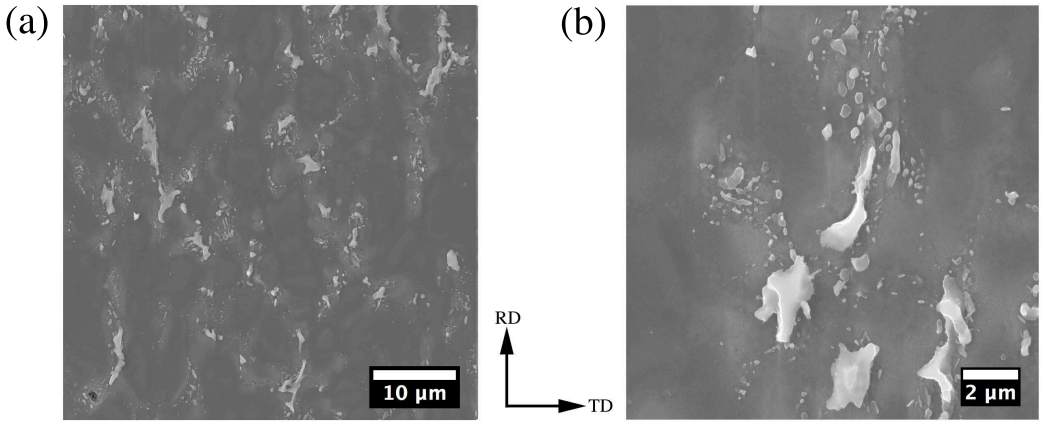

Figure 3.37: The volume fraction and distribution of the β-particles (a) and the particle size and morphology (b) in the as-rolled sheet.

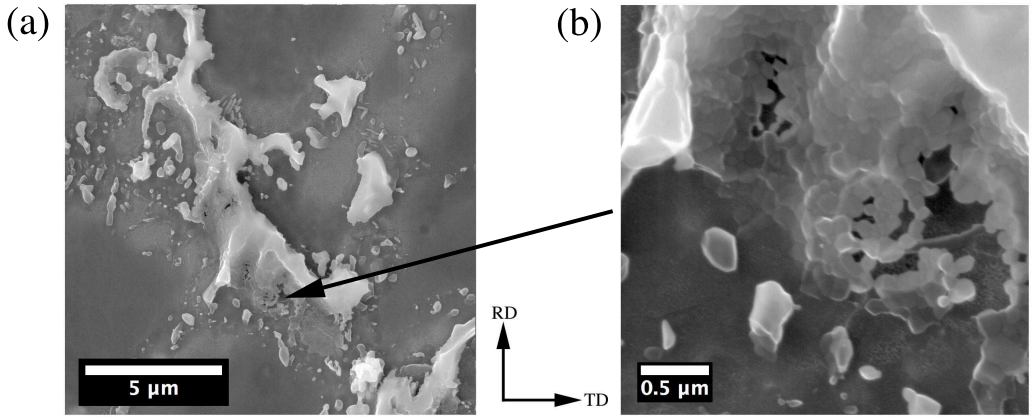

Figure 3.38: The surfaces of the large β-particles in the as-rolled sheet are coated with a conglomerate of many smaller particles, as shown in higher magnification on the right.

Annealing at 285°C/10 min led to some dissolution of the β-phase. Figure 3.39 highlights a reduction in in the β-phase volume fraction to 4.8%. The β-particles become less angular. Strands of β-particles still tend to be aligned with the rolling direction, but are now spaced further apart due to the dissolution. Some of the β-platelets persist.

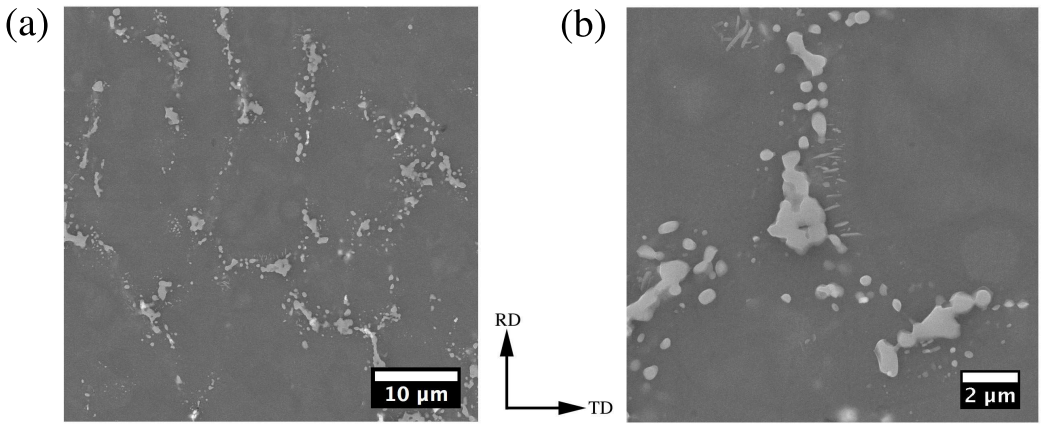

Figure 3.39: The volume fraction and distribution of the β-particles (a) and the particle size and morphology (b) in sheet annealed for 285°C for 10 min.

Comparison of Figures 3.34(a), 3.35(a), 3.37(a), and 3.39(a) show that, aside from a slight elongation after rolling, the spatial distribution of β-particles remains fairly constant during TTMP. The particle size distribution also does not show much variation during processing (Figure 3.40). Precipitation of the β-phase during rolling results in the as-rolled sheet having the largest fraction of fine β-particles (Figure 3.40(a)). If we focus on particles larger than 0.5 μm in diameter (Figure 3.40(b)), we can observe variations in the fraction of smaller β-precipitates as they precipitate and grow during the preheating and then again during rolling, and decrease slightly during dissolution. Another way to track the precipitation and growth during processing is to look at the number density of particles after each step.

Figure 3.41 chronicles this evolution of the number density for two different particle sizes, those with an average diameter between 0.2 and 0.5 μm, and those larger than 0.5 μm which can play significant roll in PSN and Zener pinning. It is clear that the preheating step does not affect the number of large particles, but results in the precipitation of new, fine particles. Rolling results in significant β-phase pre-

cipitation. It also appears that the number of large particles increases after rolling as well, but this could be the result an increase in the area in the RD-TD plane to conserve volume as the β-particles are flattened during rolling (recall that the rolling process results in a 50% reduction in the sheet thickness). Another possibility, supported by the morphology of the large β-particle in Figure 3.38, is that particles can agglomerate during deformation, leading to the formation of some larger particles. Dissolution during the post-rolling thermal treatment results in a decrease in the number of fine β-particles. The number of large particles is not affected. The similarity between the particle size distribution between the as-molded and as-rolled conditions indicates that rolling does not break-up the larger β-particles. However, it does change their shape slightly.

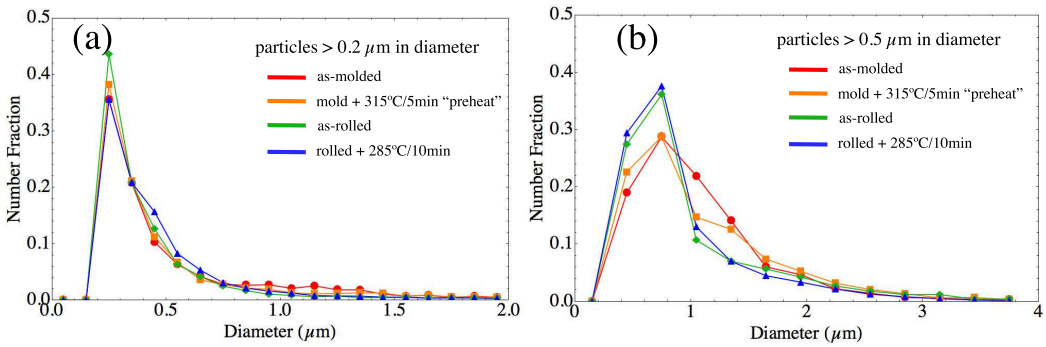

Figure 3.40: Evolution of the β-particle size distribution during TTMP for (a) particles greater than 0.2 μm in diameter and (b) particles greater than 0.5 μm in diameter.

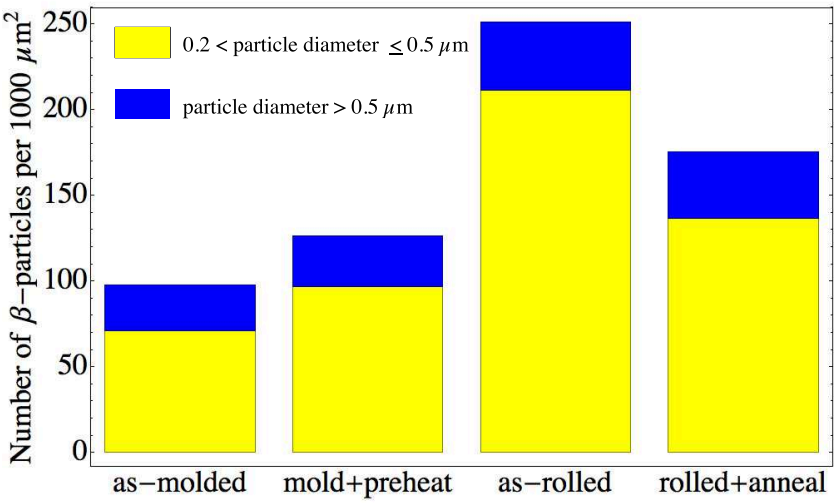

Figure 3.41: The number density of β-particles at different stages of TTMP.

To determine the extent of the elongation of β-particles along the RD, a bounding box can be constructed around each particle. Figure 3.42 illustrates some of these boxes around particles in the sheet annealed for 285°C for 10 min. The elongation can be quantified by taking the ratio of the bounding box length along the RD to that along the TD. These bounding box measurements were done automatically as an option of the ImageJ "Analyze Particle" routine when doing the particle size analysis as described in 2.2.3. Log normal fits of the ratio for particles larger than 0.5 μm^2 in size are summarized in Figure 3.43. The plate materials have approximately the same mean and mode, at 1.1 and 0.8, respectively. The as-rolled material has the largest extent of elongation along the RD; the distribution of the bounding box ratio in this material has a mode of 1.1 and a mean of 1.5. As the particles are slightly reduced in size following the post-rolling anneal, the ratio decreases slightly but remains higher than in the undeformed plates.

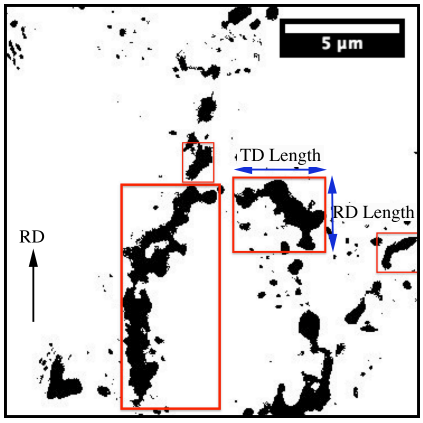

Figure 3.42: Illustration of the bounding box technique to define particle length in the RD and TD directions. In this threshold adjusted micrograph of β-particles in the sheet annealed for 285°C for 10 min, red boxes, which bound the particle in both the RD and TD direction have been added. A rough approximation for the maximum particle length in either direction can be made by assuming the particle can be described by the dimensions of this box.

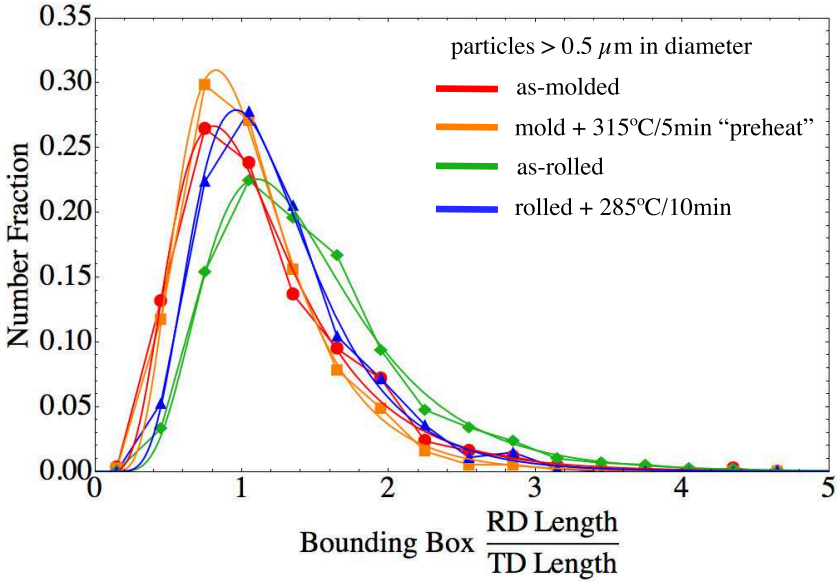

Figure 3.43: Evolution during TTMP of the aspect ratio of of particles larger than 0.5 μm^2 as described by a bounding box.

3.7 Grain Size Stability

Grain size stability is an important consideration as Mg sheet may require elevated temperatures in order to successful form complex parts. Grain growth during forming at elevated temperatures will result in a loss of strength via the Hall-Petch effect. The 420°C for 28 hour solution treatment resulted in a grain size (11.7 μm) twice that observed after 20 hr at 300°C (5.6 μm). This difference may be a result of faster grain growth kinetics at the higher temperature. A portion of the difference may also be a result of the dissolution of the β-particles which could have been pinning grain boundaries during the 300°C for 20 hour treatment. To develop a better understanding of the thermal stability, we conducted a 20h treatment at 285°C to see whether the desirable 3.1 μm grain size that resulted from the 10 min treatment at the same temperature is stable, perhaps as a consequence of the β-particles.

Figure 3.44 shows the grain size after (a) 10 min and (b) 20 hours at 285°C. The grain size increased from an average of 3.1 μm to 4.8 μm after the extended annealing treatment. The grain size distribution (Figure 3.44(c)) for the longer annealing treatment is also broader, indicating that not all grains grow at an equal rate. The two annealing treatments result in the same texture (Figure 3.44(a and b)). The longer annealing treatment results in a larger grain size, a fully recrystallized microstructure, and dissolution of the smaller β-phase particles, which improves the EBSD image quality, reducing the number of black pixels in the IPF maps. Examination of the microstructure after the 20 hour annealing treatment at 285°C (Figure 3.45(a)) reveals that the larger particles (a few of which are highlighted by black arrows) reside on grain boundaries. Dividing the particles in this image into two groups, those that are found on grain boundaries, and those that are not, we

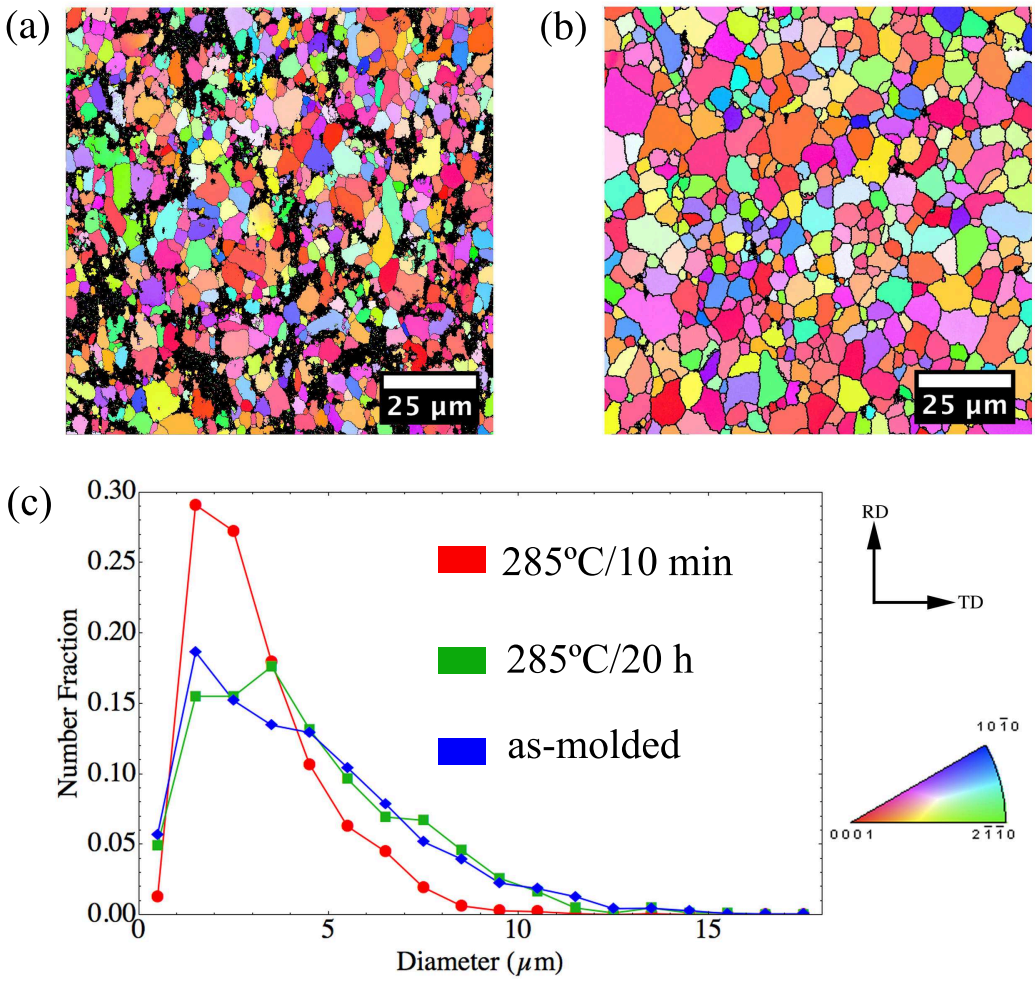

Figure 3.44: IPF maps illustrating the grain size after (a) 10 min and (b) 20 hours at 285°C and (c) their associated grain size distributions compared to that of the as-molded plate.

can evaluate the likelihood that these particles are providing grain size stability. The results of this analysis are shown in Figure 3.45(b). The fact that smaller particles are less likely to be associated with the grain boundaries than the larger particles is clear evidence of Zener pinning. The minimum particle diameter effective in pinning the grain boundaries in the TTMP AZ61 sheet after 20h at 285°C $\sim$ 0.5 μm.

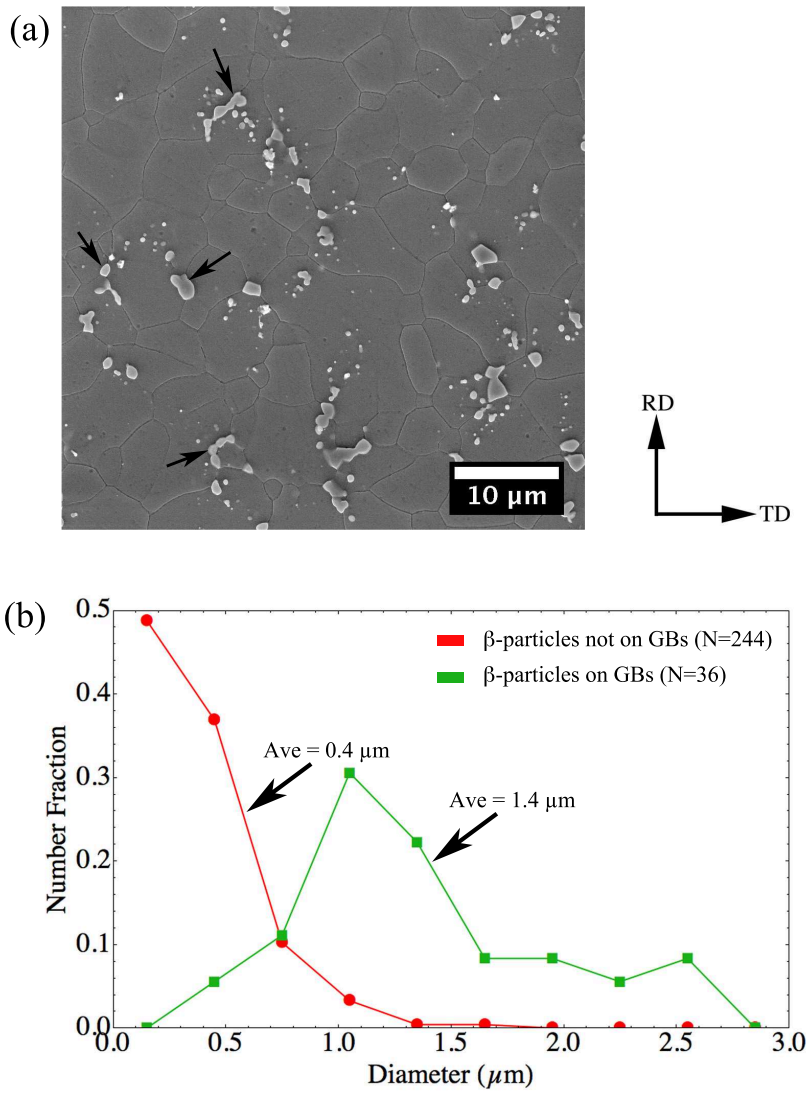

Figure 3.45: (a) SE image highlighting particles residing on grain boundaries and (b) a comparison of the size distribution of particles that are and are not associated with grain boundaries.

Whether Zener drag is effective at restricting grain growth depends on the size and number of the particles. The Zener drag pressure exerted by a uniform distribution of spherical particles, with a radius of r, on the grain boundary is given by Eqn. 3.4, where f_β is the particle volume fraction and γ is the grain boundary energy [8, 52, 60]. The pressure for grain growth is given by Eqn. 3.5, where D is the grain diameter and α is a geometric factor [8, 52, 60]. Classically, a value of 2 is used for the geometric constant, α, though further studies have suggested values between 0.5 and 1 when considering grain and particle size distributions, non-uniform distribution of particles, and several other geometric factors [52, 60]. The critical grain diameter above which Zener pinning will occur, D_c, as given in Eqn. 3.6, is determined by setting P_Z=P_G and solving for D [8].

$$P_Z = \frac{3 f_\beta \gamma}{2r} \tag{3.4}$$

$$P_G = \frac{\alpha \gamma}{D} \tag{3.5}$$

$$D_c = \frac{2r\alpha}{3 f_\beta} \tag{3.6}$$

Following the 285°C for 10 minute treatment, the average particle diameter is 0.34 μm and f_β is 4.8%. Using these parameters in Eqn. 3.6 with the classical value of α=2, the Zener pinning limiting grain size is 4.7 μm. If α is reduced to 0.5, then the critical grain size is only 1.2 μm. As the distribution of β-particles is so non-uniform, the larger size seems more reasonable (though it was based on the assumption of homogeneously distributed particles). Though the assumptions used to arrive at D_c oversimplify the TTMP microstructure, the range in predicted grain size overlaps with the experimentally determined grain size in TTMP sheets annealed at 285°C (3.1 to 4.8 μm).

Based on this analysis and observation of the microstructure, it is clear that the β-particles provide for grain size stability in the TTMP AZ61 sheet. The similarity between the grain size distribution after 20 hr at 285°C to that in the as-molded plates in Figure 3.44(c) is not a coincidence. As the size and distribution of larger β-particles is only slightly altered by rolling, β-particles will pin the grain boundaries in a similar interval as to how they decorated the boundaries in the as-molded material. The as-molded grain size acts to predetermine the stable grain size if a majority of the β-phase is maintained. Annealing treatments that result in a reduction of the β-phase volume fraction, such as the 300°C for 20 h treatment result in a larger grain size. This gives the AZ61 sheet some benefit over the commonly used AZ31 which has only 3% Al. The grain size stability in TTMP AZ61 could be improved by producing a higher quantity of fine, uniformly distributed precipitates.

At 420°C for 28 h, above the β-solvus, we begin to see the excessive growth of a few grains. This is typically referred to as abnormal grain growth [8]. Optical micrographs of sheet annealed for 300°C for 20 h (Figure 3.46(a)) demonstrate a fairly uniform microstructure. On the other hand, the sheet annealed for 420°C for 28 h (Figure 3.46(b)) contains some grains that are an order of magnitude larger than the average grain size. The size of these large grains is consistent with their being the remnants of some of the externally solidified grains in the as-molded microstructure. Abnormal grain growth can be a result of a non-uniform distribution of secondary phase particles or the result of texture [8]. The externally solidified grains are free of β-particles. Without the presence of particles to pin grain boundaries, the growth of recrystallized grains inside the volume of the prior externally solidified grain is unrestricted until they impinge upon β-particles at the perimeter of the prior externally solidified grain.

In textured materials, certain grain boundaries may have higher mobilities, and thus grains with specific orientations grow at the expense of the other grains [8]. Abnormal grain growth at annealing temperatures above 350°C has been reported by several authors in Mg sheet, and has been associated with an increase in the basal texture [11, 51, 61, 62]. Indeed, the 420°C for 28 h sheet has a stronger texture than the 300°C for 20 h sheet. The texture of the abnormal grains was not evaluated in this study.

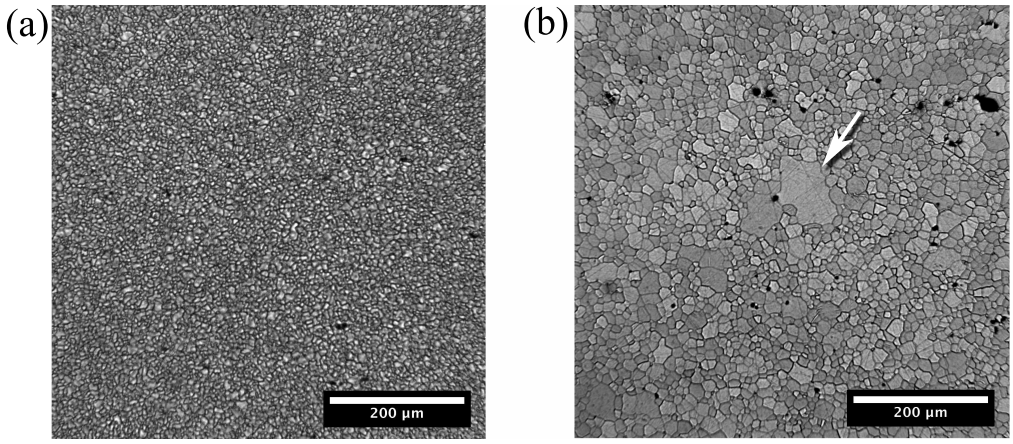

Figure 3.46: Optical micrographs of (a) sheet annealed for 300°C for 20 h and (b) sheet annealed for 420°C for 28 h demonstrating abnormal grain growth following the higher temperature anneal.

3.8 Summary

Starting with a Thixomolded plate, which exhibits a fine α-Mg grain size, a distribution of relatively fine β-precipitates, low porosity, and no crystallographic texture, we succeeding in producing sheet 1.8 mm in thickness with a texture much weaker than that observed in conventional AZ31 sheet. This weak texture may arise as Zener pinning of high angle grain boundaries by β-particles prevents the development of the typical Mg sheet deformation texture. It was shown that discontinuous static re-

crystallization following a 285°C/10 minute annealing treatment results in an average grain size of 3.1 μm and a further decrease in texture. Additional annealing treatments at 300°C for 20 h and 420°C for 28 h, resulted in average grain sizes of 5.6 and 11.7 μm respectively, and also a reduction in the β-phase volume fraction. Variations in the grain size, β-phase volume fraction, and texture in the TTMP achieved by annealing provide for the evaluation of the influence of these variables on tensile deformation behavior as is discussed in Chapter IV. In addition to promoting a weaker deformation texture, the β-particles also pin boundaries during thermal exposure, providing for grain size stability which is desirable for warm-forming applications. It is found that the spatial distribution of the β-particles is relatively stable during processing, so modifications to optimize the texture reduction or grain size stability would likely need to be made by varying the Thixomolding parameters or pre-rolling heat treatment.

Bibliography

1. L.-J. Yang, Y.-H. Wei, and L.-F. Hou, *Journal of Materials Science*, 45 (13) (2010), 3626–3634.
2. F. Czerwinski, *Materials Science and Engineering: A*, 392 (1-2) (2005), 51–61.
3. T. K. Nandy, R. M. Messing, J. W. Jones, T. M. Pollock, D. M. Walukas, and R. F. Decker, *Metallurgical and Materials Transactions A*, 37 (December) (2006), 3725–3736.
4. F. Czerwinski, a. Zielinska-Lipiec, P. Pinet, and J. Overbeeke, *Acta Materialia*, 49 (7) (2001), 1225–1235.
5. J. F. Nie, *Metallurgical and Materials Transactions A*, 43 (11) (2012), 3891–3939.
6. A. Beer and M. Barnett, *Scripta Materialia*, 61 (12) (2009), 1097–1100.
7. P. Hodgson and R. Gibbs, *ISIJ International*, 32 (12) (1992), 329–338.
8. F. Humphreys and M. Hatherly, *Recrystallization and Related Annealing Phenomena* (Elsevier, Netherlands, 2004), 2 ed.
9. A. Yanagida and J. Yanagimoto, *Materials Science and Engineering: A*, 487 (1-2) (2008), 510–517.
10. R. A. P. Djaic and J. J. Jonas, *Metallurgical Transactions*, 4 (2) (1973), 621–624.
11. H. Chao, H. Sun, W. Chen, and E. Wang, *Materials Characterization*, 62 (3) (2011), 312–320.
12. S. Wang, S. B. Kang, and J. Cho, *Journal of Materials Science*, 44 (20) (2009), 5475–5484.
13. X. Yang, Y. Okabe, H. Miura, and T. Sakai, *Materials and Design*, 36 (2012), 626–632.
14. A. Beer and M. Barnett, *Materials Science and Engineering A*, 485 (2008), 318–324.
15. C. Su, L. Lu, and M. Lai, *Philosophical Magazine*, 88 (2) (2008), 181–200.
16. M. C. Weinberg, I. Birnie, D. P, and V. Shneidman, *Journal of Non-Crystalline Solids*, 219 (1997), 89–99.
17. T. D. Berman, W. Donlon, V. M. Miller, R. F. Decker, J. Huang, T. M. Pollock, and J. Jones, *Magnesium Technology*, eds. S. Mathaudhu, W. Sillekens, N. Hort, and N. Neelameggham (Wiley, 2012), 339–344.
18. J. Cahn, *Acta Metallurgica*, 4 (12) (1956), 449–459.
19. S. Housh, B. Mikucki, and A. Stevenson, *ASM Specialty Handbook: Properties of Magnesium Alloys.* (ASM International, Metals Park, Ohio, 1990).

20. M. Avedesian and H. Baker, *ASM Specialty Handbook: Magnesium and Magnesium Alloys* (ASM International, Metals Park, Ohio, 1999).

21. Y. He, Q. Pan, Y. Qin, X. Liu, W. Li, Y. Chiu, and J. J. Chen, *Journal of Alloys and Compounds*, 492 (1-2) (2010), 605–610.

22. J.-H. Park, T.-H. Ahn, H.-S. Choi, J.-M. Chung, D.-I. Kim, K. H. Oh, and H. N. Han, *Microscopy and microanalysis*, 19, S5 (2013), 21–4.

23. S. Dziaszyk, E. Payton, F. Friedel, V. Marx, and G. Eggeler, *Materials Science and Engineering: A*, 527 (29-30) (2010), 7854–7864.

24. A.-L. Helbert, W. Wang, T. Baudin, and R. Penelle, *Advanced Engineering Materials*, 14 (1) (2012), 39–44.

25. X. Huang, K. Suzuki, and Y. Chino, *Journal of Alloys and Compounds*, 509 (14) (2011), 4854–4860.

26. X. Huang, K. Suzuki, and Y. Chino, *Materials Science & Engineering A*, 538 (2012), 281–287.

27. L. W. F. Mackenzie, G. W. Lorimer, F. Humphreys, and T. Wilks, *Materials Science Forum*, 469-470 (2004), 477–482.

28. X. Huang, K. Suzuki, Y. Chino, and M. Mabuchi, *Journal of Materials Science* (2012), 4561–4567.

29. A. Nayeb-Hashemi, *Phase Diagrams of Binary Magnesium Alloys* (ASM International, Metals Park, Ohio, 1988).

30. W. Kim and B. Lee, *Journal of Alloys and Compounds*, 482 (1-2) (2009), 106–109.

31. S. Agnew and O. Duygulu, *International Journal of Plasticity*, 21 (6) (2005), 1161–1193.

32. J. Bohlen, M. R. Nurnberg, J. W. Senn, D. Letzig, and S. Agnew, *Acta Materialia*, 55 (2007), 2101–2112.

33. Y. Chino and M. Mabuchi, *Scripta Materialia*, 60 (6) (2009), 447–450.

34. X. Huang, K. Suzuki, Y. Chino, and M. Mabuchi, *Journal of Alloys and Compounds*, 509 (28) (2011), 7579–7584.

35. S. Yi, J. Bohlen, F. Heinemann, and D. Letzig, *Acta Materialia*, 58 (2) (2010), 592–605.

36. H. Zhang, G. Huang, D. Kong, G. Sang, and B. Song, *Journal of Materials Processing Technology*, 211 (10) (2011), 1575–1580.

37. L. Jin, J. Dong, R. Wang, and L. Peng, *Materials Science and Engineering: A*, 527 (7-8) (2010), 1970–1974.

38. J. Koike, *Metallurgical and Materials Transactions A*, 36 (7) (2005), 1689–1696.

39. S. Agnew, M. Yoo, and C. Tomé, *Acta Materialia*, 49 (20) (2001), 4277–4289.

40. A. Jain, O. Duygulu, D. Brown, C. Tomé, and S. Agnew, *Materials Science and Engineering: A*, 486 (1-2) (2008), 545–555.

41. Y. Chino, K. Sassa, and M. Mabuchi, *Journal of Materials Science*, 44 (7) (2009), 1821–1827.

42. M. Eddahbi, J. del Valle, M. Pérez-Prado, and O. Ruano, *Materials Science and Engineering: A*, 410-411 (2005), 308–311.

43. H. Wang, B. Raeisinia, P. Wu, S. Agnew, and C. Tomé, *International Journal of Solids and Structures*, 47 (21) (2010), 2905–2917.

44. D. Wu, R. Chen, and E. Han, *Journal of Alloys and Compounds*, 509 (6) (2011), 2856–2863.

45. S. Agnew and J. Nie, *Scripta Materialia*, 63 (7) (2010), 671–673.

46. X. Li, F. Jiao, T. Al-Samman, and S. G. Chowdhury, *Scripta Materialia*, 66 (2012), 159–162.

47. V. Miller, J. Nie, and T. Pollock, "Recrystallization Behavior of Binary Mg-Zn Alloys," Oral Presentation in the Magnesium Technology Session at TMS. San Diego, CA. (2014).

48. M. Masoumi, F. Zarandi, and M. Pekguleryuz, *Scripta Materialia*, 62 (11) (2010), 823–826.

49. W. Kim, J. Park, and W. Kim, *Journal of Alloys and Compounds*, 460 (1-2) (2008), 289–293.

50. J. W. Senn and S. Agnew, *Magnesium Technology*, eds. M. Pekguleryuz, N. Neeglameggham, R. Beals, and E. Nyberg (Wiley, 2008), 153–158.

51. J. P. Hadorn, K. Hantzsche, S. Yi, J. Bohlen, D. Letzig, J. A. Wollmershauser, and S. Agnew, *Metallurgical and Materials Transactions A*, 43 (April) (2012), 1347–1362.

52. J. P. Hadorn, K. Hantzsche, S. Yi, J. Bohlen, D. Letzig, and S. Agnew, *Metallurgical and Materials Transactions A*, 43 (April) (2012), 1363–1375.

53. S. Agnew, J. Horton, T. Lillo, and D. Brown, *Scripta Materialia*, 50 (3) (2004), 377–381.

54. A. Jager, P. Lukáč, V. Gartnerova, J. Haloda, and M. Dopita, *Materials Science and Engineering: A*, 432 (1-2) (2006), 20–25.

55. L. W. F. Mackenzie and M. Pekguleryuz, *Scripta Materialia*, 59 (6) (2008), 665–668.

56. R. K. Nadella, I. Samajdar, and G. Gottstein, *Magnesium: Proceedings of the 6th International Conference Magnesium Alloys and Their Applications*, ed. K. Kainer (Wiley, 2005), 1052–1057.

57. G. Gottstein and T. Al-Samman, *Material Science Forum*, 495-497 (2005), 623–632.

58. F. Habiby and F. Humphreys, *Textures and Microstructures*, 20 (1977) (1993), 125–140.

59. K. Hantzsche, J. Bohlen, J. Wendt, K. Kainer, S. Yi, and D. Letzig, *Scripta Materialia*, 63 (7) (2010), 725–730.

60. P. Manohar, M. Ferry, and T. Chandra, *ISIJ International*, 38 (1998) (1998), 913–924.

61. M. Pérez-Prado and O. Ruano, *Scripta Materialia*, 48 (1) (2003), 59–64.

62. W. Peng, P.-J. Li, and P. Zeng, *Trans Nonferrous Met Soc China*, 16 (September) (2006), 1716–1720.

CHAPTER IV

Deformation Behavior

The deformation behavior of TTMP AZ61 was studied by room temperature uniaxial tensile tests. From these results, the dependence of strength and ductility on the grain size and texture is explored. The r-value and strain hardening coefficient are calculated and used to predict the formability of TTMP AZ61. The influence of texture and grain size on these parameters is discussed as well. Finally, in order to understand how the formability in TTMP AZ61 might be improved, the damage and failure processes are described.

4.1 Tensile Behavior

Representative monotonic tensile curves of the as-Thixomolded plate, as-rolled sheet, and annealed sheets loaded along the RD and TD are shown in Figure 4.1. Table 4.1 summarizes the tensile properties for these conditions as well as the results of tests in which the loading direction was 45° from the RD. Very little scatter was observed in either the yield or tensile strength of any of the materials. The maximum scatter was 14 MPa. There was much more variability in ductility. The difference in elongation to failure between the most ductile and least ductile specimens was as little a 1% strain for some conditions and as large as 13% strain for other conditions.

It was also observed that ductility between sheets could vary by 2% strain.

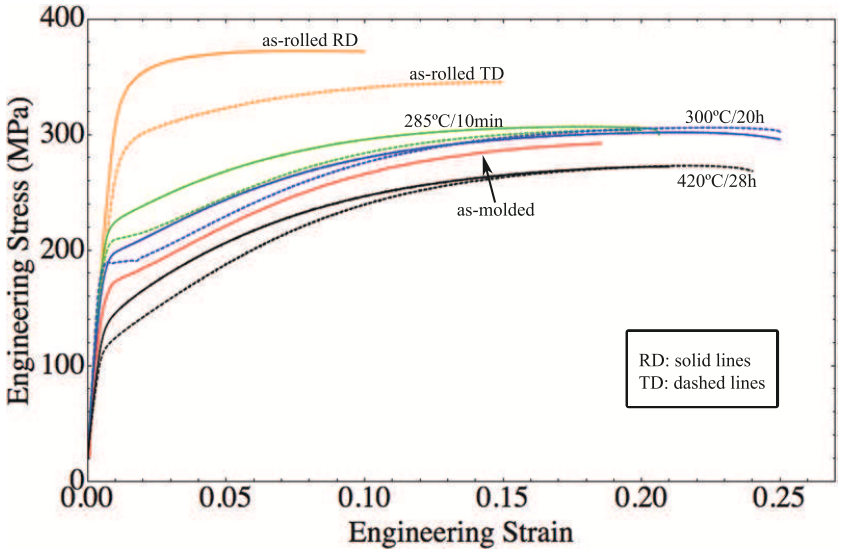

Figure 4.1: Tensile behavior along RD and TD.

Table 4.1: Tensile properties of as-molded plate and TTMP AZ61 sheet. Properties are given as an average, based on testing of 3 to 8 samples.

Thermal Treatment	**Orientation**	**YS (MPa)**	**UTS (MPa)**	**El. (%)**
as-molded		160	320	19
as-rolled	0°	320	370	10
as-rolled	45°	270	345	17
as-rolled	90°	260	345	15
285°C/10 min	0°	220	310	22
285°C/10 min	45°	215	310	26
285°C/10 min	90°	210	310	20
300°C/20 h	0°	190	300	25
300°C/20 h	45°	185	300	25
300°C/20 h	90°	185	305	25
420°C/28 h	0°	140	270	21
420°C/28 h	90°	120	270	24

The as-molded plate has a yield strength of 160 MPa and an average ductility of 19%. Rolling results in a two-fold increase in yield strength due to strain hardening as well as the presence of some dynamically recrystallized grains, which reduce the average grain size. Fine β-precipitates may also be present and increase the yield

strength by Orowan strengthening. The strain hardening leads to a reduction in the ductility.

In the sheet annealed for 285°C for 10 minutes, the establishment of a recrystallized grain size of about 3 μm results in a decrease in the yield strength to 220 MPa. The yield strength is further reduced following both the 300°C for 20 hour and 420°C for 28 hour annealing treatments.

For all sheet conditions, the orientation dependence of the tensile properties can be summarized: (1) the yield stress is highest along the RD for all conditions and decreases with increasing angle from the RD and (2) work hardening is highest along the TD for all conditions and decreases as the orientation approaches the RD. This anisotropy is the greatest in the as-rolled sheet and decreases following annealing. In the as-rolled sheet, the elongation to failure along the TD is 15%, 50% higher than along the RD. For the annealed sheets, the elongation to failure and UTS are insensitive to orientation.

TTMP AZ61L has a good balance of strength and ductility. Figure 4.2 plots the elongation to failure vs. the yield strength for various Mg alloy sheets found in the literature [1–20]. In the case where properties along more than one orientation were provided, the values were averaged. The data from this work, highlighted in red, illustrates the success of TTMP in simultaneously producing high strength and good ductility.

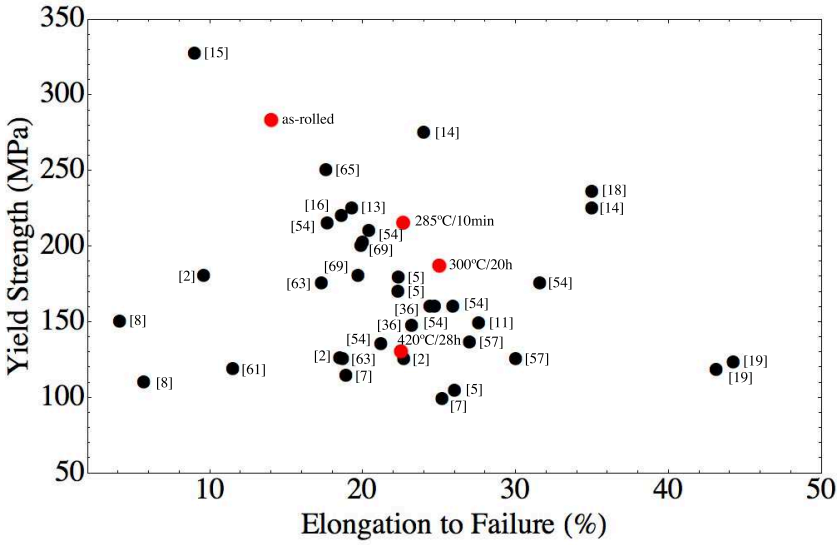

Figure 4.2: A summary the yield strength and elongation in Mg alloy sheets reported in the literature. Results from this work are indicated in red.

Two groups of researchers have been able to achieve both higher strength and ductility than obtained in the TTMP AZ61 sheet annealed for 285°C for 10 minutes, Kim et al. [14] and Miao et al. [18]. Kim and co-workers produced a 0.6mm thick sheet of AZ31 by differential speed rolling at 160°C, where the ratio of speed between the top and bottom roll was 3:1 [14]. The precursor material was a 2 mm thick plate with a grain size of 30 to 60 μm and the reduction was done in a single pass after pre-heating to the rolling temperature. Their as-rolled sheet has a similar elongation to the TTMP sheet, but a higher strength, consistent with a finer grain size (1.5 μm compared to 3.1 μm). After annealing at 200°C for 1 hour, they observed a 50 MPa decrease in strength as the grain size increased to 2.5 μm and an increase in ductility. They attribute the increase in ductility to a reduction in basal texture intensity from 11.6 to 8.2 MRD.

Miao et al. [18] produced a 0.7 mm thick AZ31 sheet by 4 warm-rolling passes with decreasing temperature. A 35% reduction in thickness was imparted per pass.

The starting material was a 4 mm thick plate with an average grain size of 25 to 40 μm. They achieved the most favorable properties, a yield stress of 236 MPa and an elongation of 35% by having a final rolling pass temperature of 160°C and then annealing at 200°C for 1 hour. This resulted in sheet with a 3 μm grain size and a basal texture with an intensity of 9.4 MRD. The texture intensity before annealing was 12.9 MRD. As observed by Kim et al., this decrease in texture strength led to an improvement in ductility. As discussed in Chapter I, ductility and formability increase with a decrease in texture. Despite the excellent performance in tensile properties of these materials, based on the texture strength, they are likely to have poor performance at ambient temperatures in forming operations requiring through-thickness deformation. Due to the fine grain sizes in these materials, high ductility is maintained despite a strong texture. In addition, grain boundary sliding likely allows for superplastic forming of these sheets at elevated temperatures [21].

4.1.1 Yield Strength

The contribution of grain size to the yield strength of the material is given by the Hall-Petch relationship (Eqn. 4.1), where σ_o is the lattice resistance of the matrix to basal slip, k is the Hall-Petch coefficient, and d is the average grain size of the material.

$$\sigma_{gs} = \sigma_o + kd^{-1/2} \tag{4.1}$$

The Hall-Petch coefficient can be orientation dependent in textured hcp materials [22–25], so we consider a separate coefficient determined for the RD and TD. Using the 0.2% offset yield strength and the grain sizes determined in Chapter III, the Hall-Petch slope for the annealed sheets is found by fitting a linear slope to σ_{YS}

versus $d^{-1/2}$. The Hall-Petch coefficients are found to be 9.1 MPa×mm$^{1/2}$ along the RD and 10.2 MPa×mm$^{1/2}$ along the TD (Table 4.2). Figure 4.3 illustrates the best fit lines for data along the RD, TD, and for all of the data in recrystallized TTMP sheets. Based on the limited number of data points, it is difficult to conclude that the orientation dependence of the Hall-Petch parameters is statistically significant.

Table 4.2: Best fit for the Hall-Petch coefficient, k, in annealed sheet.

Orientation	**YS (MPa)**	**k (MPa×mm$^{\frac{1}{2}}$)**
0°	60	9.1
90°	33	10.2
All	51	9.4

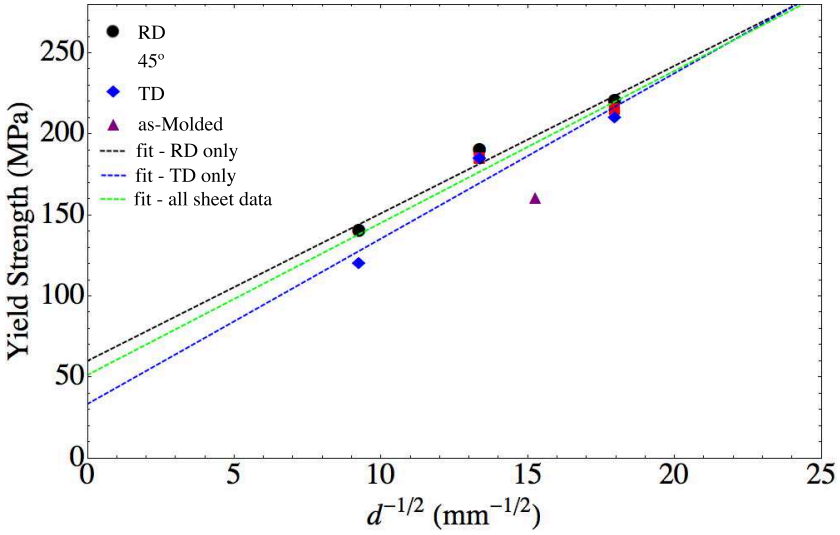

Figure 4.3: Hall-Petch Behavior of TTMP AZ61

Though it is not conclusive from the available TTMP AZ61 sheet data, it is reasonable to believe that sheet loaded along the RD will have a higher σ_o and lower k-value based on the distribution of texture in the TTMP AZ61 sheet. Armstrong observed that σ_o is related to the CRSS for basal slip (the easy slip system in Mg) [26]. A stronger basal texture intensity leads to a higher value of σ_o. σ_o is also

dependent on the Taylor factor, the more grains oriented favorably for basal slip, the lower σ_o [27]. The Hall-Petch coefficient, k, is controlled by the extent of prismatic slip activity [27–29]; as prismatic slip becomes more favorable, k decreases.

The relative activity of prismatic and basal slip are dictated by the variations in the texture intensity and texture components, which affect the fraction of grains oriented for "easy" basal slip for a specific orientation. Basal slip is the easiest when the basal plane fiber is tilted 45° from the tensile axis. We can determine the fraction of orientations (roughly proportional to the fraction of grains) oriented for soft basal slip by calculating the fraction of EBSD measurements within a certain radius of this fiber, here we use 20°; the red, dashed circles imposed on the pole figures in Figure 4.4 illustrate the area favorably oriented for basal slip along the RD. The results of this calculation for the three orientations studied are summarized in Table 4.3. As a note, in a perfectly uniform pole figure, the percentage of favorable grains for any orientation would be 12 for the criterion used here.

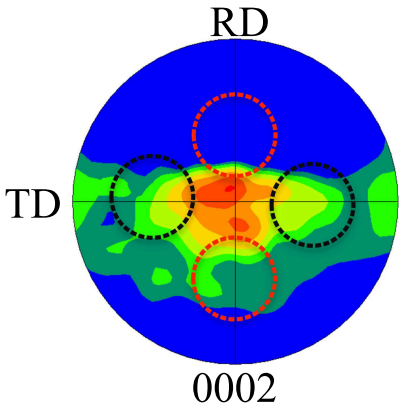

Figure 4.4: The dashed circles on the basal pole figure for as-rolled sheet indicate the regions at which grains are favorably oriented for basal slip along the RD and TD (red and black circles, respectively).

Table 4.3: Fraction of grains favorably oriented for basal slip per condition.

Thermal Treatment	**Orientation**	**Percentage of Grains Favorably Oriented for Basal Slip**
as-molded		12
as-rolled	0°	8.1
as-rolled	45°	10.9
as-rolled	90°	18.2
285°C/10 min	0°	13.2
285°C/10 min	45°	13.9
285°C/10 min	90°	15.9
300°C/20 h	0°	13.8
300°C/20 h	45°	14.9
300°C/20 h	90°	16.9
420°C/28 h	0°	14.3
420°C/28 h	90°	15.8

For each sheet condition, fewer grains are oriented favorably for basal slip along the RD than along the TD, resulting in a lower CRSS for basal slip along the TD than along the RD. Therefore, we observe that σ_{YS} is higher along the RD due to a higher value of σ_o in that direction. The ratio of the percent of favorable grains along the RD to the percent of favorable grains along the TD can be used as a rough indicator as to how much anisotropy will be observed in σ_{YS}. The as-rolled sheet exhibits the lowest ratio at 0.45, and the largest anisotropy. The annealed sheets have ratios above 0.8, and no more than 20 MPa difference in σ_{YS} between the RD and TD. Figure 4.5 illustrates the difference in anisotropy of the yield stress between the as-rolled sheet and the recrystallized sheet.

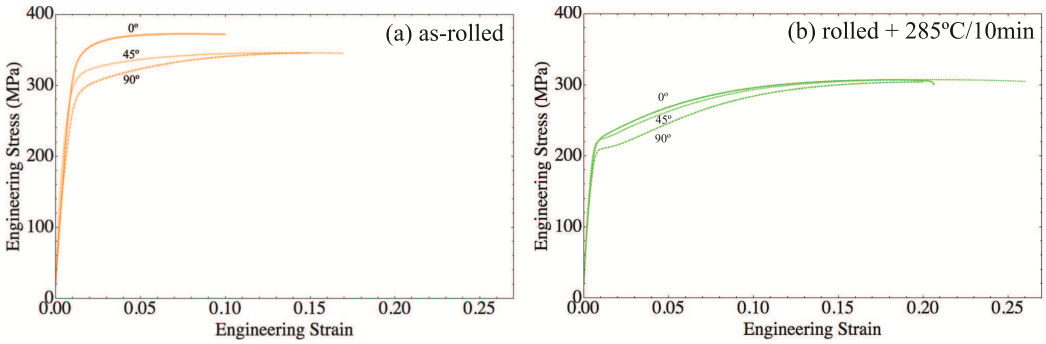

Figure 4.5: Tensile behavior along 0°, 45°, 90° for (a) as-rolled sheet and (b) sheet annealed at 285°C for 10 minutes.

The small difference between the favorable fractions in the recrystallized sheet, combined with the concurrence of grain growth and texture evolution convolute the determination of orientation dependent Hall-Petch parameters. In Mg alloys produced by equal channel angular pressing, the texture can be modified so dramatically that the materials seem to exhibit a negative Hall-Petch coefficient [30, 31]. To truly isolate the orientation effect requires a set of data representing different grain sizes, but an identical texture, a task that may be experimentally unachievable, depending on the active recrystallization and grain growth processes.

Assuming it is appropriate to describe all of the recrystallized sheet orientations with the same parameters, we arrive at a Hall-Petch coefficient of 9.4 MPa$\times$mm$^{1/2}$, which is consistent with the Hall-Petch values measured in studies of Mg-Al and Mg-Zn [32]. A comparison between these data and the average Hall-Petch coefficient for TTMP AZ61 sheets, is shown in Figure 4.6. The materials referenced in Figure 4.6, all have a strong rolling or extrusion texture [32], and are therefore expected to have a higher yield strength due to increased non-basal slip activity. This difference is observed in Figure 4.6; the yield strength in weakly textured TTMP AZ61 falls below that of the more strongly textured materials. As strain hardening is an im-

portant mechanism in the as-rolled sheet, it was not included on the plot.

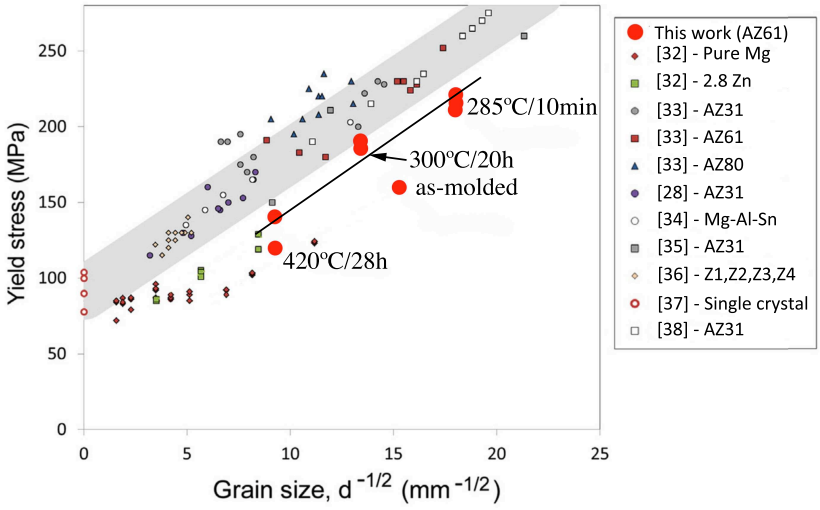

Figure 4.6: Hall-Petch Behavior of TTMP AZ61 presented with a summary Hall-Petch behavior of Mg-Al and Mg-Zn alloys by Stanford et al. [32]. Image adapted from [32], which summarizes the work of [28, 33–38]

Regardless of the particular parameters chosen, the strength in the Thixomolded plate is not well described by the Hall-Petch relationship. Based on the Hall-Petch relationship derived in the wrought sheets, the Thixomolded plate would be expected to have a yield strength of $\sim$ 200 MPa, 40 MPa higher than the observed strength of 160 MPa. Several microstructural mechanisms may be responsible for this difference. Aluminum is an effective solid solution strengthening addition to Mg, however the rapid solidification of the Thixomolded plate results in segregation of Al to the grain boundaries [39]. Cáceres studied solid solution effects in Mg-Al systems for Al concentrations between 1 and 8% and found that the change in strength due to the solution addition (in MPa) is well modeled by:

$$\sigma_{SS} \approx m B_n c^n \tag{4.2}$$

where n=½, m=5.6, B_n=21.2 (at.)$^{1/2}$, and c is the at.% Al [40]. In an AZ61 alloy with a uniform Al distribution, the expected solid solution strengthening contribution to the yield strength is only about 30 MPa. Furthermore, based on the wavelength dispersive spectroscopy measurements discussed in Chapter 3, the Al content in the interiors of grains in the Thixomolded condition is 3.3 ± 1 at.% and therefore we could expect perhaps a maximum reduction in strength due to grain boundary segregation of only 10 MPa. Other possible contributors to the reduced strength are the larger grains on the tail end of the grain size distribution, precipitation strengthening in the wrought alloys, and a lower flow stress due to easy basal slip activity in the randomly oriented as-molded plate. Yield stress in Mg alloys has been shown to be insensitive to porosity, so higher porosity in the as-molded plate is not likely to be accountable for the difference [41].

Few studies look at precipitation strengthening in AZ61, compared to AZ91, with 9 wt% Al versus 6 wt% Al [42, 43]. Kim et al. [44] observed a 13.3 HV increase in hardness after 40 h at 200°C and Hong et al. [45] reported an 11.6 HV increase after 35 h at the same temperature. Hardness (H) can be converted to yield stress (Y) by assuming H = cY, and setting c = 0.3 [46], which would then predict an increase in σ_{YS} following aging at 200°C for 35 to 40 hours to be 39 to 44 MPa.

Taking a more mechanistic approach, we can use the work by Hutchinson et al. [43] in modeling precipitation strengthening in AZ91, to approximate how much strengthening may be achieved in AZ61. Based on the shear modulus of the β-precipitates and the matrix, they predicted that dislocations will bow around any particles larger than 6 nm in diameter. Assuming a uniform distribution of precipitates and that the precipitates have the identical strength, the increase in yield

strength can be modeled by Orowan strengthening [43]:

$$\sigma_{Orowan} = \frac{MG\mathbf{b}}{2\pi\sqrt{1-\nu}}\frac{1}{\lambda}\ln\left(\frac{d_A}{r_o}\right) \tag{4.3}$$

where M is the Taylor factor (5), G is the shear modulus of the matrix (17.2 GPa), **b** is the Burgers vector for basal slip in Mg (0.32 nm), ν is the Poisson's ratio (0.35), λ is the mean particle spacing in the slip plane, d_A is the mean particle diameter, and r_o is the inner cut-off radius of the dislocation (set to **b**). For lath-shaped precipitates, the mean particle spacing is given by Eqn. 4.4, where t is the precipitate thickness and N_V is the number of precipitates per unit volume [43].

$$\lambda = \frac{1}{\sqrt{N_V * t}} - d_A \tag{4.4}$$

Hutchinson et al. determined by TEM measurements and stereographic analysis that $d_A = {}^{3.6w}/_2$, where w is the lath width, and that w=$^L/_4$ and t=$^L/_{10}$, where L is the length of the lath. L can be determined by considering the relationship between the volume of the precipitate and the volume fraction of the β-phase, f_β. Assuming a uniform distribution of particles, N_VV=N_AA = f_β, where A and V are the average precipitate area (in a planar section) and volume and N_V and N_A are the precipitate number density per unit volume and unit area, respectively. Thus, the volume of an individual precipitate can be determined by:

$$V = \frac{f_\beta}{N_V} = \pi\frac{w}{2}\frac{L}{2}t \tag{4.5}$$

In order to approximate N_V, we refer to work by Celotto on precipitation in AZ91, in which he measured a maximum number density of precipitates of $\sim 8.5 \times 10^9$ per mm^{-3} [47]. In another study, Celotto et al. [48] compared the precipitation kinetics of AZ91 to that of AZ61, and concluded that the kinetics in AZ61 are slower than those in AZ91, and that AZ61 has less growth nuclei. Since the nucleation rate is

proportional to the Al content [43] we will approximate N_V as two thirds of the maximum value measured in AZ91, $\sim 5.6 \times 10^9\ mm^{-3}$.

The maximum volume of the β-phase is limited by the amount of Al in the alloy. At equilibrium, the Al-Mg phase diagram [49] predicts the maximum weight fraction of the β-phase at 200°C is 7.7 wt%. To convert this to volume fraction, we calculate the volume of the β and α phases in 1 gram using:

$$V_\beta = \frac{wt\%\beta \times 1g}{D_\beta} \tag{4.6}$$

$$V_\alpha = \frac{(1 - wt\%\beta) \times 1g}{D_\alpha} \tag{4.7}$$

where wt % β is the equilibrium weight fraction from the phase diagram and D_α and D_β are the densities of the α and β phases in g/cm^3. From the Joint Committee on Powder Diffraction Standards (JCPDS) files #04-003-2934 and #04-003-2526, D_α is 1.74 g/cm^3 and D_β is 2.08 g/cm^3. Finally, the volume fraction of the β phase, f_β, is given by:

$$f_\beta = \frac{wt\%\beta \times 1g}{D_\beta \times V_{tot}} \tag{4.8}$$

Here, V_{tot} is a sum of Eqn. 4.6 and Eqn. 4.7. Based on this analysis, we expect an equilibrium volume fraction of 6.5% at 200°C.

Using this value, we approximate a precipitate length of $\sim$ 650 nm by solving Eqn. 4.5 for L. Therefore, the the maximum contribution to precipitate strengthening at 200°C, as determined by Eqn. 4.3 is 44 MPa or 13.2 HV in agreement with the experimentally determined measurements of 11.6 to 13.3 HV [44, 45]. This value is higher than what we might expect to see in the TTMP AZ61 materials.

As the sheet annealed for 420°C for 28 h was immediately water quenched, we do not expect any precipitates in that material. The as-rolled sheet and remaining

annealed sheet conditions have some of the Al tied up in the more massive, and non-homogeneously distributed β-precipitates discussed in detail in Chapter III. Of the β-phase containing conditions, the sheet annealed for 300°C for 20 h has the lowest fraction of massive β-particles. Electron microprobe measurements indicated 5 wt% Al in the grain interiors of this material, so an even smaller concentration of Al is available for the precipitation strengthening than the 6% assumed above, and if that Al was all tied up in fine β-precipitates it would be at the expense of the solid solution strengthening. It should be noted that an effort was made to induce the formation of age hardening precipitates by aging for 36h at 200°C following the 28 h at 420°C solution treatment in as-rolled sheet. The hardness of the solution treated coupons was 61.6 HV, with a standard deviation of 3.5 HV. After the 200°C/36 h annealing treatment the hardness was 62.2 $\pm$ 3.1 HV, thus no age hardening was observed.

Based on this analysis, and the lack of evidence of fine and uniform precipitates in the TTMP AZ61 microstructure, we will proceed assuming that difference between between the yield strength in the as-molded plate and TTMP sheets can not be accounted for by Orowan, solid solution, or Hall-Petch strengthening. The most likely explanation is that the lack of crystallographic texture allows for easy basal slip and therefore a lower σ_o value.

4.1.2 Work Hardening

Hollomon's equation (Eqn. 4.9) models work hardening as a power law relationship between the true stress and true strain. The strain hardening exponent, n, was determined by performing a least-squares fit between the Eqn. 4.9 and the experimental data (converted from an experimental stress-strain curve to a true stress-

strain curve by Eqn. 4.10 and Eqn. 4.11). An attempt was made to fit n between 5% and 15% true strain, however if a sample had a ductility less than 15%, or the log-log plot of the true stress-strain curve became non-linear before 15%, then the upper limit on ϵ_T was decreased until the plot was linear over the entire range. Figure 4.7 is a representative plot of the quality of fit for a sample of sheet annealed at 285°C for 10 minutes; this sample begins to deviate from the Hollomon hardening relationship at $\sim 14\%$.

$$\sigma_T = K\sigma^n \tag{4.9}$$

$$\epsilon_T = Ln[1+\epsilon] \tag{4.10}$$

$$\sigma_T = \sigma(1+\epsilon) \tag{4.11}$$

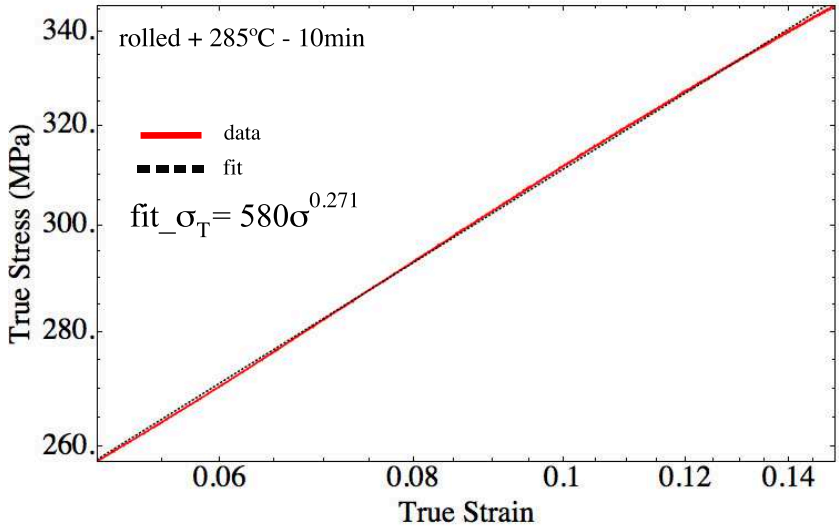

Figure 4.7: A log-log plot of the true stress-strain behavior for sheet annealed for 285°C for 10 minutes, with a best fit to the Hollomon equation between 5% and 15% strain.

Table 4.4: Strain hardening exponent of as-molded plate and TTMP AZ61 sheet

Thermal Treatment	**Orientation**	**Grain size (μm)**	**n-value**
as-molded		4.3	0.34
as-rolled	0°	NA	0.07
as-rolled	45°	NA	0.11
as-rolled	90°	NA	0.15
285°C/10 min	0°	3.1	0.21
285°C/10 min	45°	3.1	0.24
285°C/10 min	90°	3.1	0.28
300°C/20 h	0°	5.6	0.27
300°C/20 h	45°	5.6	0.30
300°C/20 h	90°	5.6	0.35
420°C/28 h	0°	11.7	0.32
420°C/28 h	90°	11.7	0.39

Table 4.4 summarizes the average strain hardening exponent calculated for each of the as-molded plate and TTMP sheet conditions. The table also includes the average grain size of each material. The work hardening exponent increases with increasing grain size. A relationship between grain size and work hardening is consistent with the rate of dislocation storage decreasing with decreasing grain size [50]. del Valle et al. [50] discuss the effect of grain size on work hardening, and conclude that the current theoretical models are insufficient due to the complexity of the problem. del Valle et al. point out that many of the same processes that affect the yield strength of the material, such as the generation, mobility, and pile-up of dislocations, also affect the work hardening behavior. With that in mind, we looked for a simple empirical relationship between work hardening and grain size.

Based on the work of Morrison, we use the following equation to relate the yield strength of a material to its work hardening coefficient [51]:

$$n = z * \sigma_{\mathrm{YS}} + n_0 \tag{4.12}$$

The value of the constants, z and n_0, were determined for each orientation using the values of n and σ_{YS} for each of the three annealing treatments. A plot of the

best fit of Eqn. 4.12 for each orientation in the annealed sheets is shown in Figure 4.8. Because there were no tests conducted at 45° from the RD for the 420°C/28 h annealing treatment, this point was approximated by averaging the properties from the RD and TD orientations, for the purposes of fitting the trend line. Based on the available data, the linear fit seems a reasonable relationship between the yield stress and the work hardening coefficient. The best fit parameters are summarized in Table 4.5.

Table 4.5: Best fit parameters for n_0 and z, from Eqn. 4.12 in annealed sheets.

Orientation	$\mathbf{n_0}$	**z (MPa^{-1})**
0°	0.511	-1.34×10^{-3}
45°	0.530	-1.31×10^{-3}
90°	0.529	-1.10×10^{-3}

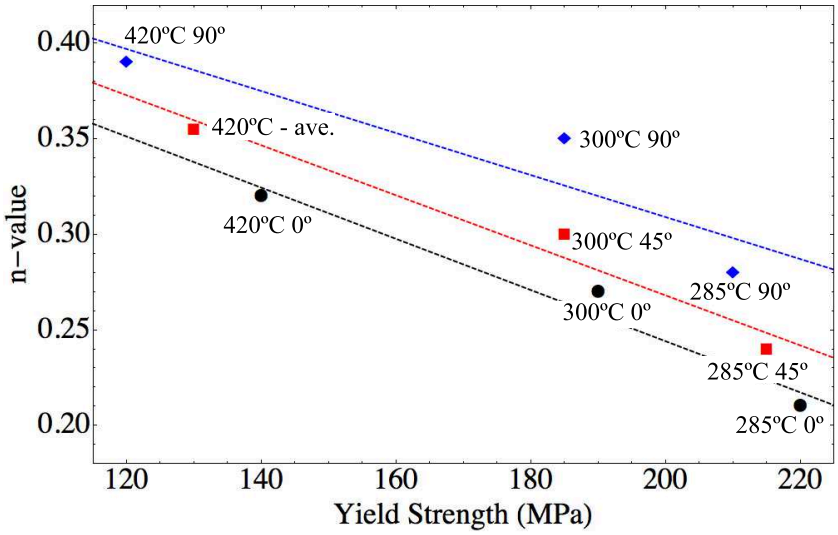

Figure 4.8: Best linear fit between Eqn. 4.12 and the tensile properties of annealed TTMP AZ61 sheets. The point for 45° from the RD for the 420°C/28 h annealing treatment was approximated by averaging the values from 0° and 90°.

Recalling our discussion on the anisotropy in the yield strength, we can use the fraction of grains favorably oriented for basal slip as a numerical parameter with which to model the effect of orientation on work hardening. Figure 4.9 plots the n-

value versus the percentage of grains oriented favorably for basal slip. The trend lines are a linear best fit; a point at (0,0) was included in each fit to ensure that a material with 0% of favorably oriented grains behaves perfectly plastically, in other words with n=0. As with Figure 4.8, Figure 4.9 indicates that the strain hardening coefficient increases with increasing angle from the RD and also increases with increasing grain size. In order to examine the effect of the texture distribution on the strain hardening coefficient, it is useful to minimize the grain size contribution to strain hardening from Figure 4.9.

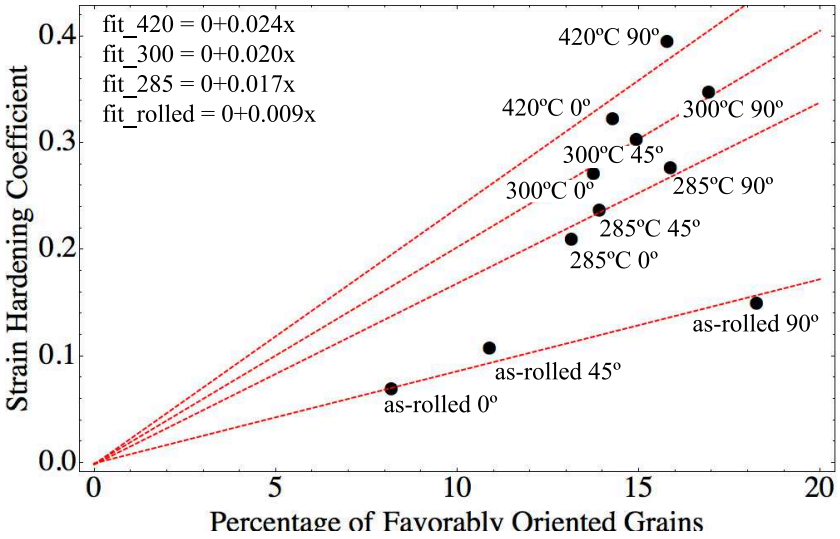

Figure 4.9: Relationship between the percentage of grains oriented favorably for basal slip and the work hardening coefficient for each TTMP sheet condition.

Referring back to Eqn. 4.12, the linear dependence between the work hardening coefficient and yield stress allows us to describe the grain size dependence of work hardening with the Hall-Petch relationship (Eqn. 4.1). The difference in yield stress between a material with an average grain size of d, and a material with an average grain size of $d_{effective}$ is given by Eqn. 4.13, where the appropriate orientation dependent value of k is used from section 4.1.1. The n-value of each condition can

be adjusted to an effective grain size by Eqn. 4.14, where σ_{YS} is the experimentally determined yield stress and z and n_0 are the orientation dependent best fit values. A grain size after the 285°C/10 min annealing treatment of 3.1 μm was used for $d_{\mathrm{effective}}$.

$$\sigma_{\mathrm{YSdiff}} = \frac{k(\sqrt{d} - \sqrt{d_{\mathrm{effective}}})}{\sqrt{d}\sqrt{d_{\mathrm{effective}}}} \tag{4.13}$$

$$n = z * (\sigma_{\mathrm{YS}} + \sigma_{\mathrm{YSdiff}}) + n_0 \tag{4.14}$$

The as-rolled material was not used to fit the relationship between the n-value and yield stress, as it does not have a well defined grain size, and has an extra contribution to yield stress from dislocation interactions. However, it has the largest orientation dependence on the percentage of favorably oriented grains, and so in order to develop the most useful model between texture (percentage of favorably oriented grains calculated from the basal pole figure) and work hardening, it would be beneficial to describe the n-value of sheet with the as-rolled texture and an effective grain size of 3.1 μm as well. Once again, Eqn. 4.13 and Eqn. 4.14 were used to determine the work hardening coefficient for a material with the same texture as the original material, but with an effective grain size of 3.1 μm. The "grain size", d, of the as-rolled material was varied between 1 and 2.5 μm in increments of 0.1 μm, and a linear best fit trend line for the resulting adjusted as-rolled n-values for each increment was determined. The difference between these trend lines and the experimental trend line for the percentage of favorable grains and the n-value in the sheet annealed for 10 min at 285°C was determined by a least squares difference in increment of 1% between the values of 8% and 19% favorably oriented grains. The results of this analysis conclude that a difference in grain size and strain hardening between the as-rolled sheet and sheet annealed for 10 min at 285°C could be best

described by assigning the as-rolled material and artificial grain size of 2.1 μm.

Figure 4.10 summarizes the adjusted n-values. The red dashed trend line, fit to all of the adjusted data points, represents the variation that might be expected for the n-value in material with an average grain size of 3.1 μm, depending on the distribution of texture. The black dashed trend line was the best fit to the experimental data for sheet annealed for 10 min at 285°C. The trend line for the adjusted n-values varies by less than 0.003 between 8 to 18% favorably oriented grains from the trend line for 285°C/10min sheet. The maximum difference of an adjusted point to the adjusted n-value trend line is 0.041. In the range of 8 to 18% one might expect to be able to predict the work hardening exponent to within 0.04 in TTMP AZ61L for any given grain size using the basal pole figure and the orientation dependent parameters of n_0, z, and k from Tables 4.5 and 4.2. At some point the linear relationship breaks down, as it predicts a strain hardening coefficient of 1.65 for a material in which all of the grains are oriented favorably for basal slip.

Based on this analysis, strain hardening is dependent on both grain size and texture. The strain hardening coefficient increases with increasing grain size, and increases with increasing favorability of basal slip. Higher strain hardening coefficients indicate more resistance to shear localization, and thus should predict materials with better formability [52].

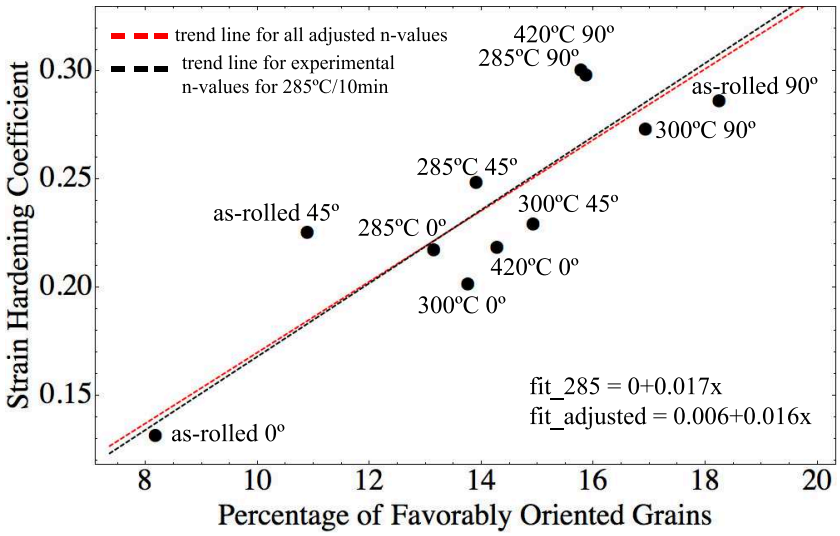

Figure 4.10: Relationship between the percentage of grains oriented favorably for basal slip and the work hardening coefficient for each TTMP sheet condition.

4.2 Lankford r-value

In order to evaluate formability, some tests on the as-rolled sheet and 285°C/10 min sheet were interrupted at 10% strain at which point the width and thickness strains were calculated for the determination of the Lankford r-value. The results are summarized in Table 4.6.

Table 4.6: The r-values in as-rolled and annealed AZ61 sheet

Material	r_0	r_{45}	r_{90}	$\bar{r}$	Δr	Δr_2
as-rolled	1.48	1.59	1.10	1.44	0.30	0.49
rolled + 285°C/10 min	0.96	1.14	1.09	1.12	0.12	0.18

The r-value, $\bar{r}$, and Δr values provide indicators as to material formability. In steel, the average r-value, $\bar{r}$, relates to the drawability of the material. In general, a high $\bar{r}$ value indicates that the material resists thinning and should have good drawing properties [52]. However, in hcp materials a high $\bar{r}$-value is associated with strong anisotropy and poor formability, and thus requires a different interpretation [20]. Instead, reduced $\bar{r}$ values in Mg-sheet indicate good formability for stretching

operations [3, 11, 20] . The $\bar{r}$-values for the TTMP AZ61L sheet material are all quite low for a Mg sheet alloy, even in the as-rolled condition. Average r-values of 3 or more are typical in commercial AZ31 sheet [1].

The association between the $\bar{r}$-value and room temperature formability is highlighted by a compilation of results from the literature in Figure 4.11. The maximum dome height achieved in an Erichsen biaxial stretch test decreases as $\bar{r}$ increases. The two black arrows indicate that dome heights of 6 to 7mm might be expected in the as-rolled TTMP AZ61 and TTMP AZ61 sheet annealed for 10 minutes at 285°C based on $\bar{r}$ in those materials and the literature-based trend line.

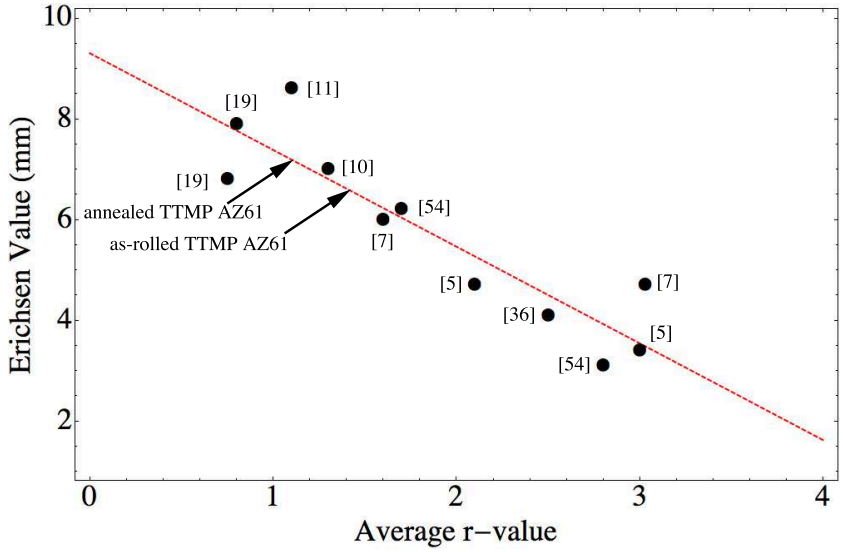

Figure 4.11: Relationship between $\bar{r}$ and Erichsen dome height at room temperature for various Mg sheets.

Calculation of Δr provides a measure of anisotropy, and predicts the extent of earing[52]. Bohlen et al. [3] discusses that earing in the hcp Mg crystal structure might be better predicted by instead looking at the maximum variation of the r-value in the sheet, $\Delta r_2 = r_{max}$ - r_{min}. In the TTMP AZ61 sheet annealed for 10 minutes at 285°C, Δr_2 is 0.18, which is very low. To the authors knowledge, the only lower

value that has been reported is 0.10 in hot rolled ZE10 [3]. Values of 1 or more for Δr_2 are not uncommon in Mg sheet [1, 3, 5–7, 12, 13, 20, 53–55]. In TTMP AZ61 Δr is also quite low, comparable with values in RE alloys [3]. Values of at least 0.3 are typical for Δr [1, 3, 5–7, 13, 19, 20, 53, 55].

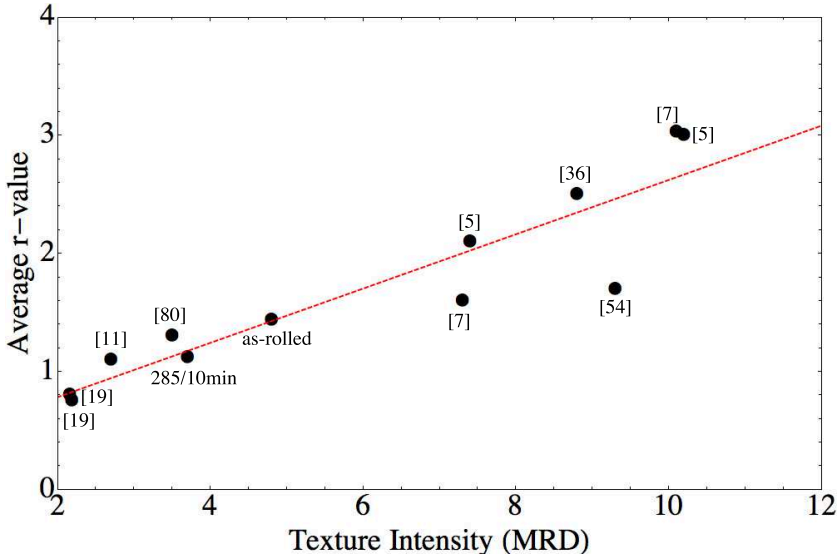

Figure 4.12: Relationship between $\bar{r}$ and basal texture intensity for various Mg sheets.

As discussed in Chapter I, the r-value is strongly dependent on texture [56]. Looking again at the same studies referenced in Figure 4.11, it is clear that $\bar{r}$ is strongly related to the maximum basal texture intensity (Figure 4.12). Values from the as-rolled and annealed TTMP AZ61 sheet are consistent with the correlation. The low r-value parameters TTMP AZ61 sheet are a direct consequence of the relatively weak texture of the material. Though room temperature formability was not studied in this dissertation, the favorable $\bar{r}$ and Δr_2 measurements, as well as the high work hardening coefficient, indicate that TTMP AZ61 sheet will perform better than commercial AZ31 sheet during ambient forming operations.

4.3 Texture Evolution During Tensile Deformation

In the discussion of yield stress and work hardening, the effect of the initial texture on the tensile behavior was explored. The texture distribution and intensity in the initial pole figure can be used as a predictor for the work hardening and yield stress anisotropy. It is also useful to look at the texture evolution during deformation. During tensile deformation slip leads to a rotation of the lattice such that the active slip direction tends to become aligned along the tensile axis and the active slip plane parallel to the tensile stress axis. Therefore, texture evolution during deformation provides an insight about the relative slip system activity. Figure 4.13 summarizes the texture evolution of samples loaded to ϵ=10% along either the RD or TD.

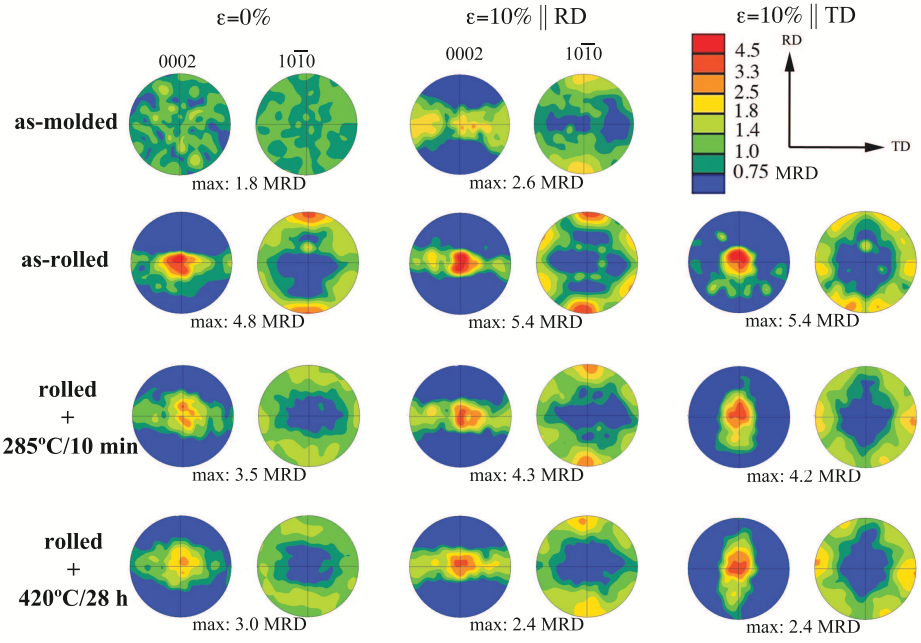

Figure 4.13: Texture evolution following 10% strain along either the RD or TD.

After deformation, the originally un-textured as-molded plate manifests a tight distribution along the TD in the basal pole figure and two strong peaks parallel to the

tensile axis in the prismatic pole figure. Sheets loaded along the RD exhibits similar characteristics, with two notable differences, (1) the distribution along the TD is denser in the RD and (2) evidence of six-fold symmetry arises in the prismatic pole figure. In sheet loaded along the TD the spread along the tensile axis in the basal pole figure is reduced, and the intensity perpendicular to the tensile axis increases. In addition, six-fold symmetry develops in the prismatic pole figure, the two strongest peaks in the prismatic pole figure are along the tensile axis in the annealed sheet materials and the peaks appear to be roughly equal in the as-rolled sheet.

The spread in the basal pole figure perpendicular to the tensile axis and the strong peaks in the prismatic pole figure parallel to the tensile axis are a result of basal slip. Basal $\langle \mathbf{a} \rangle$ slip tends to rotate the c-axis such that it becomes perpendicular to the tensile axis. This leads to the development of $\langle 10\bar{1}0 \rangle$ fiber texture and an increase in the maximum basal texture intensity [16, 20, 57]. For samples loaded along the TD, the original spread of grains along the TD is reduced as the basal plane of these favorably oriented grains rotates towards the tensile axis.

The additional component in the sheet materials, the development of the six-fold symmetry in the prismatic pole figures, is a consequence of $\langle \mathbf{a} \rangle$ slip on prismatic planes [1, 16, 28, 58]. This slip will rotate the crystals such that the normals of two of the prismatic planes are aligned with the tensile axis, the additional peaks showcase the six-fold symmetry of the hexagonal crystal. The peaks from alignment of the prismatic planes will intensify the peaks arising from rotation of the basal planes.

Based on the lack of statistics in the EBSD generated pole figures, it would be misleading to attempt to quantify the relative slip activity based on the intensity of the two texture components. However, a qualitative statement can be made by

looking at the materials with the weakest and strongest initial textures, the as-molded plate and the as-rolled sheet. The $\langle 10\bar{1}0 \rangle$ fiber texture is the only texture component that develops in the as-molded material, so it appears that basal slip was dominant in this un-textured material. The as-rolled sheet has the smallest number of grains favorably oriented for basal slip when loaded along the RD, therefore non-basal slip must accommodate a larger fraction of the deformation. Correspondingly, the texture of the as-rolled sheet loaded along the RD displays the strongest six-fold component indicating increased prismatic slip activity.

A more accurate description of the relative activity of different slip systems can be obtained by crystal plasticity modeling, which is outside the scope of this thesis. The texture of the materials determines the relative activity of each slip system, and the active slip systems determine the crystal rotations during deformation, so in an iterative fashion, one can describe the texture evolution and relative activity of each slip system during deformation. The aggregate response of the crystal rotations will also determine the width and thickness strains that develop during deformation, and so the r-value can be modeled as well. Agnew et al. [1] used a viscoplastic self-consistent model to study tensile deformation in a commercial AZ31 sheet. Though this sheet started with a stronger basal texture (>9 MRD) and less spread along the TD, the texture evolution at $\epsilon \sim 11\%$ is quite similar to that observed in the TTMP AZ61 sheets at 10% strain. They found the experimental r-value and texture evolution were best replicated by assuming that the critical resolved shear stress at room temperature for prismatic slip was 2.5 times that for basal slip.

As a final note on the texture evolution, there is an additional texture component that may arise during deformation of Mg sheets that was not observed in the TTMP AZ61 sheets. $\{10\bar{1}2\}$ extension twinning during tensile deformation rotates

the c-axis of grains from the normal direction of the sheet 86° towards the sheet direction perpendicular to the tensile axis [28, 59]. An illustration of this texture component is shown in Figure 4.14. The extent of twinning in TTMP AZ61 sheets will be discussed in more depth in the next section, 4.4.

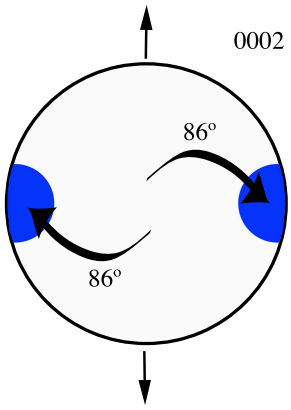

Figure 4.14: Illistration of the texture component arising in the basal pole figure due to twinning during tensile deformation in the vertical direction.

4.4 Twinning

Twinning is a common deformation mechanism in Mg, and is often credited with providing for an additional deformation mode in order to satisfy the von Mises requirement [1, 60]. However, twinning is activated more easily in compression than in tension, leading to an anisotropy that may complicate forming operations [61]. Twinning can be suppressed by grain refinement, as high local stresses are required to nucleate twins grain boundaries [62]. The tendency for hcp crystals to twin increases with the grain size [21, 63]. The extent of twinning at ϵ=10% and failure was investigated in the as-molded plate and the as-rolled and annealed TTMP AZ61 sheets through observation of the microstructure and EBSD mapping.

At 10% strain, in materials with an average grain size less than 10 μm (the as-molded plates, as-rolled sheet, and sheets annealed for 285°C/10min and those annealed for 300°C/20 hours) only a few twins are observed by SEM. The black arrows in Figure 4.15(a) highlight some of the twins in the 285°C/10min sheet when loaded along the RD. A larger area fraction of twins is observed in the larger (11.7 μm) grained 420°C/28 h sheet (Figure 4.15(b)).

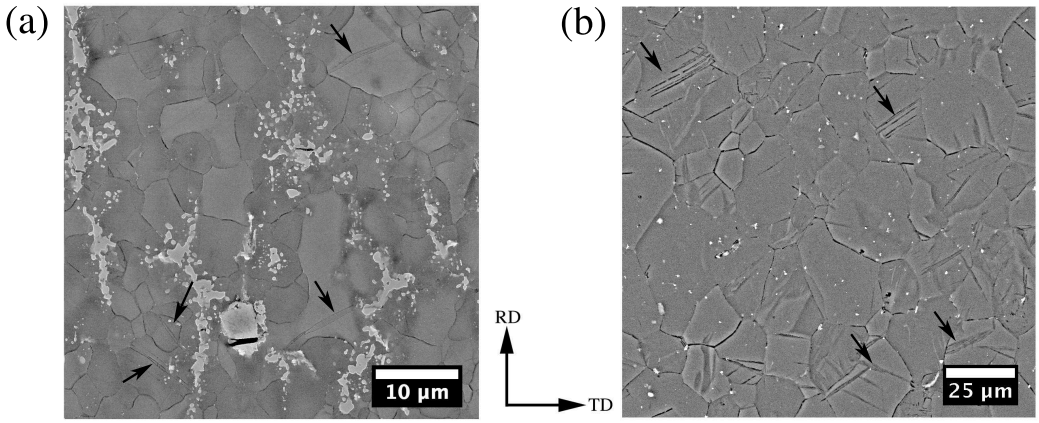

Figure 4.15: SE micrographs highlighting twinning in (a) sheet annealed for 285°C/10min and (b) sheet annealed for 420°C/28h at ϵ=10% along the RD.

In order to confirm that the highlighted features are in fact twins, and if so, to determine their nature, EBSD twin maps were generated for the deformed materials. By using the orientation data provided by EBSD to isolate the orientation relationships commonly observed in twinning of Mg, it was determined that only $\{10\bar{1}2\}\langle 10\bar{1}1\rangle$ extension twins are present at ϵ=10%. These twins are highlighted in red in the EBSD twin maps shown in Figure 4.16. Comparison of (a) sheet annealed for 285°C/10min and (b) sheet annealed for 420°C/28h reveals that twinning is more prevalent in the larger grained material at 10%. Indeed, in the fine grained materials, twins accounted for less than 1% of the total area. In the larger grained sheet,

twins account for approximately 6% of the total area. However, as $\sim$ 2% of the area is twinned in undeformed sheet following 420°C/28h, only a 4% area fraction is attributed to deformation twinning. It should be noted, that based on the selected step size, the minimum detectable twin width is 0.6 μm.

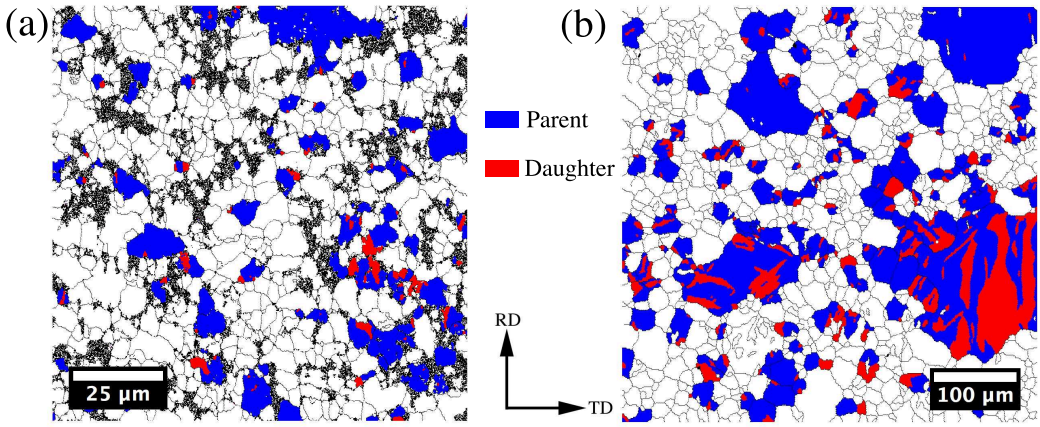

Figure 4.16: EBSD twinning maps highlighting $\{10\bar{1}2\}\langle 10\bar{1}1\rangle$ extension twins in (a) sheet annealed for 285°C/10min and (b) sheet annealed for 420°C/28h at ϵ=10% along the RD.

Following fracture, SEM reveals that twinning is more prevalent near the fracture surface. The disparity between the extent of twinning in the large and fine grained materials is even more evident at the higher strain. Figure 4.17 shows the microstructure, once again, in (a) sheet annealed for 285°C/10min and (b) sheet annealed for 420°C/28h. These micrographs were taken approximately 1 mm from the fracture surface in specimens that failed near ϵ=20% along the RD. In the 285°C/10min sheet approximately 5% of the area is twinned, whereas twinning is much more extensive in the 420°C/28h sheet. EBSD maps were not collected on these specimens, as the level of deformation would not provide for quality indexing. At both 10% and failure, the amount of twinning was similar between the RD and TD orientations.

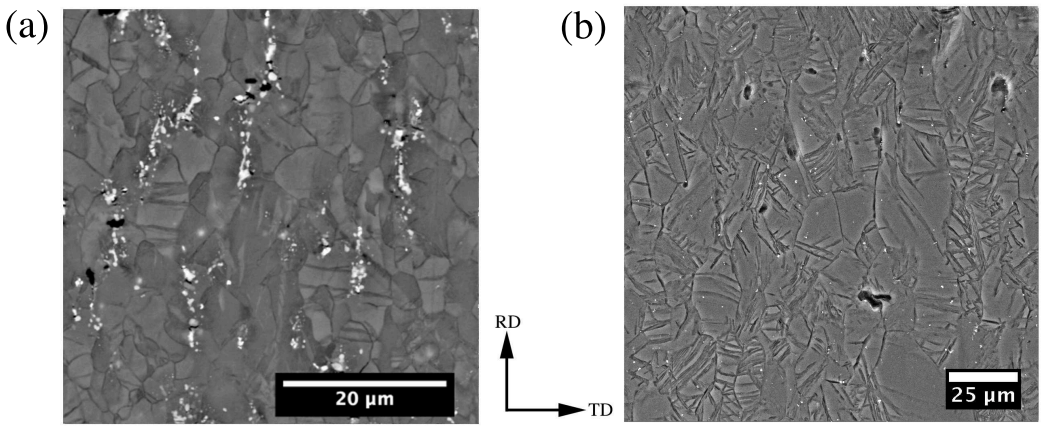

Figure 4.17: BSE micrographs highlighting twinning in (a) sheet annealed for 285°C/10min and (b) sheet annealed for 420°C/28h approximately 1 mm from the fracture surface. Both samples have a failure elongation of ∼19% along the RD.

The grain size dependency of twinning observed in the as-molded and TTMP AZ61 sheets is similar to that observed by Chino et al. [64] in AZ31. Chino et al. observed a twin area ratio less than 2% up to failure (at 20% strain) in material with an 8 μm grain size, and more extensive twinning in material with a grain size of 69 μm. The texture of the large and fine-grained annealed sheets are comparable (all have a basal texture with a maximum intensity between 2.4 and 3.7 MRD), so it is reasonable to attribute the difference to grain size alone. Sheet with a strong basal texture is unfavorably oriented for $\{10\bar{1}2\}\langle 10\bar{1}1\rangle$ tensile twinning, so limited twinning in such materials is likely more a result of texture than grain size [65]. Twinning itself is only able to contribute a maximum of 7% strain along the tensile axis [66], so the main contribution of twinning is the reorientation of grains such that slip becomes more favorable [4, 60].

4.5 Damage Evolution During Tensile Deformation

It is a commonly held belief that cracking in the β-phase initiates tensile fracture. In order to access the contribution of the β-phase to failure, damage accumulation during deformation was explored using interrupted tensile tests. In order to understand the mechanisms of damage initiation, specimens were loaded to a specific plastic strain and then unloaded, and examined in the SEM. The tensile curve for the interrupted test along the RD of the recrystallized sheet can be seen in Fig. 4.18. After a tensile specimen was reloaded, there was a small amount of static strain aging, otherwise the properties of the interrupted tests are equivalent to those found in the monotonic tests.

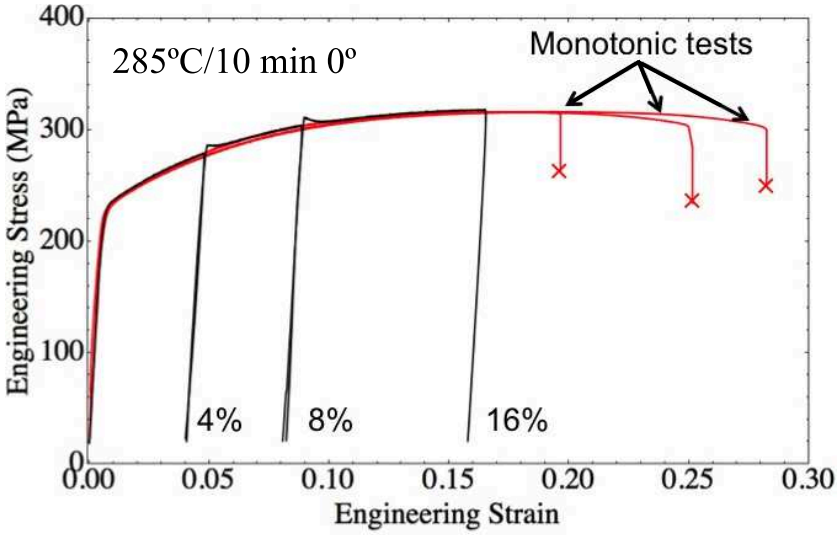

Figure 4.18: Interrupted and monotonic engineering stress -strain curves along the RD of sheet annealed for 285°C/10min.

In some of our early studies, the samples were not polished before SEM examination, so there is some surface topography caused by the rotation of grains at the surface. This rotation leads to triple junctions and displacements at the grain

boundaries that makes it appear that grain boundary sliding could be an active deformation mechanism. In specimens in which at least 50 μm has been removed from the surface by grinding and polishing there is no indication that grain boundary sliding is active in the bulk of these materials. Figure 4.19(a) shows an area of surface of an sheet specimen annealed at 285°C for 10min and loaded to ϵ=16% along the TD. The black arrows indicate displacements at grain boundaries. In comparison, when looking at the bulk behavior of the sheet under the same conditions in Figure 4.19(b), no evidence of grain boundary sliding is observed. The grain boundary displacements seem to only be a surface effect, and thus only the damage observed in samples polished after deformation will be discussed further. As a note, grain boundary sliding at room temperature in AZ31 alloys with a similar grain size has been reported [21, 67]. In these studies, by measuring step heights on the surface of tensile specimens, the contribution of grain boundary sliding was determined to be of 8% of the total strain. The authors did not report analysis of the sub-surface deformation.

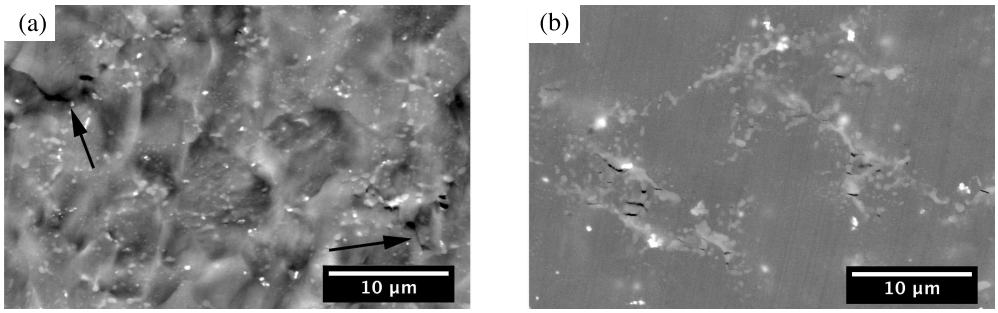

Figure 4.19: The microstructure of sheet annealed for 285°C/10min and loaded to ϵ=16% along the TD at the (a) surface and (b) subsurface. The black arrows indicate displacements at grain boundaries.

Since the 285°C sheet exhibits the best balance of strength and ductility, we concentrated our efforts on characterizing the damage accumulation for this condition.

The damage at increasing levels of strain along either the RD or TD is summarized in Figure 4.20. During the interrupted tensile tests of the 285°C sheet, the first signs of damage in the microstructure are observed at 4% plastic strain (Fig. 4.20(a) and Fig. 4.20(b)). At this point cracks begin to appear in the β-particles. As the strain is increased to 8% the crack width and density increases (Fig. 4.20(c) and Fig. 4.20(d)). At 16% strain cracks that initiated earlier continue to open and the crack density increases as more cracks continue to develop. The cracks remain confined almost exclusively to the β-network; no propagation of cracks into the matrix is observed (Fig.4.20(e) and Fig.4.20(f)). The small, bright particles in these micrographs are Al and Mn intermetallics.

One of the objectives of this work was to determine if the tendency for strings of β-particles to be aligned along the RD would affect the growth of these cracks. Analysis of the crack lengths and number density in the recrystallized sheet from a nominal area of 20,000 μm^2 for each strain level are found in Fig. 4.21. At 4% strain the average crack length is longer when loaded along the TD than along the RD, however there are $\sim$ 2.5 more cracks per 1000 μm^2 when loaded along the RD. It should be noted that the standard deviation for the crack length at 4% strain along the TD is the largest as a result not only of the presence of some long cracks, but also due to the limited number of cracks at this deformation level; the 4% TD specimen had the lowest crack density. The longest crack observed in the TD specimen at 4% is 17.9 μm, compared to 10.7 μm in the RD specimen. As the strain increases to 8% and then 16% the crack number density increases for both orientations, but the difference between the two orientations remains constant as shown in Fig. 4.21(b). The average crack length (and standard deviation) along the TD decreases, while the average crack length in annealed sheet loaded along the RD increases moderately.

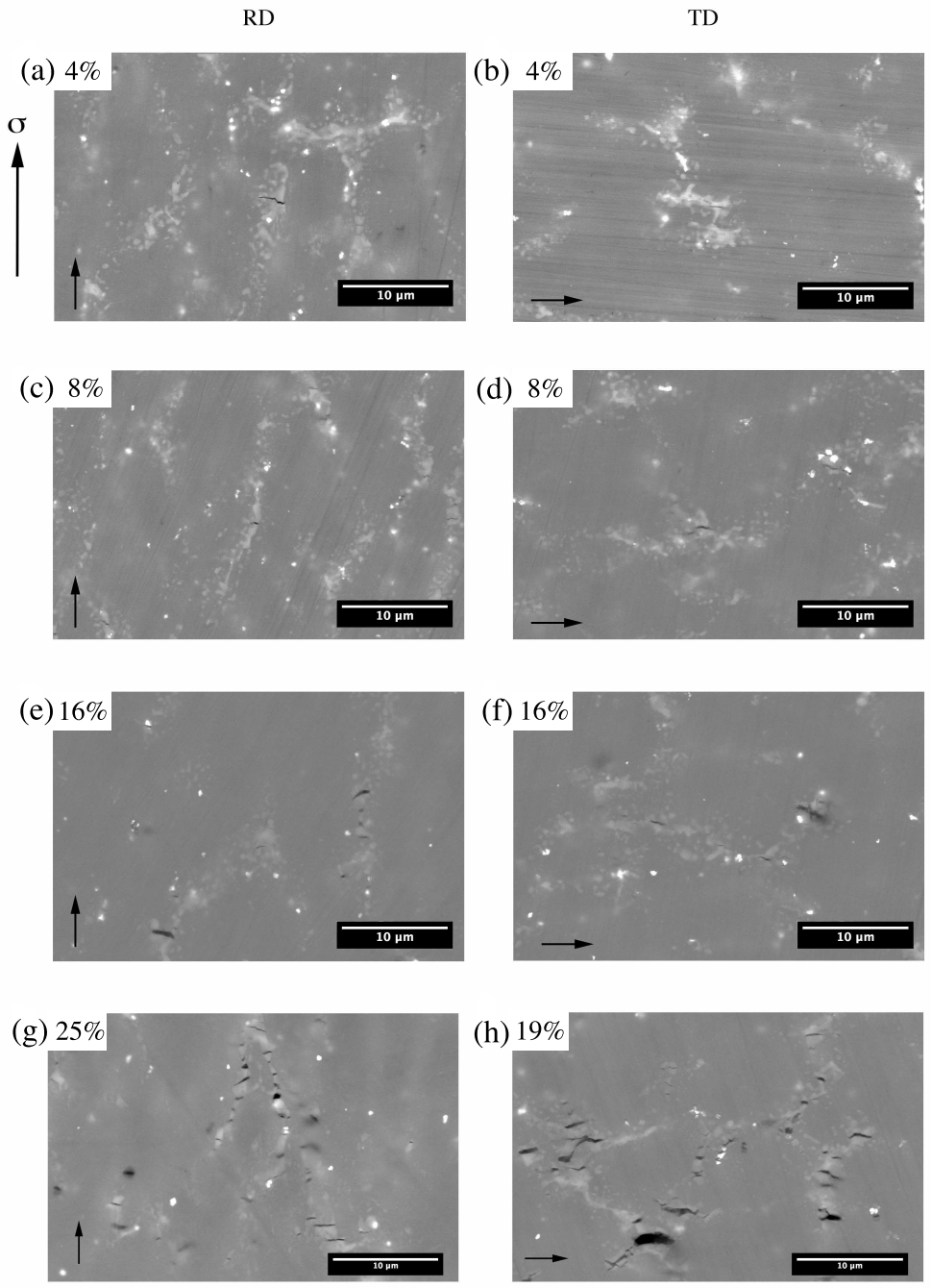

Figure 4.20: Damage accumulation in sheet annealed for 285°C for 10 min when loaded along the RD (right) and TD (left) at increasing levels of deformation.

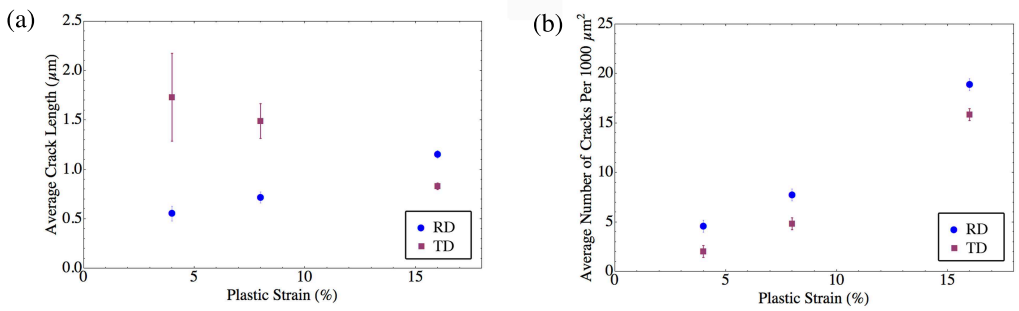

Figure 4.21: Graphs comparing (a) the average crack length and (b) the crack number density at 4%, 8%, and 16% along the RD or TD in sheet annealed for 285°C for 10 min.

Assuming a homogenous matrix and a uniform particle spacing, strain incompatibility between the matrix and β-phase will be the greatest for the larger particles, and so the increasing internal stresses cause the larger particles will fracture (or debond) first. Successive cracks will occur in increasingly smaller particles. If the local stress is not sufficient to for propagation of the crack into the matrix, then the crack arrests at the matrix/particle interface and so the maximum crack length is limited by the particle length in the plane of maximum stress. In this scenario, the mean crack length would decrease with increasing strain. The initial difference between the crack length in the two orientations at 4% strain is likely a consequence of elongation of the particles, especially those larger than 1 μm, along the RD.

A quick approximation for the effective particle length along each direction can be defined by constructing a bounding box around each particle as described in Section 3.6. By plotting the aspect ratio of the bounding box (the ratio of the length along the RD to the length along the TD) for different sized grains, as done in Figure 4.22, we can see that while the majority of grains have an aspect ratio near 1 (the average is 1.3), by isolatating increasing larger β-particles, it becomes evident that there is a population of large particles with a high aspect ratio. One of these large, high aspect

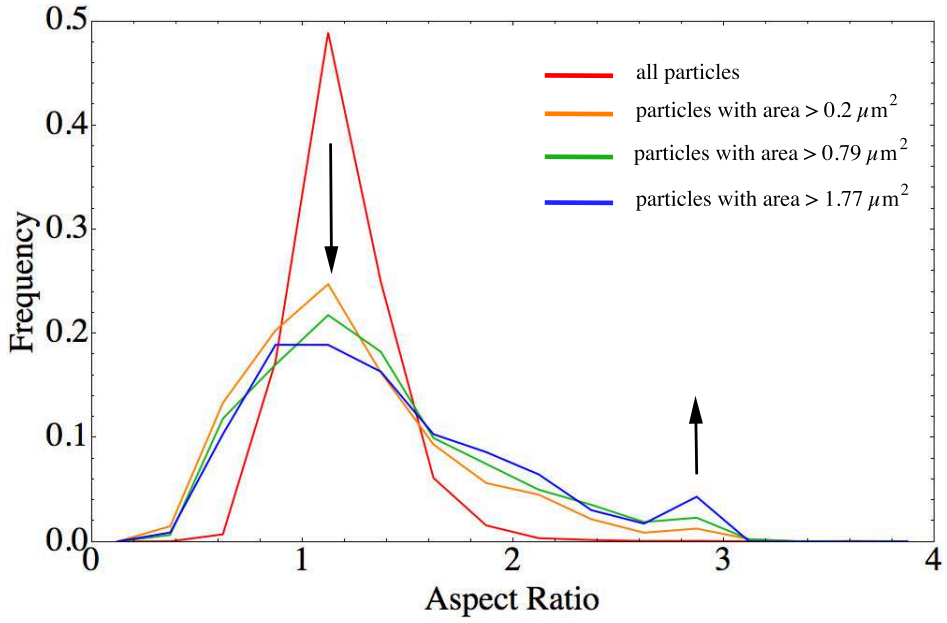

Figure 4.22: Distribution of the aspect ratio of the bounding box for different sized β-particles.

ratio particles is apparent in Figure 3.42. This small population of large, elongated β-particles is likely responsible for the initial difference in the crack length at 4% between the samples loaded along the TD and those loaded along the RD. As most of the particles are roughly equiaxed, as the number of cracked particles increases, the difference in average crack length between the two orientations decreases.

The damage process described in the sheet annealed for 285°C for 10 min is comparable to that observed in the other β-phase containing materials (the as-molded plate, as-rolled sheet, and sheet annealed for 300°C for 20h). The β-particles begin to fragment at 4% strain and the crack density then increases with increasing strain. In all of the materials, crack length and number density are limited by the morphology of the β-phase, so for example in the sheet annealed for 300°C for 20h, which has a β volume fraction of 3% (compared to 4.8% after the 285°C for 10 min anneal), there is less damage observed. In the solution treated sheet (420°C/28 h) damage is not

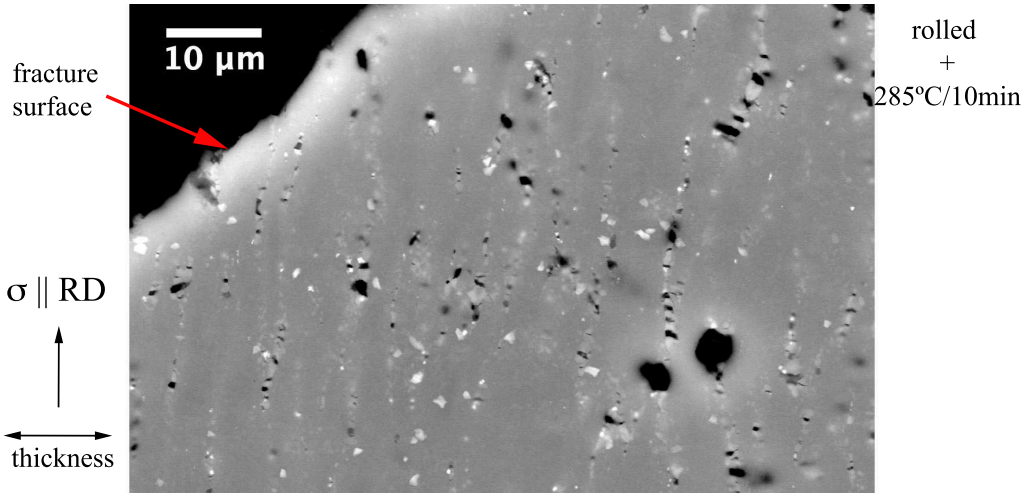

Figure 4.23: Damage near the fracture surface in sheet annealed for 285°C for 10 min and loaded along the RD. The majority of voids are associated with the β-particles.

observed until failure, and is only evident very near the fracture surface.

Despite the variations in the crack length and crack density between different orientations and different treatments, the samples (excluding the as-rolled sheet, in which the ductility is negatively affected the the strain hardening present from rolling) the average elongation to failure only varies from 19% to 26%. Thus it seems that damage associated with the β-phase has a minimal effect on ductility. Examination of tensile specimen polished to mid-width post-mortem shows minimal evidence of coalescence of the voids associated with the β-phase (Figure 4.23). Thus we turn to fractography to better understand the mechanism responsible for failure in the as-molded and TTMP AZ61 sheet conditions.

4.6 Fractography

Macroscopically, shear fracture terminated tensile deformation. The average shear angle is 50° in the as-rolled and annealed sheets and 60° in the as-molded plates.

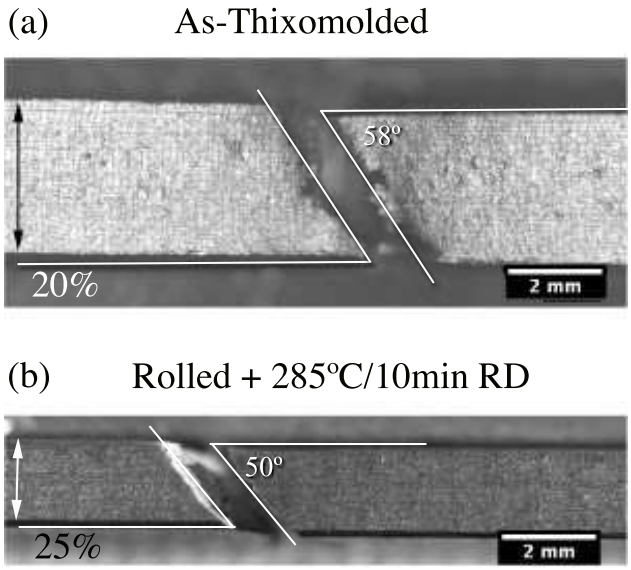

Figure 4.24: Shear angle in (a) as-molded plate and (b) sheet annealed for 285°C for 10 min and loaded along the RD. The vertical arrows indicate the thickness direction.

Figure 4.24 shows two representative samples. The average is slightly higher in the as-molded condition as a few of the specimens had a shear angles of $\sim 70°$. The higher shear angles, and lower ductility in some of the as-molded specimen may be a result of the porosity in this condition. In Mg alloys failure commonly occurs near the plane of maximum shear stress [68]. An attempt to observe the formation of shear bands on tensile specimen polished before deformation was unsuccessful, so it is likely that failure occurs soon after shear localization. Similarly, necking was limited and observed in only a few of the higher ductility samples.

Fractography indicates that microvoid coalescence is the dominant failure mechanism for all of the material conditions. Figures 4.25 and 4.26 compare the fracture surfaces of the (a) as-molded and (b) as-rolled materials as well as sheets annealed for either (c) 285°C for 10 min or (d) 420°C for 28 hours. The dimples are finest in the as-rolled sheet, in the other materials the dimple size is on the order of a

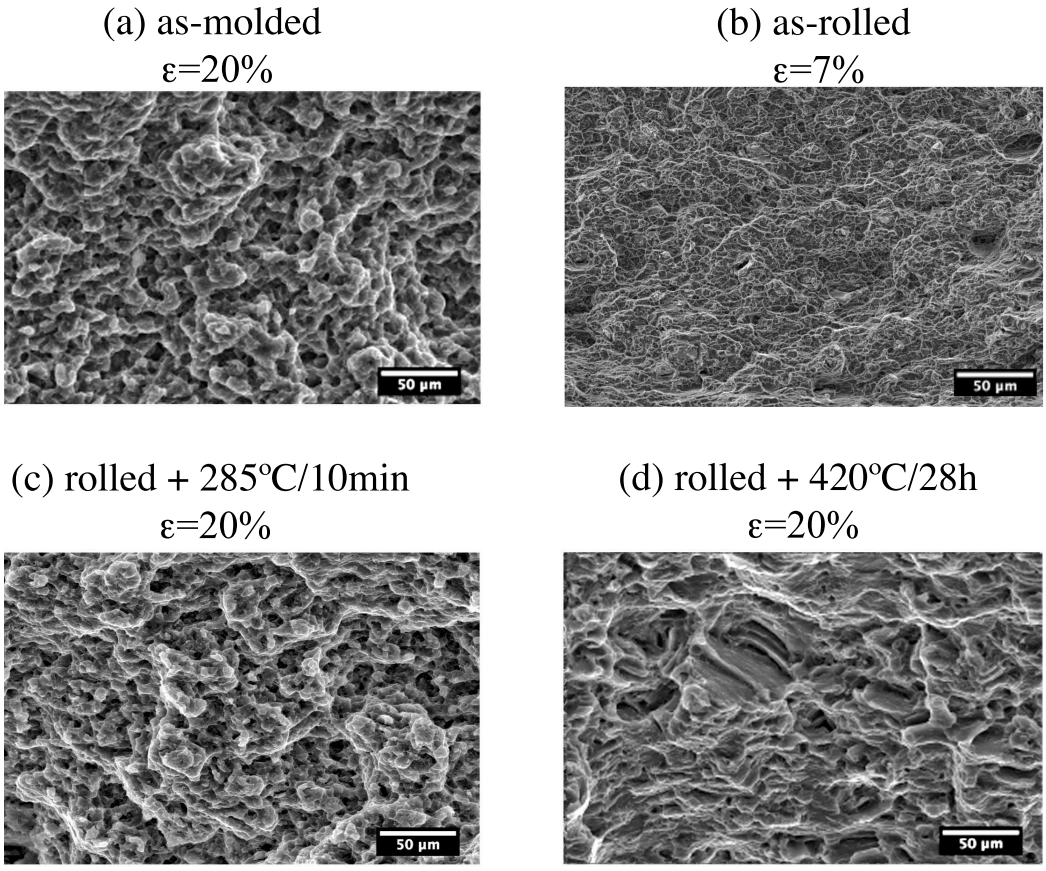

Figure 4.25: SE images of fracture surface in (a) as-molded, (b) as-rolled, (c) rolled and annealed for 285°C for 10 min, and (d) rolled and annealed for 420°C for 28 hours.

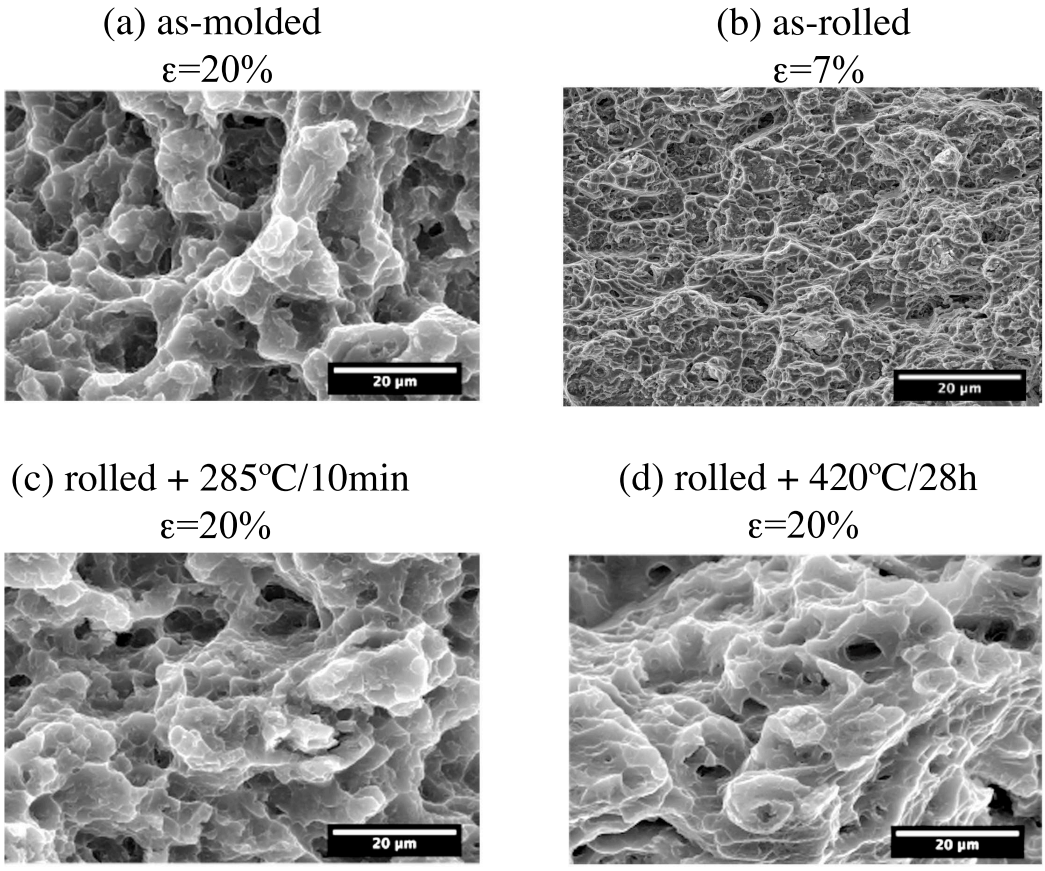

Figure 4.26: Higher magnification SE images of fracture surface in (a) as-molded, (b) as-rolled, (c) rolled and annealed for 285°C for 10 min, and (d) rolled and annealed for 420°C for 28 hours.

few micrometers. In the largest-grained material, sheet annealed for 420°C for 28 hours, several coarser features are apparent (Figure 4.25(c)). These features may be a result of void nucleation at twins, which are much more numerous in this material or indicate a transition to a more cleavage type failure due to the larger grain size. In addition, a few 50 to 100 μm more cleavage-like features were observed in an as-molded sample was well. Figure 4.27 shows one of these features, which based on its size, is likely failure in one of the externally solidified grains.

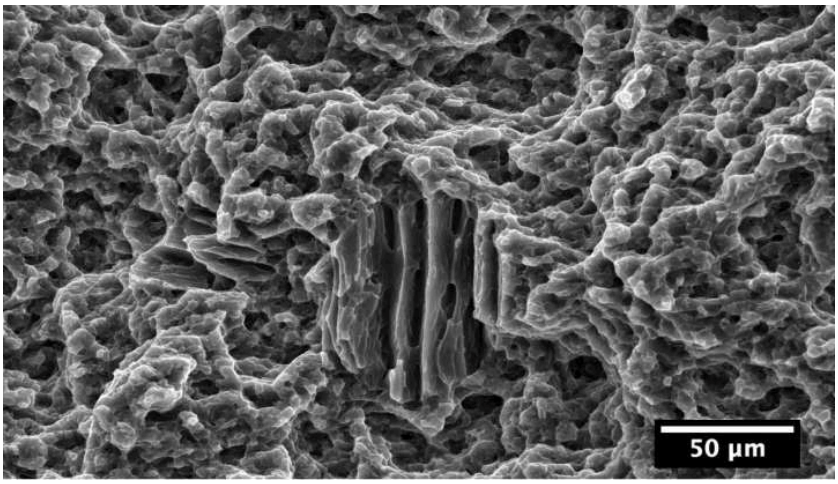

Figure 4.27: SE image of a portion of the fracture surface in the as-molded plate exhibiting a large, more cleaveage-like feature

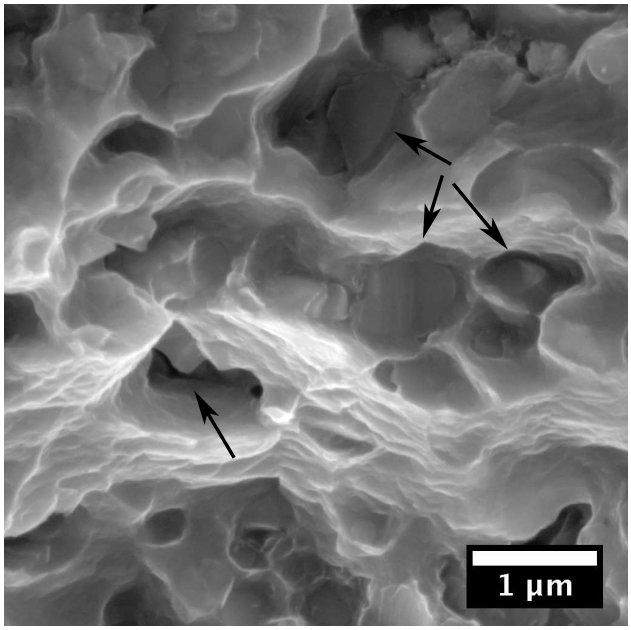

Figure 4.28: SE micrograph of fragmented β-particles at the bottom of voids in the sheet annealed for 285°C for 10 min.

Fragmented β-particles, such as those highlighted in Figure 4.28 are observable in the bottom of many of the pores. Based on observations of failed specimens at mid-width, such as the one shown in Figure 4.23, this is a consequence of the intersection of the microvoids nucleating in the shear band with voids associated with the β-phase. The particles themselves are not directly responsible for failure, though they may affect the development of the shear localization.

Microvoid coalescence has been observed by several authors in Mg alloy sheets [4, 69–73]. Grain size is one of the most important parameters in controlling the failure in Mg alloy sheets, a brittle to ductile transition can be observed with grain refinement [18, 74, 75]. Based on these studies, 10 μm seems to a benchmark below which microvoid coalescence in the dominant mechanism, though some larger grained materials, such as 41 μm SiC reinforced AZ91 studied by Luo, also exhibit uniform

dimples. Fractography in the TTMP AZ61 is consistent with an evolution in the failure mode to include more cleavage-like behavior as the grain size exceeds 10 μm. In addition to grain size, brittle failure has also been attributed to the nucleation of voids on cracked secondary particles [76]. As observed in TTMP AZ61, particles often observed in the bottom of dimples [69, 70, 73, 76]. These cracks may terminate ductility if the β-particles become too large [76] or too numerous [69], but otherwise, as observed in the as-molded plates and TTMP AZ61 sheets, may not play a significant role in failure.

4.7 Summary

The tensile behavior in TTMP AZ61 is controlled primarily by the grain size and crystallographic texture. In the annealed sheets, the yield strength varied in accordance with the Hall-Petch relationship, though texture affected the yield strength as well. In conditions where fewer grains were oriented for easy, basal slip, the yield strength increases. This is likely a consequence of mechanisms with a higher CRSS, such as prismatic slip, having to accommodate a larger fraction of the strain. The texture evolution during tensile deformation is consistant with the activation of prismatic slip in the sheet materials. Similarly, work hardening was also found to correlate with the texture, the work hardening exponent decreases as the fraction of grains oriented for basal slip decreases. These texture dependencies generate anisotropic deformation behavior in the plane of the sheet. Texture reduction during static recrystallization decreases this anisotropy.

Despite some anisotropy arising from the non-symmetric distribution of the basal poles, the low basal texture intensity leads to excellent r-values. Materials with

similar r-values have performed well during stretch forming at ambient temperature. The balance of strength and ductility combined with the low r-values in the annealed sheets indicates that TTMP is an outstanding processing route for the production of Mg sheet with better formability than conventional AZ31.

During tensile deformation, damage accumulates preferentially in the β-phase particles. However, this damage does not lead to premature failure and low ductility. In all of the annealed sheets, fractography indicates that failure results from coalescence of voids in the α-Mg matrix. Indeed, the average ductility to failure was near 23% in the annealed sheets, regardless of grain size or β-phase volume fraction. This indicates, that at least in terms of tensile deformation, the beneficial properties of the β-particles discussed in Chapter III, namely texture weakening and grain size stability, outweigh consequences of the damage developing in the particles.

An increase in grain size to 11.7 μm following the 420°C for 28 hours annealing treatment leads to a dramatic increase in twinning activity. Fractographic evidence of more brittle features also begin to manifest at this grain size. This is consistent with the body of Mg literature; grain refinement leads to an improvement in both strength and ductility. The control of the grain size and texture, achieved by TTMP, is essential to produce formable Mg alloy sheet.

Bibliography

1. S. Agnew and O. Duygulu, *International Journal of Plasticity*, 21 (6) (2005), 1161–1193.

2. I. Bayandorian, I. Stone, Y. Huang, and Z. Fan, *Magnesium Technology*, eds. S. Mathaudhu, W. Sillekens, N. Hort, and N. Neelameggham (Wiley, 2012), 135–140.

3. J. Bohlen, M. R. Nurnberg, J. W. Senn, D. Letzig, and S. Agnew, *Acta Materialia*, 55 (2007), 2101–2112.

4. A. N. Chamos, S. G. Pantelakis, G. N. Haidemenopoulos, and E. Kamoutsi, *Fatigue & Fracture of Engineering Materials & Structures*, 31 (9) (2008), 812–821.

5. Y. Chino and M. Mabuchi, *Scripta Materialia*, 60 (6) (2009), 447–450.

6. Y. Chino, M. Mabuchi, R. Kishihara, H. Hosokawa, Y. Yamada, C. Wen, K. Shimojima, and H. Iwasaki, *Materials Transactions*, 43 (10) (2002), 2554–2560.

7. Y. Chino, K. Sassa, and M. Mabuchi, *Journal of Materials Science*, 44 (7) (2009), 1821–1827.

8. H. N. Choi, Y. W. Chae, J. D. Park, H. S. Lee, and J. J. Kim, *Magnesium Technology*, eds. S. Mathaudhu, W. Sillekens, N. Hort, and N. Neelameggham (Wiley, 2012), 1043–1048.

9. G.-S. Huang, H.-C. Li, B. Song, and L. Zhang, *Transactions of Nonferrous Metals Society of China*, 20 (1) (2010), 28–33.

10. X. Huang, K. Suzuki, and N. Saito, *Scripta Materialia*, 61 (4) (2009), 445–448.

11. X. Huang, K. Suzuki, Y. Chino, and M. Mabuchi, *Journal of Alloys and Compounds*, 509 (28) (2011), 7579–7584.

12. X. Huang, K. Suzuki, A. Watazu, I. Shigematsu, and N. Saito, *Journal of Alloys and Compounds*, 470 (1-2) (2009), 263–268.

13. F. Kaiser, D. Letzig, J. Bohlen, A. Styczynski, C. Hartig, and K. Kainer, *Materials Science Forum*, 419-422 (2003), 315–320.

14. W. Kim, J. Lee, W. Kim, H. Jeong, and H. Jeong, *Scripta Materialia*, 56 (4) (2007), 309–312.

15. W. Kim, J. Park, and W. Kim, *Journal of Alloys and Compounds*, 460 (1-2) (2008), 289–293.

16. J. Koike and R. Ohyama, *Acta Materialia*, 53 (2005), 1963–1972.

17. M. Masoumi, F. Zarandi, and M. Pekguleryuz, *Materials Science and Engineering: A*, 528 (3) (2011), 1268–1279.

18. Q. Miao, L. Hu, G. Wang, and E. Wang, *Materials Science and Engineering: A*, 528 (22-23) (2011), 6694–6701.

19. D. Wu, R. Chen, and E. Han, *Journal of Alloys and Compounds*, 509 (6) (2011), 2856–2863.

20. S. Yi, J. Bohlen, F. Heinemann, and D. Letzig, *Acta Materialia*, 58 (2) (2010), 592–605.

21. J. Koike, T. Kobayahi, T. Mukai, H. Watanabe, M. Suzuki, K. Maruyama, and K. Higashi, *Acta Materialia*, 51 (2003), 2055–2065.

22. G. Proust, C. Tomé, and G. Kaschner, *Acta Materialia*, 55 (6) (2007), 2137–2148.

23. B. S. Fromm, B. L. Adams, S. Ahmadi, and M. Knezevic, *Acta Materialia*, 57 (8) (2009), 2339–2348.

24. W. Yuan, S. Panigrahi, J.-Q. Su, and R. Mishra, *Scripta Materialia*, 65 (11) (2011), 994–997.

25. G. Bhargava, W. Yuan, S. Webb, and R. Mishra, *Metallurgical and Materials Transactions A*, 41 (1) (2009), 13–17.

26. R. Armstrong, *Acta Metallurgica*, 16 (1968), 347–355.

27. G. Sambasiva Rao and Y. V. R. K. Prasad, *Metallurgical Transactions A*, 13A (December) (1982), 2219–2226.

28. A. Jain, O. Duygulu, D. Brown, C. Tomé, and S. Agnew, *Materials Science and Engineering: A*, 486 (1-2) (2008), 545–555.

29. G. Sambasiva Rao and Y. V. R. K. Prasad, *Scripta Metallurgica*, 17 (1983), 147–151.

30. V. N. Serebryany, T. Ivanova, T. Savyolova, and S. V. Dobatkin, *Solid State Phenomena*, 160 (2010), 159–164.

31. W. Kim, S. Hong, Y. Kim, S. Min, H. Jeong, and J. Lee, *Acta Materialia*, 51 (11) (2003), 3293–3307.

32. N. Stanford and M. Barnett, *International Journal of Plasticity*, 47 (2013), 165–181.

33. J. Bohlen, P. Dobron, J. Swiostek, D. Letzig, F. Chmelik, P. Lukac, and K. Kainer, *Materials Science and Engineering: A*, 462 (1-2) (2007), 302–306.

34. H.-Y. Wang, E.-S. Xue, W. Xiao, Z. Liu, J.-B. Li, and Q.-C. Jiang, *Materials Science and Engineering: A*, 528 (29-30) (2011), 8790–8794.

35. N. Stanford and M. Barnett, *Journal of Alloys and Compounds*, 466 (1-2) (2008), 182–188.

36. E. Meza-Garciá, J. Bohlen, D. Letzig, and K. Kainer, *Magnesium Technology*, eds. R. Beals, A. Luo, N. Neeglameggham, and M. Pekguleryuz (Wiley, 2007), 263–268.

37. A. Akhtar and E. Teghtsoonian, *Acta Metallurgia*, 17 (1969), 1351–1356.

38. L. Chang, Y. Wang, X. Zhao, and M. Qi, *Materials Characterization*, 60 (9) (2009), 991–994.

39. L.-J. Yang, Y.-H. Wei, and L.-F. Hou, *Journal of Materials Science*, 45 (13) (2010), 3626–3634.

40. C. Cáceres and D. M. Rovera, *Journal of Light Metals*, 1 (2001), 151–156.

41. T. B. Abbott, C. Cáceres, and M. A. Easton, *Handbook of Metallurgical Process Design*, eds. G. Totten, K. Funatani, and L. Xie (Marcel Dekkers, New York, USA, 2003), chap. 10, 487–538.

42. J. F. Nie, *Metallurgical and Materials Transactions A*, 43 (11) (2012), 3891–3939.

43. C. R. Hutchinson, J. F. Nie, and S. Gorsse, *Metallurgical and Materials Transactions A*, 36 (8) (2005), 2093–2105.

44. W. Kim, S. I. Hong, and Y. H. Kim, *Scripta Materialia*, 67 (7-8) (2012), 689–692.

45. Y. Hong, H. Xiaowu, N. Qiao, and C. Lei, *China Foundry*, 8 (3) (2011), 269–273.

46. C. Cáceres, W. Poole, A. Bowles, and C. Davidson, *Materials Science and Engineering: A*, 402 (1-2) (2005), 269–277.

47. S. Celotto, *Science*, 48 (2000), 1775–1787.

48. S. Celotto, T. Bastow, P. Humble, and C. Bettles, *Proceedings of the Third International Magnesium Conference*, ed. G. W. Lorimer (Institute of Materials, London, 1997), 391–402.

49. A. Nayeb-Hashemi, *Phase Diagrams of Binary Magnesium Alloys* (ASM International, Metals Park, Ohio, 1988).

50. J. del Valle, F. Carreño, and O. Ruano, *Acta Materialia*, 54 (16) (2006), 4247–4259.

51. W. Morrison, *ASM Transactions Quarterly*, 59 (4) (1966), 824–846.

52. *ASM Handbook: Volume 14 (Forming and Forging)* (ASM, 1990).

53. S. Gall, R. Coelho, S. Müller, and W. Reimers, *Materials Science and Engineering: A*, 579 (2013), 180–187.

54. H. Zhang, G. Huang, D. Kong, G. Sang, and B. Song, *Journal of Materials Processing Technology*, 211 (10) (2011), 1575–1580.

55. T. Wu, L. Jin, W. Wu, L. Gao, J. Wang, Z. Zhang, and J. Dong, *Materials Science and Engineering: A*, 584 (2013), 97–102.

56. W. F. Hosford, *Materials Science and Engineering: A*, 257 (1998), 1–8.

57. Y. Liu and X. Wu, *Metallurgical and Materials Transactions A*, 37 (January) (2006), 7–17.

58. T. Ebeling, C. Hartig, and R. Bormann, *Magnesium Technology*, eds. S. Agnew, N. Neeglameggham, E. Nyberg, and W. Sillekens (Hoboken, New Jersey, 2010), 521–525.

59. J. Koike, Y. Sato, and D. Ando, *Materials Transactions*, 49 (12) (2008), 2792–2800.

60. M. Barnett, *Materials Science and Engineering: A*, 464 (1-2) (2007), 1–7.

61. E. Ball and P. Prangnell, *Scripta Metallurgica et Materialia*, 31 (2) (1994), 111–116.

62. I. Beyerlein, L. Capolungo, P. Marshall, R. McCabe, and C. Tomé, *Philosophical Magazine*, 90 (2010), 2161–2190.

63. V. Meyers, M.A., Vohringer, O., Lubarda, *Acta Materialia*, 49 (19) (2001), 4025–4039.

64. Y. Chino, K. Kimura, and M. Mabuchi, *Materials Science and Engineering: A*, 486 (1-2) (2008), 481–488.

65. S. Kleiner and P. Uggowitzer, *Materials Science and Engineering: A*, 379 (1-2) (2004), 258–263.

66. S. Agnew, J. Horton, T. Lillo, and D. Brown, *Scripta Materialia*, 50 (3) (2004), 377–381.

67. M. Barnett, N. Stanford, P. Cizek, C. Bettles, Z. Xuebin, and Z. Keshavarz, *JOM*, 61 (8) (2009), 19–24.

68. M. Barnett, *Materials Science and Engineering: A*, 464 (1-2) (2007), 8–16.

69. A. Sadeghi, S. Shook, and M. Pekguleryuz, *Materials Science and Engineering: A*, 528 (25-26) (2011), 7529–7536.

70. A. Luo, *Metallurgical and Materials Transactions A*, 26 (September) (1995), 2445–2455.

71. M. Marya, L. G. Hector, R. Verma, and W. Tong, *Materials Science and Engineering: A*, 418 (1-2) (2006), 341–356.

72. Z. Chen, J. Huang, R. F. Decker, S. E. Lebeau, L. R. Walker, O. B. Cavin, T. R. Watkins, and C. J. Boehlert, *Metallurgical and Materials Transactions A*, 42 (5) (2010), 1386–1399.

73. Z. Li, J. Dong, X. Q. Zeng, C. Lu, and W. J. Ding, *Materials Science and Engineering: A*, 466 (1-2) (2007), 134–139.

74. T. Mukai, T. Mohri, M. Mabuchi, M. Nakamura, K. Ishikawa, and K. Higashi, *Scripta Materialia*, 39 (9) (1998), 1249–1253.

75. C. W. Chung, R. G. Ding, Y. Chino, M. A. Hodgson, and W. Gao, *IOP Conference Series: Materials Science and Engineering*, 4 (2009), 012012.

76. Y. Lu, Q. D. Wang, W. J. Ding, X. Q. Zeng, and Y. P. Zhu, *Material Letters*, 44 (July) (2000), 265–268.

CHAPTER V

Conclusions and Recommendations

5.1 Conclusions

Increased use of Mg sheet in automotive applications would result in substantial mass-reductions. Currently less than 1% of the weight of modern North American automobiles are comprised of Mg components [1]. One of the barriers preventing increased employment of Mg sheet has been limited formability. Due to its hcp crystal structure, the production of Mg sheet results in a strong basal texture that generally persists through further processing. This texture results in strong tensile-compressive asymmetry, a resistance to sheet thinning, and generally poor formability. Some of the limitations the basal texture can be overcome by utilizing warm forming, which allows for the activation of $\langle \mathbf{c}+\mathbf{a} \rangle$ pyramidal slip, therefore providing for extension along the c-axis. Yet, this increased manufacturing cost, has deterred increased usage of Mg sheets.

It has been established that a reduction in the basal texture can dramatically improve formability. One of the most successful approaches has been alloying with RE elements [2]. For reasons not yet understood, RE alloys have weaker deformation textures, which can be altered by post-deformation annealing. However, RE elements are advantageous additions in other applications as well, such as magnets

and phosphors for lighting, and are in high demand for clean energy applications. RE elements are expensive, and several of the most common RE additions to Mg alloys (yttrium, neodymium, cerium, and lanthanum) are at critical or near-critical supply risk [3]. Thus a need arises to achieve weaker textures by focusing on the processing route and the addition of secondary-phase particles in conventional alloys.

The objective of this research was to understand the mechanisms behind the favorable mechanical properties observed in TTMP sheet. TTMP was developed by Decker and co-workers to address the need for improved formability in Mg sheet while maintaining strength [4, 5]. It was known that the as-molded plates had a fine grain size, low porosity, intermetallics decorating the grain boundaries, and an isotropic texture due to the casting process. The hypothesis was that the severe plastic deformation introduced during rolling would refine the grain size, leading to improvements in both strength and ductility [6]. It was also believed that rolling would act to fracture the secondary phases, and thus improve formability as cracking in the brittle intermetallics has been associated with a decrease in ductility [7, 8]. The microstructure evolution during TTMP and the effect of this evolution on the tensile deformation behavior had not been throughly investigated. Of particular importance, due to its significant influence on formability, was to understand the texture evolution through TTMP.

We have demonstrated that Thixomolding followed by subsequent thermomechanical processing of AZ61 results in sheet with an good balance of strength and ductility. This success is a result of achieving sheets with a weak basal texture and a fine grain size, which is stabilized by β-$Mg_{17}Al_{12}$ particles. The deformation texture has a maximum texture intensity of less than 5 MRD, while the maximum intensity in conventional AZ31 sheet is typically around 10 MRD [9]. This texture is reduced to

less than 3 MRD during static recrystallization, leading to an increase in elongation to failure and decreased planar anisotropy. Indicators of formability determined from tensile deformation, such as the elongation to failure, work hardening coefficient, and r-value, indicate that TTMP AZ61 will have excellent room temperature formability for Mg sheet. The strength of the sheets varies according to the Hall-Petch relationship, however the texture must also be taken into account. The yield strength and work hardening coefficient are directly related to the number of grains oriented favorably for basal slip in the loading direction.

Based on this investigation, we cannot conclude which mechanisms are responsible for the weak deformation texture in TTMP AZ61, however it appears that the β-$Mg_{17}Al_{12}$ particles play an important role. It was observed that the as-rolled sheet exhibited a limited amount of dynamic recrystallization, and that the dynamically recrystallized grains were associated with regions of a high density of β-particles. The relative reduction of texture following annealing is consistent with that caused by PSN [10]. Although PSN is usually associated with particles larger than 1 μm, which is satisfied by only a small fraction of the β-particles observed in the TTMP sheet, the critical size for PSN decreases with increasing strain. A 50% reduction of thickness in a single pass, may have provided sufficient dislocation gradients to allow smaller particles to serve as nucleation sites as well [11]. Furthermore, small, closely spaced precipitates have been observed to alter the recrystallization kinetics by pinning high angle grain boundaries, perhaps leading to an extended recovery period [11]. Discontinuous static recrystallization, which is more likely to result in texture reduction during annealing than continuous recrystallization, tends to be reported more often in Mg alloy sheets that have undergone less dynamic recrystallization. It is a reasonable assumption that the weaker deformation texture, and the reduction

of texture during annealing, results from increased discontinuous static recrystallization as β-particles hindered dynamic recrystallization. A similar mechanism has been suggested for the formation of the RE-textures [12, 13].

The preheat, rolling, and annealing stages had only a moderate influence on the β-particles. The amount of finer-precipitates fluctuated as thermal exposures resulted in precipitation or dissolution, but the number of particles > 0.5 μm remained quite stable. The large particles are not fractured during the rolling process, rather they deform, becoming elongated parallel to the rolling direction. Aside from a moderate elongation of the network of β-particles and deformation of the larger β-particles, the distribution of the β-phase is largely pre-determined by the as-molded microstructure. In the as-molded plate, β-particles decorated the α-Mg grain boundaries. As the β-particles stabilize the recrystallized grain size, it is not a coincidence that the grain size in annealed sheets is so similar to that of the plates.

Though β-particles promote a stable, refined grain size and likely weaken the basal texture of the sheet, they also initiate damage during deformation. Particles began to fragment as early as 4% strain. Damage accumulation in the β-phase has been associated with decreased ductility. However, for the β-particle sizes and distributions in the as-molded, as-rolled, and annealed TTMP sheets, failure was not attributed to the damage in the secondary particles. The elongation to failure was insensitive to the variation of the β-phase volume fraction achieved by annealing treatments. Furthermore, analysis of the damage showed no evidence of cracks propagating from the particles into the matrix. Fractography reveals that failure results from microvoid coalescence in the matrix following the development of shear instability.

This work highlights the importance of considering the addition of an increased amount of secondary phase particles to alloys subjected to rolling. In order to pro-

duce weakly-textured and fine-grained Mg alloy sheet, it is logical to start with a weakly-textured and fine-grained precursor, such as Thixomolded plate. Microstructure control can by obtained by the addition of secondary phase particles which can act to stabilize the grain size and promote a weaker deformation texture. As the arrangement and distribution of particles evolves little during TTMP, the largest amount of control in the secondary phases will likely be attained in the molding phase of TTMP. If kept sufficiently small, these particles will not limit ductility. However, adaption of these materials to commercial applications requires consideration of the consequence of β-particle fragmentation on fatigue and corrosion.

5.2 Recommendations for Future Research

The success of TTMP has been demonstrated, and many of the mechanisms responsible have been determined, but research on this production method and recrystallization in Mg sheets is far from exhausted. Based on this investigation, the following future work is recommended.

1. A detailed study of the relationship between the β-particles and the weak deformation texture. Having only one condition of Thixomolded plate limited our ability to evaluate the effect of β-phase particles on the dynamic recrystallization mechanisms and kinetics. In order to understand the mechanisms resulting in the significant difference between the deformation texture of commercial AZ31 and TTMP AZ61, it is important to isolate the effect of the rolling schedule used in TTMP from the results of selecting an alloy with a higher quantity of β-particles. Annealing of the Thixomolded AZ61 to reduce the fraction of intermetallic particles will result in an increase in grain size. The relative ac-

tivity of slips systems can depend on grain size, therefore, ideally the quantity of secondarily phases should be varied independent of grain size. This could be achieved by comparing different alloys. AZ31 does not Thixomold well, and it may not be possible to find another production method for un-textured AZ31 with a grain size less than 5 μm for comparison to the Thixomolded AZ61. Use of larger-grained, direct chill (DC) cast AZ31, AZ61, and AZ91, annealed such that all three alloys have the same grain size, seems the best approach for determining the relationship between the quantity of β-particles and deformation texture.

Subjecting 3 mm thick DC cast plates of the three alloys to the same rolling parameters used to produce the TTMP AZ61 in this study would also allow for comparison between the deformation texture resulting from use of the fine-grained Thixomolded AZ61 to that from the DC cast plates. Cooling rates in DC casting are slower than that in Thixomolding, so the β-volume fraction will be higher as well, though that could be modified by annealing. The slower cooling rate will also result in a coarser β-particles and eutectics. The size and spacing of the β-particles will determine their effect on dynamic recrystallization. It may be that in DC cast alloys, PSN is most significant, whereas retardation of the recrystallization kinetics by Zener drag is dominant when starting with Thixomolded plate. Differences between the TD spread in materials with different sized β-particles could help elucidate the formation of the so-called RE texture.

The rolling schedule used in the production of TTMP AZ61 may not be suitable for the rolling of DC cast AZ31, AZ61, and AZ91. However, as the goal of this study would be to understand the deformation texture; in this situation, edge

cracking and poor surface quality are tolerable. Similarly, increased porosity in the DC cast alloys is acceptable. As a final note, AZ71, AZ81, and AZ91 can be successfully Thixomolded [14, 15], so there is an option to study TTMP in alloys with increasing Al content.

2. Investigation of TTMP on more complicated alloy systems. Within the two-phase system provided by AZ61, microstructure control is limited. It seems feasible to design an alloy such that one phase serves to promote a weak recrystallization texture while a second, thermally stable phase, acts to stabilize the grain size. Selecting the first phase to have a low dissolution temperature, allows these particles to be removed by annealing, decreasing the potential volume of cracked particles during deformation. If processing could achieve a homogenous distribution of the thermally stable particles, finer recrystallized grain sizes could be attained. In addition to increasing strength via the Hall-Petch relationship, it would also be useful to produce TTMP sheets from age-hardenable alloys.

3. Room temperature formability studies. Comparison of the tensile deformation behavior, specifically the r-values, in TTMP AZ61 to other Mg alloy sheets indicates that TTMP AZ61 may have excellent room temperature formability, but this has yet to be established. Erichsen tests should be conducted on, at minimum, sheet annealed for 285°C/10 min. Evaluating sheet annealed for 420°C/28 h would provide for a comparison with a larger grained material free of secondary phases.

4. Investigation of the effect of variations in the TTMP rolling schedule on microstructure and texture evolution. As discussed in Chapter I, asymmetric

rolling can produce more weakly textured material than symmetric rolling. Comparing the deformation texture as a function of the ratio of speed between the top and bottom rolls in TTMP sheet could provide more insights into the mechanisms responsible and potentially lead to further advancement of TTMP. Maintaining the same pre-heat and rolling temperatures, as well as thickness reduction will allow for comparison to the work in this dissertation. It should be noted, that we have done some preliminary studies on the texture in TTMP AM60 produced by multiple-pass cross rolling, a technique that has also been demonstrated to reduce texture intensity. However, multiple variables were changed in the production process, including the alloy, so the effect of the cross rolling itself can not be isolated.

5. EBSD studies to explore the relationship between GOS and grain orientation in deformed material. For this dissertation, EBSD was successfully conducted on samples loaded to ϵ=10%. Partitioning the texture of large (> 1000 grain) EBSD maps from deformed material based the internal misorientation (GOS) would provide knowledge of which grain orientations are accommodating more of the deformation. Performing this analysis on textured samples loaded along different directions could provide further insights into how texture influences deformation behavior.

6. Plasticity modeling. Use of a self-consistent polycrystal plasticity model would allow for a more sophisticated theoretical description of the orientation dependence of yield strength and work hardening based on texture than presented in this investigation. This could be used to confirm, for instance, that the difference in strength between the as-molded and annealed sheets (not associated

with Hall-Petch) is due to increased "soft" basal slip activity in the un-textured as-molded material. Having an experimentally calibrated model for plasticity in TTMP AZ61 would also increase the efficiency of further studies. For instance, the proposed study on the effect of β-particles on the deformation texture will yield crystallographic information that can be fed into the plasticity model. Stress-strain curves can be predicted for each deformation texture. Based on the results of the modeling, the conditions most constructive for further work can be selected, reducing the time and cost needed to machine and test tensile specimen.

7. Detailed TEM analysis of the dislocations following deformation of annealed sheets. Information of the relative activity of the different slip systems in deformed sheet would complement, or suggest changes to, the slip-system dependent hardening parameters used to calibrate the plasticity model. Dislocation analysis can provide more information as to the activity of non-basal slip as the loading direction is varied. Foils for TEM would need to be removed from samples with only 1 to 2% plastic deformation. Foils removed such that the foil normal is parallel to loading direction will allow for easy comparison of slip and loading directions. As many of the grains are oriented such that their c-axis is perpendicular to the loading direction, this foil orientation provides for viewing the basal plane "edge-on" such that basal dislocations appear straight [9]. It is also recommended to prepare foils with a normal parallel to that of the sheets to examine prismatic slip, though care will have to be taken to track the loading direction.

8. Detailed TEM analysis of fine β-precipitates through TTMP. Only limited TEM

observations were conducted on the as-molded plate, as-rolled sheet, and sheet annealed at 285°C for 10 minutes. It is unknown how the density and distribution of β-particles smaller than 200 nm evolve during processing. In addition, while study of the as-rolled sheet is difficult due to the high dislocation density, analysis of rolled sheet following an annealing treatment selected to promote recovery, could provide insights into the activity of PSN and the interaction between high angle grain boundaries and fine β-particles. Based on the work demonstrated in Figure 3.16, 130°C for 100 minutes promotes recovery, but not static recrystallization, such that the dynamic recrystallization mechanisms active during TTMP could be studied.

9. Fatigue studies should be conducted in pre-strained TTMP AZ61. Though it was demonstrated that damage accumulation in the β-phase during tensile loading does not cause failure, the effect of this damage on fatigue has yet to be investigated. Components formed from TTMP AZ61 sheets will contain voids from the β-particle cracking, with the void density varying with the strain distribution. It is unclear how these voids will behave during service. If the presence of these cracks rapidly degrades the fatigue lifetime of the Mg alloy sheet components, a recommendation to increase the fraction of secondary particles would be unwise. Small fatigue crack growth studies should be conducted on TTMP AZ61 that has been pre-strained to simulate forming. Focus should be made on the relationship of the fatigue cracks and the β-particles and the preexisting damage in the the particles. In addition, a comparison of fatigue lifetime to pre-strained commercial AZ31 should be made. It should be noted that Chen and co-workers have studied fatigue and small crack growth in Thixomolded and TTMP AM60 [16, 17], though an emphasis was not made on the β-particles.

Also, that batch of materials contains a higher porosity and much higher fraction of externally solidified grains than the AZ61 materials used in this study, since then the Thixomolding parameters have been adjusted; current batches of TTMP AZ61 likely have a longer fatigue life.

10. Corrosion studies. Cracking in the β-particles during deformation will create effective porosity in formed components. In addition, the effect of the β-phase on corrosion is dependent on the particle size and volume fraction [18, 19]. The corrosion rate resulting from (1) the size and distribution of β-particles resulting from TTMP and (2) cracking of the β-particles during deformation will allow for a more informed decision as to the appropriate amount of β-particles to incorporate into TTMP and other Mg sheet production methods.

Bibliography

1. M. Luo, M. Dunand, and D. Mohr, *International Journal of Plasticity*, 32-33 (2012), 36–58.
2. N. Stanford, D. Atwell, and M. Barnett, *Acta Materialia*, 58 (20) (2010), 6773–6783.
3. "Critical Materials Strategy," Tech. rep., U.S. Department of Energy (2011).
4. R. F. Decker, S. Kulkarni, J. Huang, and S. LeBeau, *Magnesium Technology*, eds. E. Nyberg, S. Agnew, N. Neeglameggham, and M. Pekguleryuz (Wiley, 2009), 357–361.
5. G.-S. Huang, H.-C. Li, B. Song, and L. Zhang, *Transactions of Nonferrous Metals Society of China*, 20 (1) (2010), 28–33.
6. J. Chapman and D. Wilson, *Journal of the Institute of Metals*, 91 (1962), 39–40.
7. *ASM Handbook: Volume 2 (Properties and Selection : Nonferrous Alloys and Special-Purpose Materials)* (ASM, 1990).
8. I. Polmear, *Light Alloys: From Traditional Alloys to Nanocrystals* (Elselvier, Oxford, 2006), 4 ed.
9. S. Agnew and O. Duygulu, *International Journal of Plasticity*, 21 (6) (2005), 1161–1193.
10. F. Habiby and F. Humphreys, *Textures and Microstructures*, 20 (1977) (1993), 125–140.
11. F. Humphreys and M. Hatherly, *Recrystallization and Related Annealing Phenomena* (Elsevier, Netherlands, 2004), 2 ed.
12. J. P. Hadorn, K. Hantzsche, S. Yi, J. Bohlen, D. Letzig, J. A. Wollmershauser, and S. Agnew, *Metallurgical and Materials Transactions A*, 43 (April) (2012), 1347–1362.
13. K. Hantzsche, J. Bohlen, J. Wendt, K. Kainer, S. Yi, and D. Letzig, *Scripta Materialia*, 63 (7) (2010), 725–730.
14. R. F. Decker and S. E. Lebeau, *Advanced Materials and Processes*, (April) (2008), 28–30.
15. R. F. Decker, *Solid State Phenomena*, 192-193 (2012), 47–57.
16. Z. Chen, J. Huang, R. F. Decker, S. E. Lebeau, L. R. Walker, O. B. Cavin, T. R. Watkins, and C. J. Boehlert, *Metallurgical and Materials Transactions A*, 42 (5) (2010), 1386–1399.
17. Z. Chen, A. Shyam, J. Huang, R. Decker, S. E. Lebeau, and C. J. Boehlert, *Metallurgical and Materials Transactions A*, 44 (February) (2013), 1045–1058.
18. G. Song, A. Atrens, and X. Wu, *Corrosion Science*, 40 (10) (1998), 1769–1791.
19. G. Song, A. Atrens, and M. Dargusch, *Corrosion Science*, 41 (1999), 249–273.

APPENDIX

APPENDIX

X-Ray Diffraction Texture Measurements and Comparison to Texture via EBSD

Crystallographic texture has been conventionally measured by X-ray diffraction (XRD), however analysis via electron backscatter diffraction (EBSD) is becoming more prevalent as the speed of EBSD systems increases [1, 2]. Both techniques were used to characterize texture in the AZ61 materials in this research, but for consistency, the texture evolution detailed in Chapters 3 and 4 was illustrated using only EBSD pole figures. This appendix provides the experimental procedure used to generate XRD pole figures, describes the differences between both techniques, and justifies the validity of the EBSD pole figures used in this dissertation.

A.1 Experimental Procedure for Generation of XRD Pole Figures

A Rigaku rotating anode X-Ray diffractometer with a computer automated pole figure attachment was used to measure XRD intensity. Coupons of material of at least 6.35 mm x 6.35 mm x 1 mm thick (the maximum sample size the pole figure attachment can accept is 31.8 mm in diameter and 3 mm thick) were prepared by grinding to 1200 grit SiC paper with water. Bragg peaks were determined by a $\Theta/2\Theta$ scan with a resolution of 0.01° and a scan rate of 4 points per second between 30° and

65°. Incomplete pole figures of the $\{0002\}$, $\{10\bar{1}0\}$, $\{10\bar{1}1\}$, and $\{10\bar{1}2\}$ were collected by recording the intensity in increments of 3° out to 75° in the radial direction and in 5° steps in the azimuthal direction. The azimuthal rotation speed was 180° per minute. Oscillation of the sample under the beam maximized the number of grains included in the measurement.

Multiple pole figures are required in order to uniquely determine texture; at minimum the three pole figures with the smallest Bragg peaks should be used [3]. Due to geometric constraints of XRD systems, Bragg peaks above 60° are not used. As the specimen is tilted about the $\Theta/2\Theta$ axes and radial axis the beam becomes spread out on the specimen surface (Figure A.1), correspondingly the diffracted beam spreads out as well [3]. Above a certain spread, not all of the beam enters the detector. As a consequence, intensity will decrease towards the edges of a pole figure, even in a randomly oriented sample, for purely geometric reasons. Thus, raw pole figures are incomplete, only going to a radial tilt of 75° or 80°, and a defocusing correction is required to increase the intensity near the edge of measured pole figures [3]. Figure A.2 provides an example of a defocusing correction.

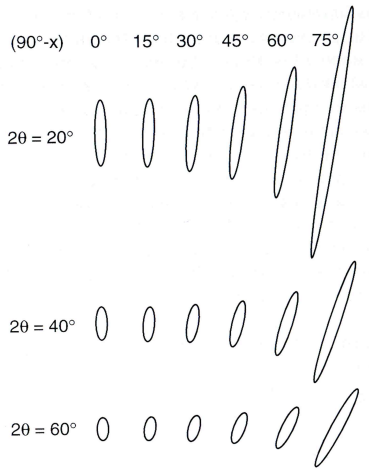

Figure A.1: Change in shape and orientation of x-ray stop size as a function of radial tilt and Bragg angle. Figure from [3].

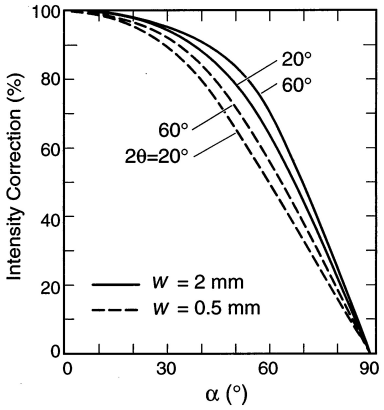

Figure A.2: Theoretical intensity correction curves for two different values of 2Θ and receiving slit widths. Figure from [3].

The best procedure for determining the defocusing correction is to measure the intensity from a reference sample with a random texture. Random texture can be verified by either examination of the pole figures or a $\Theta/2\Theta$ scan, though the pole figure method is preferred [4]. If using a $\Theta/2\Theta$ scan to ascertain randomness, the intensity ratios of the major peaks should be compared to the intensity ratios found

in the Joint Committee on Powder Diffraction Standards (JCPDS) files. Preferred orientation, p_{hkil}, can be quantified using the method of Harris:

$$p_{hkil} = N\left(\frac{I_{hkil}}{I^o_{hkil}}\right)\left(\sum_{hkil=1}^{N}\frac{I_{hkil}}{I^o_{hkil}}\right)^{-1} \tag{A.1}$$

where N in the number of peaks within the region of interest, I_{hkil} is the measured peak intensity, and I^o_{hkil} is the intensity from the JCPDS file [5]. If $p_{hkil} < 1$, the preferred orientation is along an axis other than $\langle hkil \rangle$. A value of $p_{hkil} > 1$ indicates a texture in the $\langle hkil \rangle$ axis. The maximum texture strength possible is N. A value of $p_{hkil} = 1$ for all sets of hkil indicates a randomly oriented sample.

In this case, the as-Thixomolded plate was chosen as the reference sample; this is a reasonable assumption as p_{0002} is 1.28 in this material as calculated from the data given in Table A.1. $\Theta/2\Theta$ measurements of the as-Thixomolded material shown in Figure A.3 demonstrate the similarity of peak intensities to a random sample.

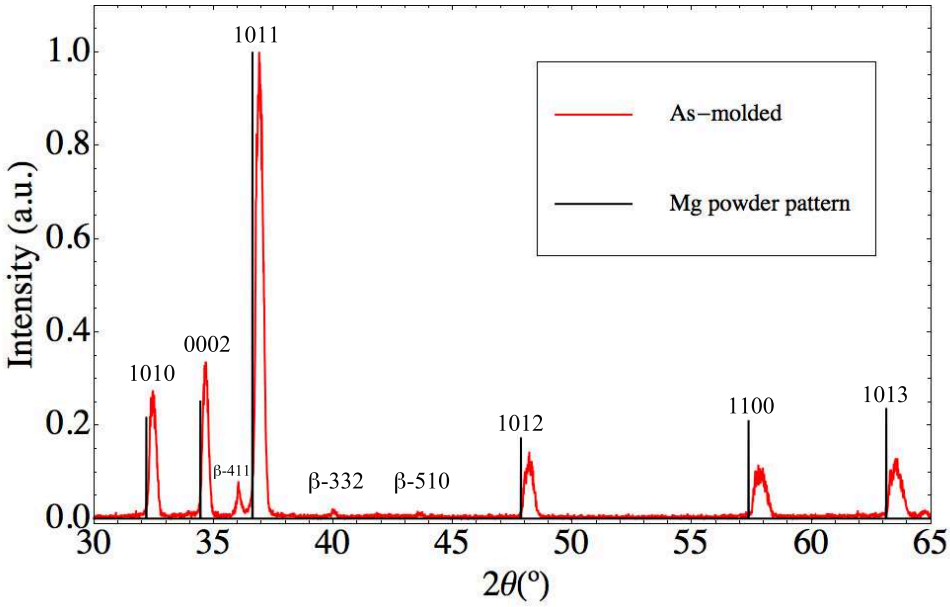

Figure A.3: Diffracted intensity from $\Theta/2\Theta$ scan of as-molded AZ61 aside peaks from the JCPDS file 04-003-2526 for Mg powder.

Table A.1: Data used for calculation of preferred orientation. $2\Theta^o$ and I^o_{hkil} values from JCPDS file # 04-003-2526.

hkil	$\mathbf{2\Theta^o(^\circ)}$	$\boldsymbol{I^o_{hkil}}$	$\mathbf{2\Theta(^\circ)}$	$\boldsymbol{I_{hkil}}$
$10\bar{1}0$	32.183	0.218	32.47	0.26
0002	34.447	0.253	34.67	0.33
$10\bar{1}1$	36.630	1.000	36.93	1.00
$10\bar{1}2$	47.856	0.174	48.20	0.12
$11\bar{2}0$	57.382	0.211	57.88	0.10
$10\bar{1}3$	63.140	0.237	63.55	0.11

It should be noted that the difference between the reference and measured peak locations is due to the alteration of the lattice constant by the addition of Al. The lattice parameters in pure Mg are a = 0.32092 nm and c = 0.52105 nm and the lattice parameters in AZ61 are a = 0.319 nm and c = 0.518 nm [6].

The planar spacings, d_{hkl}, in hexagonal crystals can be calculated by:

$$d_{hkl} = \left[\frac{4}{3a^2}\left(h^2 + hk + k^2\right) + \frac{l^2}{c^2}\right]^{-\frac{1}{2}} \tag{A.2}$$

The distance between lattice planes can be experimentally determined from XRD using Bragg's Law:

$$n\lambda = 2d\sin\Theta \tag{A.3}$$

where λ is the wavelength of the X-Ray radiation, 0.1541 nm, n is an integer, and Θ is the experimentally determined Bragg angle. By setting d_{hkl} in Equation A.2 to d in Equation A.3 the lattice constants for any particular plane {hkl} can be determined. Using the Bragg angles measured in the as-molded material (listed in Table A.1) for $\{10\bar{1}0\}$ and {0002} we find that a = 0.318 nm and c = 0.517 which are in good agreement with [6], confirming that the shift in peak locations is due to that alloying addition of Al.

Pole figures for a random sample should not have any peaks and the intensity within each radial ring should be constant [4]. The intensity within 45° should show

little variation, and should smoothly decrease as the radial angle increases outside this bound. The raw 0002 pole for the Thixomolded plate in Figure A.4 meets this conditions.

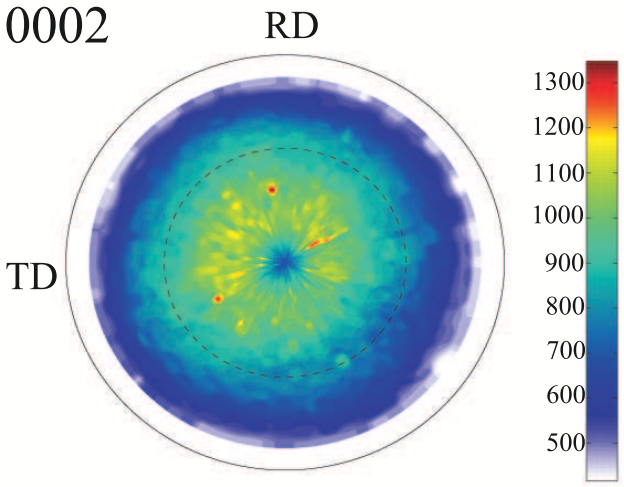

Figure A.4: Raw 0002 pole figure for the Thixomolded plate. The dashed circle is drawn at $\alpha = 45°$.

Complete pole figures were calculated using MTEX, a MATLAB® toolbox created for texture analysis [7]. Eight data files were imported in order to generate the a full description of the texture of each material, the raw $\{0002\}$, $\{10\bar{1}0\}$, $\{10\bar{1}1\}$, and $\{10\bar{1}2\}$ pole figures as well as their defocusing correction (here the as-molded pole figures). The software requires knowledge of the sample symmetry (triclinic) and crystal symmetry (point group is 6/mmm with a = 3.19 $\mathring{A}$ and c = 5.18 $\mathring{A}$). After the defocusing correction is applied to each pole figure, all four incomplete pole figures are used in order to generate a orientation density function (ODF) for the material.

The ODF is a tool for describing the normalized probability density of each texture component, which can be described by three Euler angles. MTEX calculates the ODF by using a series expansion method for fitting the coefficients of harmonic functions

[7]. The ODF unites all of the incomplete pole figures into a complete representation of all of the crystal orientations within the specimen volume. Once the ODF has been constructed it can be used to calculate any pole figure for the material. Thus, we can extract a complete {0002} pole figure. In addition, the generated pole figures can be rotated to the sample orientation of choice. Figure A.5 shows raw, defocusing corrected, and recalculated pole figures for the basal and prismatic pole figures for the as-rolled sheet.

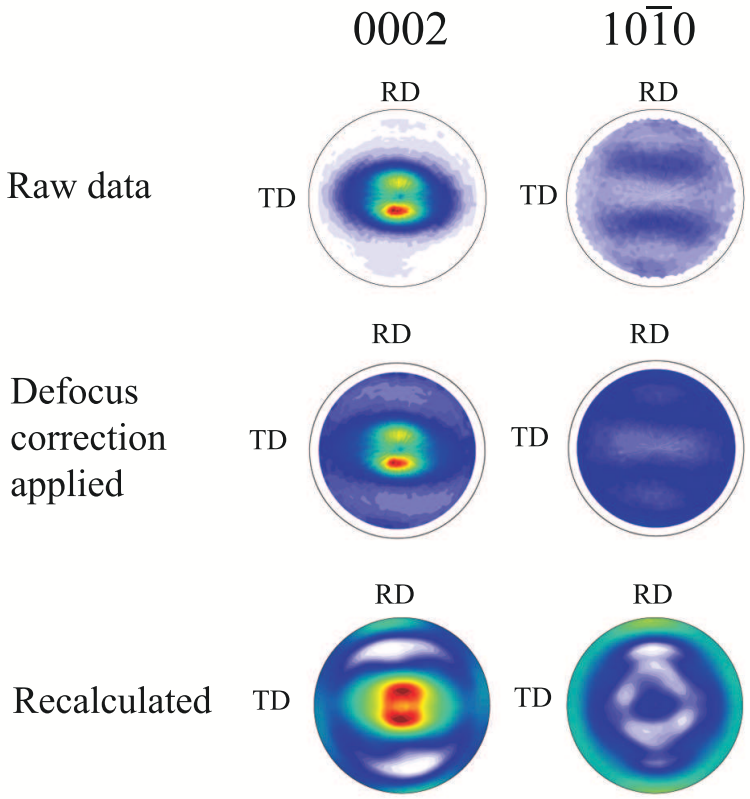

Figure A.5: XRD pole figures of the as-rolled sheet at different stages in the recalculation process.

A.2 XRD vs EBSD

Provided a sufficient number of grains are measured, the most accurate measurement of the true texture is EBSD as it has better accuracy (orientations accurate

to within 2°), there is no defocusing correction needed, and the inherent inaccuracies when recalculating the ODF by deconvolving the XRD pole figures are avoided [8, 9]. XRD provides the most statistical representation of texture. Assuming a beam diameter of 10 mm and a penetration depth of 0.05 mm, XRD samples about 40 million 5 μm diameter grains, far more than can be measured with EBSD [1]. Several researchers have studied the number of grains needed to accurately represent texture, and 1000 grains has emerged as a rule of thumb [1, 8, 10]. Wright et al. [2], however conducted a comparison of texture by EBSD and XRD in low carbon steel and suggested that 10,000 grains be the benchmark for a good statistical representation of texture. Furthermore, they caution that no value is added by taking multiple measurements per grain; scanning duration can be minimized by setting up scanning parameters to sample grains only once or twice each. Figure A.6, from Wright and co-workers demonstrates how pole figures for varying number of grains via EBSD compares to the XRD pole figure. The EBSD scanning parameters in Chap II are based on this work.

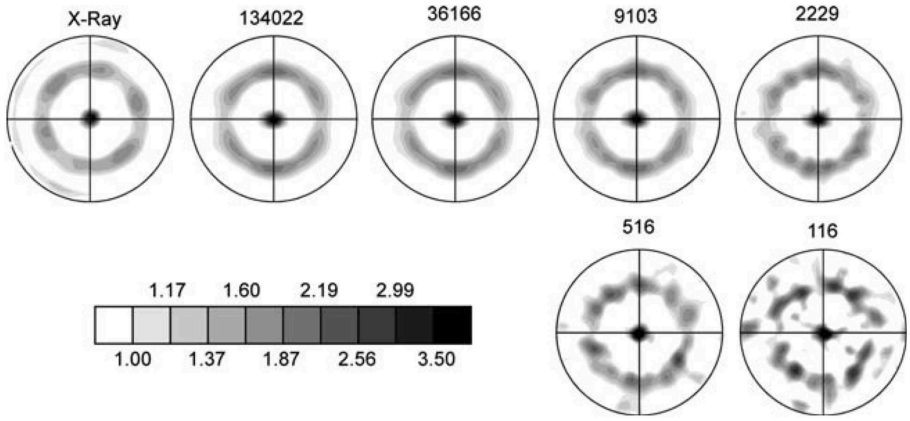

Figure A.6: 110 pole figures for a low carbon steel generated by XRD and by varying numbers of EBSD grain measurements. Figure from [2].

One more important consideration, especially in this work, is the dislocation content of the material. Lattice distortion by deformation produces a distribution of plane spacing and, thus, a distribution of diffraction angles results. In XRD this broadens the diffraction peak, and decreases the maximum raw intensity of each pole figure, but the peak will likely remain far above of background level. As the intensities are normalized in the ODF calculation, the texture intensity of the recalculated pole figures will not be affected as long as each grain orientation contains similar amounts of deformation. In the case of EBSD, this peak broadening manifests as blurring of the Kikuchi bands [11]. As the bands become more diffuse, and the contrast approaches background levels, the likelihood of the software being able to accurately determine the texture is greatly reduced. Mg, already has relatively poor quality images due to its low atomic number (z=12), and thus scatters less electrons than heavier metals such as brass (z=29 and 30 for copper and zinc, respectively). If certain grain orientations or phases preferentially deform, then these grains will be underrepresented in the final EBSD texture. Engler studied EBSD texture in as-deformed and partially recrystallized cold-rolled Al-Mg alloy [1] and concluded that in the partially RX material, since certain orientations recrystallize more rapidly, the non-RX regions were underrepresented in the final texture. In the as-rolled sheet, they observed a decrease in indexing rate but did not see bias towards certain texture components.

With that in mind, we studied how the as-rolled texture generated by EBSD compared to that from XRD for differing number of orientations, as shown in Figure A.7. As the number of orientations increase, the data begins to smooth out and noisy peaks are reduced. The maximum texture intensity by XRD is 4.5 MRD; the maximum intensity via EBSD is too high when less than 6400 orientations are measured,

but converges near the XRD value with the inclusion of $\sim$ 12,000 orientations. This data satisfies one of the measures of statistical significance for texture via EBSD, the jackknife test, in which if you cut the number of grains measured in half, the texture intensity should not increase appreciably [10]. This test was used to determine the number of orientations needed to characterize the texture via EBSD in the as-rolled sheet. For the as-molded plate and recrystallized sheets, a scan area large enough to contain 10,000 grains was used. Figure A.8 summarizes the texture of the primary conditions discussed in this dissertation by both XRD and EBSD. Based on this work, we believe that EBSD characterization of texture in this dissertation is valid.

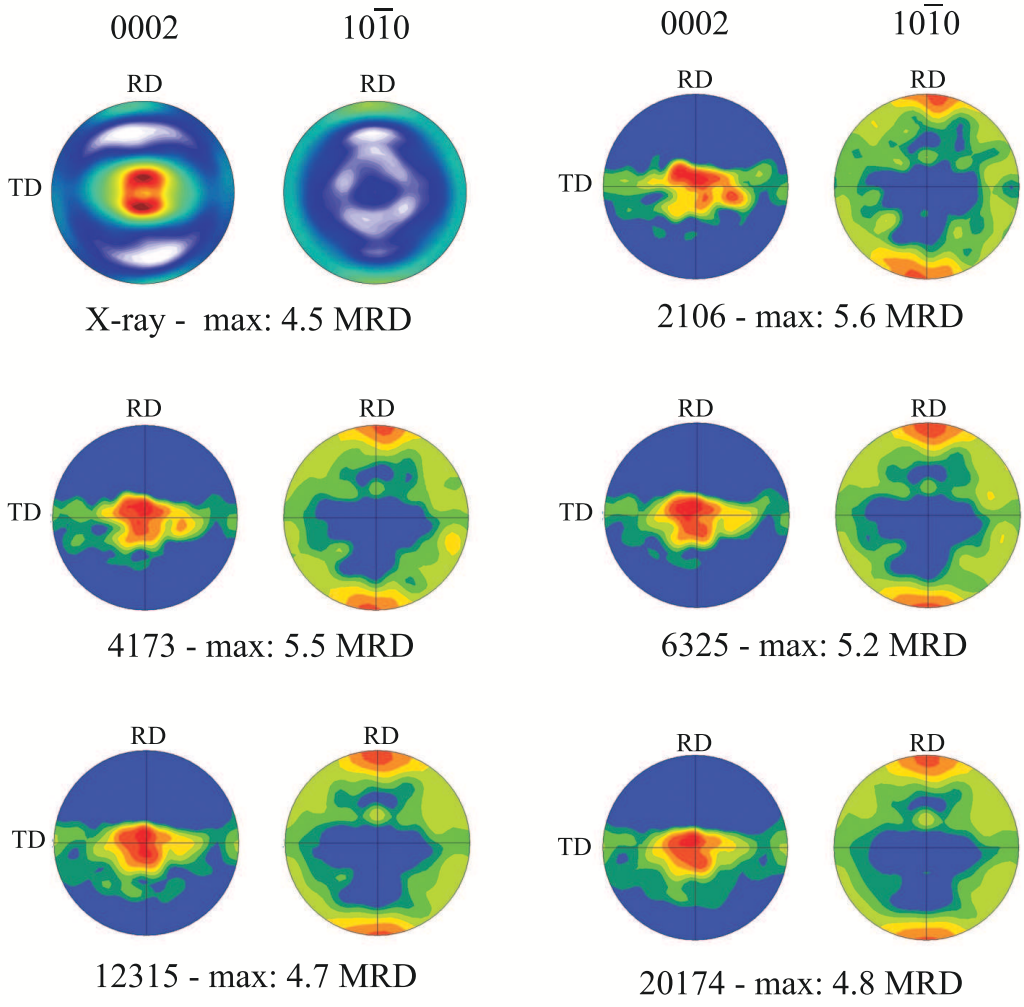

Figure A.7: Basal and prismatic pole figures for as-rolled AZ61 sheet generated by XRD and for an increasing number of EBSD grain orientation measurements. The number of orientations and maximum texture intensity are listed below the pole figures.

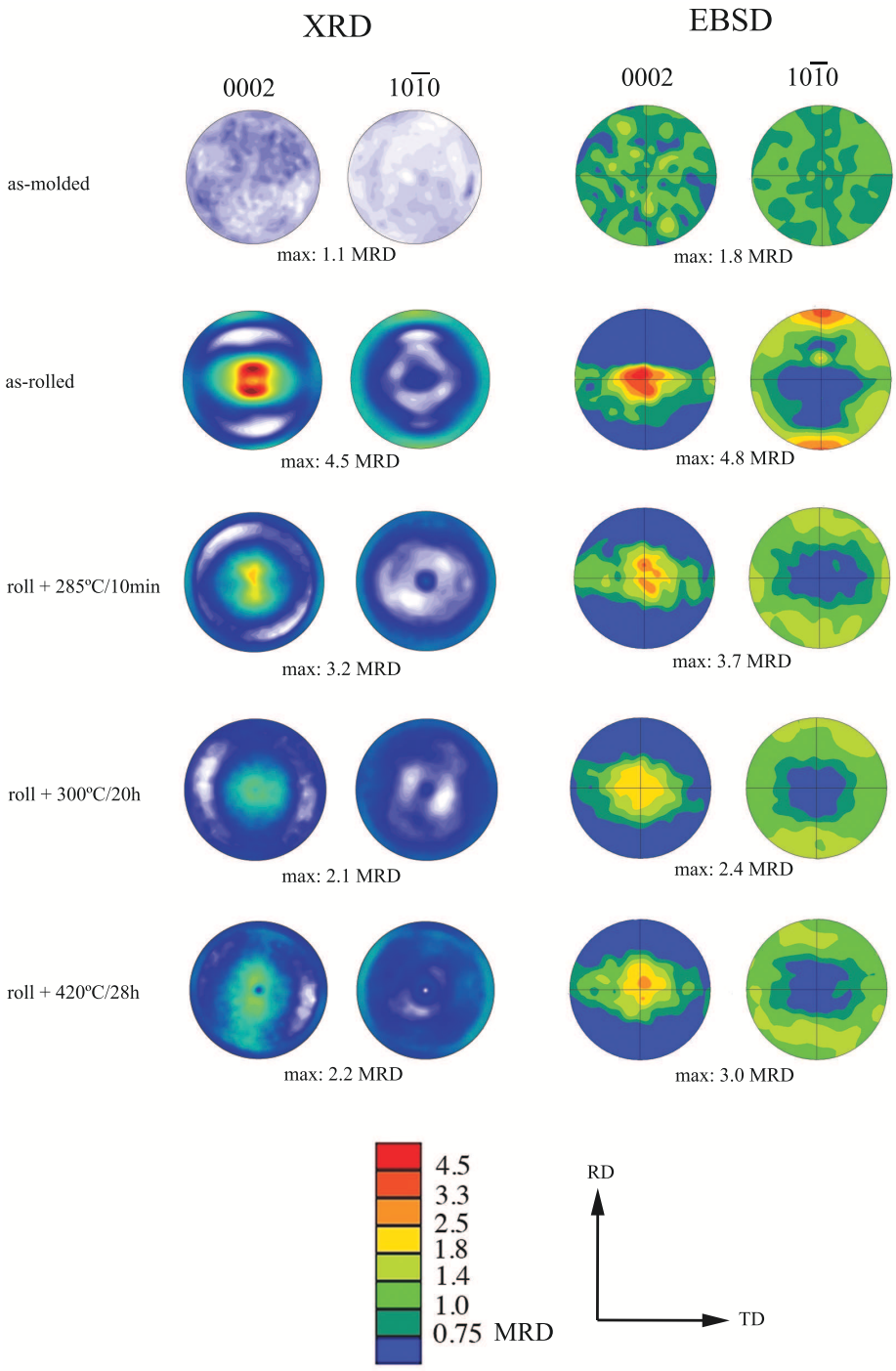

Figure A.8: Basal and prismatic pole figures for by both XRD and EBSD for the primary materials in this dissertation.

Bibliography

1. O. Engler, *Applications of Texture Analysis: Ceramic Transactions* (2009), vol. 201, 125–133.

2. S. I. Wright, M. M. Nowell, and J. F. Bingert, *Metallurgical and Materials Transactions A*, 38 (8) (2007), 1845–1855.

3. U. Kocks, C. Tóme, and H.-R. Wenk, *Texture and Anisotropy: Preferred Orientations in Polycrystals and Their Effect on Materials Properties* (Cambridge University Press, Cambridge, UK, 1998).

4. S. Wright and U. Kocks, "Preferred Orientation Package Los Alamos," (1995).

5. G. Harris, *Philosophical Magazine A*, 43 (336) (1952), 113–123.

6. A. Nayeb-Hashemi, *Phase Diagrams of Binary Magnesium Alloys* (ASM International, Metals Park, Ohio, 1988).

7. F. Bachmann, R. Hielscher, and H. Schaeben, *Solid State Phenomena*, 160 (2010), 63–68.

8. W. B. Hutchinson, *Acta Metallurgica*, 37 (4) (1989), 1047–1056.

9. F. Humphreys, *Journal of Materials Science*, 36 (2001), 3833 – 3854.

10. A. D. Rollett, *ASM Handbook, Volume 22B, Metals Process Simulation*, eds. D. Furrer and S. Semiatin (ASM International, Materials Park, OH, 2010), vol. 22, chap. Input Data, 92–99.

11. A. Wilkinson and D. Dingley, *Acta Metallurgica et Materialia*, 39 (12) (1991), 3047–3055.